Attenuation of Disturbances on an Earth Observing Satellite

by

Pejmun Motaghedi

B.S., Georgia Institute of Technology (1993)

Submitted to the Department of Aeronautics and Astronautics
in partial fulfillment of the requirements
for the degree of

Master of Science in Aeronautics and Astronautics

at the

Massachusetts Institute of Technology

February 1996

Author_____
Department of Aeronautics and Astronautics
November 9, 1995

Certified by_____
Professor Steven R. Hall
Department of Aeronautics and Astronautics
Thesis Supervisor

Accepted by_____
Professor Harold Y. Wachman
Chairman, Departmental Graduate Committee

Attenuation of Disturbances on an Earth Observing Satellite

by

Pejmun Motaghedi

Submitted to the Department of Aeronautics and Astronautics
on November 9, 1995, in partial fulfillment of the
requirements for the degree of
Master of Science in Aeronautics and Astronautics

Abstract

The effects of disturbance sources on the pointing performance of a small spacecraft in NASA's Small Satellite Technology Initiative (SSTI) program were investigated. Two particular disturbances, a stepper motor and thermal snap, have significant impact on the pointing performance. Models of thermal snap and the stepper motor were developed and applied to simulations using a NASTRAN model of the spacecraft. The simulations predicted that most of the performance specifications will be satisfied, with the exception of the pointing stability specification, due to high frequency vibration.

Open- and closed-loop compensation methods were developed to attenuate the disturbance effects and further improve performance. It is shown that the open-loop compensation methods of shaping the input to the stepper motor and feedforward control from the stepper motor to the reaction wheel can successfully attenuate low frequency vibration and improve pointing accuracy. Furthermore, use of rate feedback from a rate gyro to a reaction wheel may be used to improve low frequency vibration, but is not recommended, due to potential instability. Rate feedback from an accelerometer to a piezoceramic actuator can attenuate high frequency vibration, improving the stability performance.

Thesis Supervisor: Steven R. Hall, Sc.D.
Title: Associate Professor of Aeronautics and Astronautics

Acknowledgements

I would like to thank my advisors: Prof. Steven R. Hall for his invaluable guidance and generous commitment of time to his student, and Dr. David W. Miller for his wonderful, practical advice and clear vision of this project. I would also like to thank all my fellow graduate students and friends at SERC for their useful discussions and help which kept my research moving along. I would especially like to thank Carolos Livadas for his personal support and friendship throughout my graduate studies at M.I.T. Finally, I would like to express my heartfelt appreciation and thanks to my family for their unceasing support and love throughout this arduous step in my life.

This research was funded by the Space Engineering Research Center at the Massachusetts Institute of Technology

Contents

List of Figures

List of Tables

Chapter 1

Introduction

1.1 Background

Earth observing satellites make use of sensitive equipment requiring stable spacecraft platforms to fulfill their objectives. The required degree of attitude control and stability of these spacecraft platforms is becoming increasingly stringent due to high performance requirements. The flexible dynamics of spacecraft structures make it even more difficult to achieve good control and stability. Achieving a high level of stability and control comes at great financial cost and requires a long development time, making each spacecraft an enormously expensive and lengthy venture. These two problems, associated with the current practice of custom building most spacecraft, have caused the aerospace industry to begin changing. The industry has recently begun considering increased use of off-the-shelf, commercial components to demonstrate financial savings, maturity of commercial products, and shorter design and manufacturing periods. Although the specifications of individual commercial components are normally well defined, computer simulations and tests must be carried out on the integrated spacecraft to ensure satisfactory overall performance.

For many spacecraft the issue of accurate pointing ability is of great importance. Unfortunately, disturbance sources such as thermal snap and on-board mechanical devices excite the spacecraft's flexible dynamics. This can cause structural vibrations which degrade pointing ability and may require corrective measures. The Clark

spacecraft, an earth observing satellite commissioned by the National Aeronautics and Space Administration (NASA), is one such satellite with a sensitive earth-imaging instrument on board called World View. In order to investigate this potential problem, a performance metric must be clearly defined and disturbance sources which affect it need to be identified and appropriately modeled. Propagation of the disturbance model through a simplified, but accurate, spacecraft model will yield simulated performance that can be compared to performance specifications. A further step can then be taken to determine if performance can be improved in any way, and if so, at what cost. Such simulations often point out potential problems and suggest various solutions which can be very valuable to the designers and manufacturers of the spacecraft prior to launch. Key elements of this process are forming models of the disturbances, developing a simplified but accurate structural model and identifying and implementing control techniques that improve the performance of the particular problem at hand.

1.2 Technical Approach

The phenomenon of thermal snap, a source of vibration in spacecraft solar arrays, is one disturbance source which has begun to attract attention due to increasingly stringent performance requirements. Zimbelman [36, 37] derives an elaborate model of thermal snap using conservation of momentum in which the time rates of change of the thermal gradient are the primary driving variables of the resulting disturbance torque. Poelaert and Burke [26] develop another model of thermal snap specific to the Hubble Space Telescope using a simplified mechanical model of the solar array and Lagrangian analysis. In this thesis a new model of thermal snap is developed where momentum conserving torques are applied to induce the thermally deformed shape of the structure. A key variable in this model, equivalent to specifying the time rates of change of the thermal gradient, is the speed with which the structure is forced from the original to the fully deformed state.

The World View imaging instrument to be used on the Clark satellite is another

of the disturbance sources addressed in this work. At the heart of the disturbance are two stepper motors actuated in microstepping mode which gimbal a two degree of freedom mirror. Microstepping has the advantage of very high resolution, up to 0.0144° [31], but also has the disadvantages of a vibratory step response. Furthermore, microstepping does not ensure good open loop accuracy [1]. However, use of such a high resolution positioning device together with a position sensor in closed loop feedback leads to a highly accurate, discrete positioning system. This thesis attempts to capture the vibratory effects of discrete positioning on the structural model. To do this, the stepper motor is modeled as a displacement actuator rather than a torque actuator.

The structural model used for this work consists of a NASTRAN finite element model obtained from Lockheed-Martin that was initially used for launch load simulations. The final version of this model supplied over 250 degrees of freedom over a bandwidth of 0-100 Hz, requiring model reduction to maintain reasonable computation times. The method of modal cost analysis [28] was chosen over the method of balanced reduction [10] as the model reduction technique for reasons of simplicity and speed. Modifications are made to the model to account for actuators and sensors.

The next step in this problem consists of identifying methods of control to attenuate the effects of these two disturbance sources. Input shaping is one form of open loop control which has been made very robust and practical through work done by Hyde and Seering [12], Singer and Seering [27] and Tuttle and Seering [32]. Application of this method to MIT's Middeck Active Control Experiment by Tuttle and Seering [33] correctly predicted substantial vibration reductions as confirmed by its recent flight on the Space Shuttle Endeavor. This method is applied to the problem at hand to shape the World View instrument's disturbing motor slews to avoid exciting Clark's flexible modes.

Feedforward control is one simple method that can be used to prevent excitation of the flexible structure. Zhao [34] claims that this method can never provide exactly zero tracking error with uncertainty in the plant, yet Oda [24] still demonstrates its successful use in compensating for disturbances causing unwanted rigid body motion.

This work makes use of feedforward control to compensate for the basebody disturbing effect of the World View imaging instrument, preventing excitation of the low frequency solar array modes.

A fundamental understanding of the closed loop control-structure interaction problem is provided by Spanos [29] with an analytical evaluation of a simple gyro-reaction wheel feedback loop using a PD controller and a simple two degree of freedom model. Kaplow and Velman [13] propose a design concept in which the "dirty" disturbances sources are structurally separated from the "quiet" performance instruments and sensors, connected only by an active isolation device. The applicability of this concept, however, is highly dependent on spacecraft topology and the Clark spacecraft is not well suited for such a concept. A somewhat successful attempt to attenuate solar array vibration on the Clark satellite uses attitude rate feedback to the reaction wheels together with a double lag compensator.

The high frequency structural vibration that occurs in the cantilevered World View support strut is a good candidate for control using piezoceramics. Bailey and Hubbard [4] demonstrated successful use of piezoelectric material to actively damp out vibrations on a cantilevered beam and Hagood and von Flotow [11] demonstrated the same but using passive electric networks. This work uses a piezoceramic actuator model [7] to form a simple closed loop feedback controller with a beam tip velocity output and actuated root strain input.

1.3 Thesis Overview

Chapter 2 describes the Clark spacecraft and develops the input-output structural finite element model to be used in simulations. Starting from a finite element model data deck supplied by Lockheed-Martin, a representative state space model is developed using NASTRAN's eigenvalue and mode shape solution. The control, disturbance, performance and measurement variables forming the inputs and outputs of the model are specified and appropriate changes are made to the finite element model to

accommodate them. Finally, the 268 state model is reduced to a smaller model using modal cost analysis.

In Chapter 3, a model of the World View stepper motors is created and used to simulate the effects of their motion on the World View pointing performance. A brief description of stepper motor operation is given and the state space model is modified to represent the stepper motors as relative displacement rather than torque actuators. Theoretical World View slew magnitudes are presented and two slew command profiles are presented: one that ignores the individual motor steps and one that attempts to model it. Both command profiles are used to form simulated spacecraft responses which are then compared to performance specifications.

Chapter 4 consists of an investigation of thermal snap and its effects on the Clark spacecraft. The physical phenomenon of thermal snap is explained in detail and a new method of modeling is presented which uses externally applied but momentum conserving torques and forces to form the thermally deflected shape. This model is applied to a Clark solar array using some simplifying assumptions and then simulated on the state space model to obtain performance responses that are compared to specifications.

Chapter 5 presents two open loop and two closed loop compensation methods to attenuate the effect of the World View and thermal snap disturbances. Input shaping is successfully applied on the World View slew command to reduce the low frequency vibration due to the solar arrays but is unsuccessful in reducing the high frequency vibration due to the World View support strut. The World View slew command is used as a feedforward signal in actuating a reaction wheel on the spacecraft bus to successfully eliminate low frequency vibration by counteracting the World View stepper motor's reaction torque. For closed loop control, rate feedback is implemented using attitude rate from the spacecraft bus gyro fed to the reaction wheel torque, but with an intervening double lag compensator to gain stabilize high frequency bus modes. This method achieves limited reduction of low frequency vibration caused by both World View and thermal snap. Another controller is formed using a piezoceramic actuator at the root and an accelerometer at the tip of the World View support

strut. This rate feedback loop from tip velocity to root actuated strain successfully attenuates the high frequency vibrations as designed.

Chapter 2

Spacecraft Model

This chapter describes the Clark spacecraft and the finite element model used in subsequent analyses.

2.1 Background

The Clark spacecraft, for which CTA Space Systems and Lockheed Martin are prime contractors, is part of NASA's Small Satellite Technology Initiative (SSTI) program created in the early 1990's to encourage industry to develop spacecraft in a more economical and less time consuming fashion. The Clark spacecraft is designed primarily as an Earth Observing Satellite (EOS), with most hardware acquired as off-the-shelf commercial products, in order to save money, development time, and demonstrate their technological maturity. Instruments on board include an X-ray spectrometer, a sensor to map air pollution called μMaps, an atmospheric tomography instrument called ATOMS, and an earth imaging instrument called World View (WV). Among all the instruments, the World View imaging instrument has the most stringent pointing performance specifications of 5.7 mdeg reporting accuracy, 4 $\frac{\text{mdeg}}{\text{s}}$ over 10 second stability and 143 μdeg jitter. The slewing of a mirror by the World View instrument and the occurrence of solar array thermal snap are primary disturbance sources which may cause exceedance of the performance specifications. This warrants development of a spacecraft model with the necessary inputs and outputs to simulate disturbance

effects and to determine methods of compensation. Figure 2-1 shows a conceptual picture of the Clark spacecraft.

2.2 Finite Element Model

In order to analytically predict the behavior of the spacecraft, a finite element model is used which captures all the important structural characteristics of the real structure with sufficient fidelity and which is simultaneously as simple as possible.

The models of the Clark satellite used in preparing this work are NASTRAN finite element models, all acquired from CTA Space Systems and Lockheed-Martin. The models represent the structure using various simple structural elements: beams, bars, rods, springs, quadrilateral and triangular plates and shells, concentrated masses and inertias and rigid elements. Each element is associated with a certain number of nodes: two at the ends of beams, bars, rods and springs; four at the corners of plates and shells; one at the location of each concentrated mass or inertia, and an arbitrary number for each rigid element which rigidly connects the nodes. Each node forms the common junction which connects element to element, with each node possessing 6 degrees of freedom, three translational and three rotational. The final model is a highly detailed, $4,500$ node, $27,000$ degree of freedom model representing all masses, inertias, and flexible elements. No mechanisms were initially included to model moving parts such as the World View gimbals, the reaction wheels, the solar array mechanisms or the solar array drives. Figure 2-2 shows the NASTRAN finite element model of the Clark spacecraft in the form of elements.

A NASTRAN eigenvalue solution of this finite element model results in a list of eigenvalues and corresponding mass-normalized eigenvectors or mode shapes that lie in a specified bandwidth. MATLAB, a software tool especially convenient for mathematical manipulation and simulation of dynamic systems, is now used for further analysis. The eigenvalues are imported into MATLAB as a diagonal matrix $\mathbf{\Omega}$ and the mode shapes are organized into a matrix $\Phi \in \mathbb{R}^{m \times n}$ where m is the total number

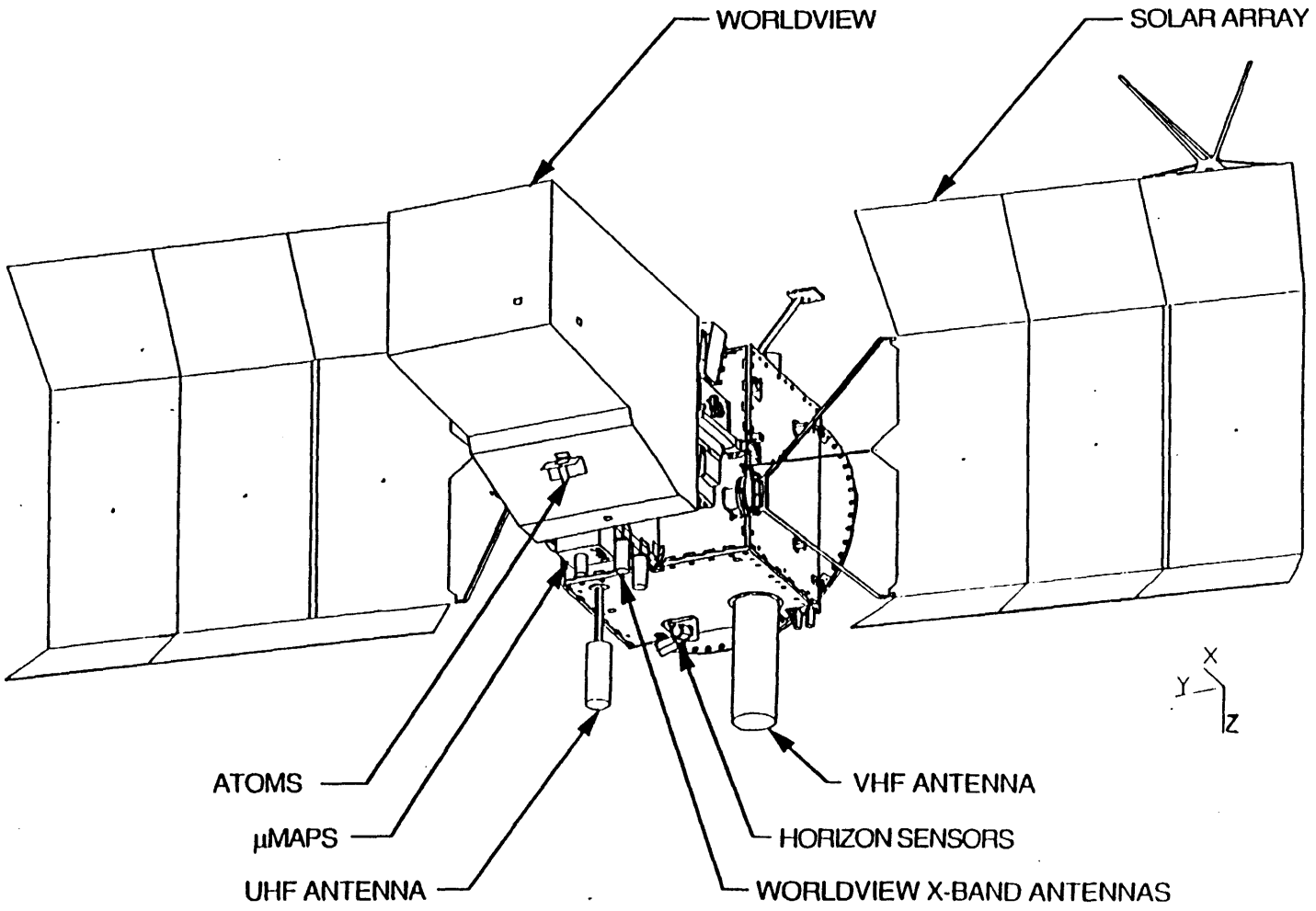

Figure 2-1: Conceptual picture of the Clark spacecraft.

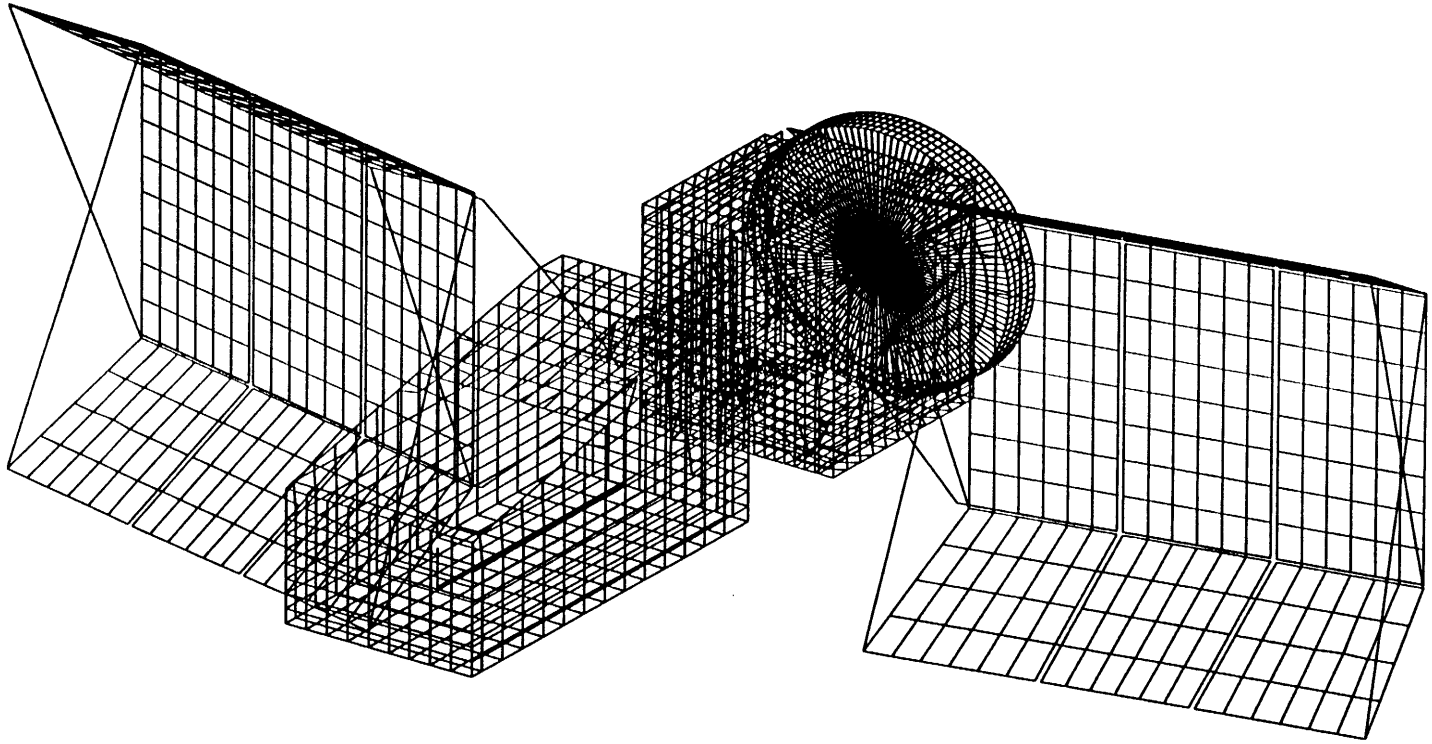

Figure 2-2: Element depiction of the NASTRAN finite element model of the Clark spacecraft.

of degrees of freedom and n is the number of modes or eigenvalues. Each row of Φ represents the participation of degree of freedom i from node j in modes $1 \ldots n$.

The equation governing the structural dynamics of the spacecraft can be written as

$$M\ddot{\boldsymbol{q}} + D\dot{\boldsymbol{q}} + K\boldsymbol{q} = Q\boldsymbol{f} \tag{2.1}$$

where the state vector $\boldsymbol{q}$ represents the displacement and rotation degrees of freedom of each node and the inputs $\boldsymbol{f}$ are forces and moments. Using Φ to transform the physical state vector into a modal one by substituting the relation $\boldsymbol{q} = \Phi\eta$ into Equation (2.1), and then premultiplying by Φ^{T}, produces

$$\Phi^{\mathrm{T}}M\Phi\ddot{\boldsymbol{\eta}} + \Phi^{\mathrm{T}}D\Phi\dot{\boldsymbol{\eta}} + \Phi^{\mathrm{T}}K\Phi\boldsymbol{\eta} = \Phi^{\mathrm{T}}Q\boldsymbol{f} \tag{2.2}$$

Premultiply by $\Phi^{\mathrm{T}}M^{-1}\Phi$ further produces

$$\ddot{\boldsymbol{\eta}} + D^*\dot{\boldsymbol{\eta}} + K^*\boldsymbol{\eta} = Q^*\boldsymbol{f} \tag{2.3}$$

where

$$K^* = \Omega^2 = \begin{bmatrix} \omega_1^2 & 0 & \cdots & 0 \\ 0 & \omega_2^2 & & \vdots \\ \vdots & & \ddots & 0 \\ 0 & \cdots & 0 & \omega_n^2 \end{bmatrix}, \; D^* = 2Z\Omega \equiv \begin{bmatrix} 2\zeta_1\omega_1 & 0 & \cdots & 0 \\ 0 & 2\zeta_2\omega_2 & & \vdots \\ \vdots & & \ddots & 0 \\ 0 & \cdots & 0 & 2\zeta_n\omega_n \end{bmatrix} \tag{2.4}$$

and the columns of Q^* consist of rows or combinations of rows of Φ. Note that that the diagonal form of D^* implies an assumption of uncoupled, modal damping, which is not generally true.

At this point the damping values $\zeta_1 \ldots \zeta_n$ can be conveniently assigned for each mode. Most flexible structures have damping ratios that range from about 0.1-1%. Modal tests on the MIT interferometer testbed resulted in damping ratios of 0.5-2.8% [3] and tests on the MIT Middeck Active Control Experiment resulted in larger values of 0.9-10% [9] due to actuators, sensors, wiring. A conservative, uniform

damping ratio of 0.5% is assumed for all the modes of the Clark model. The next step is to rewrite this second-order differential equation as an equivalent first-order differential equation in state-space form:

$$\begin{Bmatrix} \dot{\boldsymbol{\eta}} \\ \ddot{\boldsymbol{\eta}} \end{Bmatrix} = \begin{bmatrix} 0 & I \\ -\Omega^2 & -2Z\Omega \end{bmatrix} \begin{Bmatrix} \boldsymbol{\eta} \\ \dot{\boldsymbol{\eta}} \end{Bmatrix} + \begin{bmatrix} 0 \\ Q^* \end{bmatrix} \boldsymbol{f} \tag{2.5}$$

which can be rewritten as

$$\dot{\boldsymbol{x}} = A\boldsymbol{x} + B\boldsymbol{f} \tag{2.6}$$

where

$$A = \begin{bmatrix} 0 & I \\ -\Omega^2 & -2Z\Omega \end{bmatrix}, B = \begin{bmatrix} 0 \\ Q^* \end{bmatrix}, \boldsymbol{x} = \begin{Bmatrix} \boldsymbol{\eta} \\ \dot{\boldsymbol{\eta}} \end{Bmatrix} \tag{2.7}$$

This final equation describing the behavior of the structure makes it convenient to transport the eigenvalues and eigenvectors from NASTRAN into MATLAB in order to analyze the problem with existing tools.

2.3 Inputs and Outputs

In order to use the structural model for simulations and make quantified statements about its behavior, all control inputs $\boldsymbol{u}$, disturbance inputs $\boldsymbol{w}$, measured outputs $\boldsymbol{y}$ and performance outputs $\boldsymbol{z}$ must be identified. Each of the instruments on board the spacecraft has performance specifications that could be used to formulate a performance output. The World View instrument has the most stringent specifications, defined in terms of angular reporting accuracy, stability and jitter. A schematic of the World View instrument is shown in Figure 2-3. Reporting accuracy is interpreted as how well the measured angle agrees with the actual angle, specified as better than 5.7 mdeg. Stability is interpreted as a limit on the angular rate, limited to 4.0 $\frac{\text{mdeg}}{\text{s}}$. Jitter is a way of measuring high frequency vibration. The definition of jitter is the largest relative angular perturbation in a fixed length of time. The World View jitter specification is 143 μdeg in 2 msec. These three measures are all defined in terms of deviation from the World View instrument's intended line-of-sight to the ground.

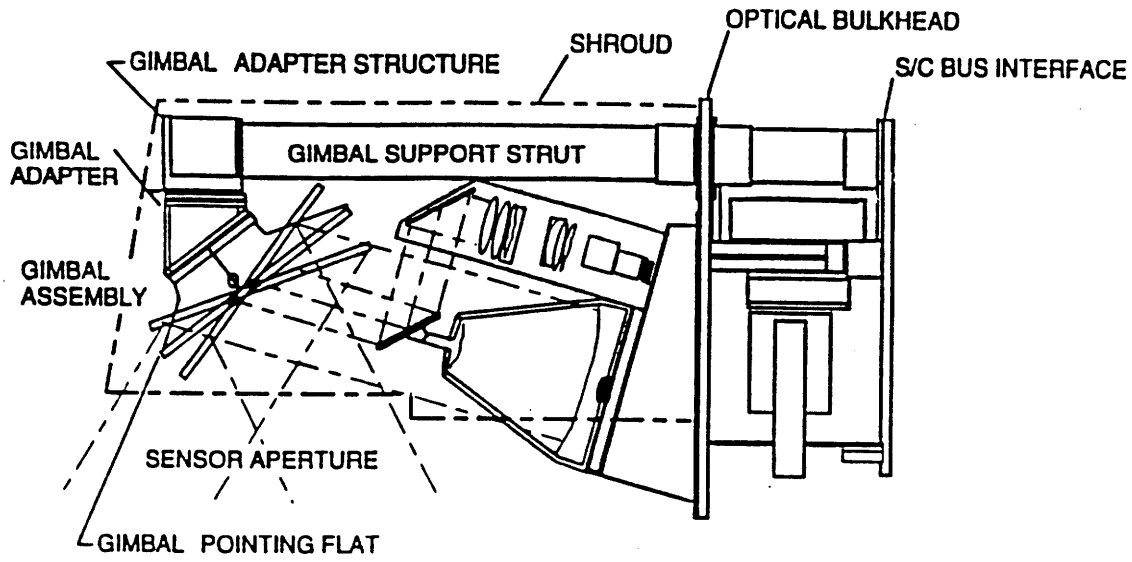

Figure 2-3: The World View instrument. Courtesy of CTA Space Systems and Lockheed-Martin.

Figure 2-4 aids in the following explanation. Deviation from the line-of-sight, represented by rotations about the ground axes X_G and Y_G, arise principally from four angular perturbations: the light-collecting optics about Y_O and Z_O and the reflecting mirror about X_M and Z_M. Assuming the mirror is at a 45 deg angle from the line-of-sight and all angular perturbations are small, the two line-of-sight error angles can be expressed as a function of the four angular perturbations. This can be derived by separately considering the effect of each of the four angular perturbations on X_G and Y_G. Thus, a unit rotation of the optics about Y_O causes no angular deviation about X_G and a negative unit deviation about Y_G. After doing the same for the other three angular perturbations, the resulting relationship is

$$\begin{Bmatrix} X_G \\ Y_G \end{Bmatrix} = \begin{bmatrix} 0 & 1 & \sqrt{2} & 0 \\ -1 & 0 & 0 & 2 \end{bmatrix} \begin{Bmatrix} Y_O \\ Z_O \\ X_M \\ Z_M \end{Bmatrix} \tag{2.8}$$

Equation (2.8) is used to derive the World View line-of-sight error about X_G and Y_G given the four perturbation angles from the simulation. Thus, the performance

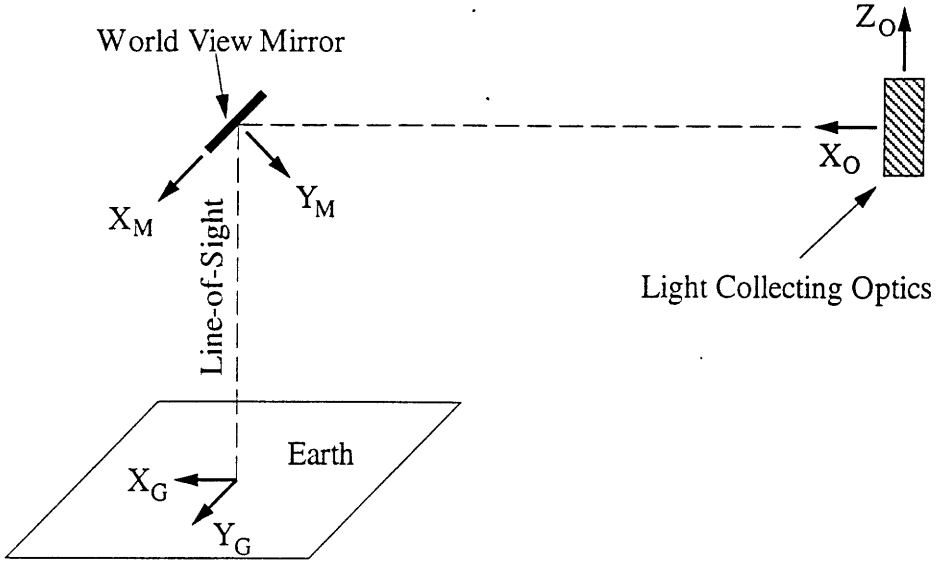

Figure 2-4: Coordinate systems representing the World View light collecting optics, the reflecting mirror at the tip of the World View support, and the viewing point on the ground. Y_O and Z_M point out of the paper.

metric $\boldsymbol{z}$ is now defined as the World View line-of-sight reporting accuracy, stability and jitter. These are expressed in raw form about the two axes X_G and Y_G, but compared to the performance specifications as single RMS values.

The only significant disturbance input $\boldsymbol{w}$ considered for this spacecraft is the phenomenon of thermal snap. Other disturbances such as solar wind due sun activity, atmospheric drag and the earth's magnetic field are many orders of magnitude smaller than thermal snap. It is possible that the World View instrument will be imaging during or near sunrise or sunset, and it is precisely at these moments that thermal snap often occurs, propagating vibration originating from the solar arrays to the rest of the spacecraft. Modeling this will require a minimum of one input. Details of modeling thermal snap are discussed in Chapter 4.

The output measurements $\boldsymbol{y}$ will be used for either feedback control purposes or monitoring a particular measurement. Three gyro measurement outputs will be used for closed loop control of the spacecraft attitude. Currently the spacecraft has a closed loop bandwidth of 0.1 Hz designed to prevent any control-structure interaction with

the structural modes. This normally would mean that there should be no need for modeling a gyro output since the effects of such a low bandwidth loop are negligible. In Section 5.2.1, however, the gyros are used for closed loop control to help attenuate low frequency disturbance effects, thus requiring them to be modeled. In addition, the reaction wheel velocities must be monitored to prevent excessively high spin rates. Thus the output $\boldsymbol{y}$ consists of the gyro and the reaction wheel outputs.

There are ten possible control inputs $\boldsymbol{u}$ to consider for this spacecraft: two for slewing the World View instrument about its two axes, two for slewing the solar arrays, three for controlling the reaction wheels, and three for controlling the thrusters. The thruster is not modeled because the performance variables are not measured when the thruster is slewing the spacecraft. The slewing of the solar arrays might significantly affect the performance since they are actuated throughout imaging periods, but they also will not be modeled. The five control inputs $\boldsymbol{u}$ to be modeled are the two for World View and three for the reaction wheels.

The definition of these inputs and outputs allows a more complete description of the model to be written as

$$\begin{aligned} \dot{\boldsymbol{x}} &= A\boldsymbol{x} + B\boldsymbol{f} = A\boldsymbol{x} + [B_u \; B_w] \begin{bmatrix} \boldsymbol{u} \\ \boldsymbol{w} \end{bmatrix} \\ \begin{Bmatrix} \boldsymbol{y} \\ \boldsymbol{z} \end{Bmatrix} &= C\boldsymbol{x} = \begin{bmatrix} C_y \\ C_z \end{bmatrix} \boldsymbol{x} \end{aligned} \tag{2.9}$$

2.4 Changes to the NASTRAN Model

The control inputs chosen for this spacecraft are all relative torque inputs, meaning that opposite and equal torques are applied to the two sides of the rotating mechanism, the reaction wheel and its housing, for example. In order to model these rigid body modes, five rotational mechanisms must be introduced into the finite element model. This is accomplished in a manner much like that presented by Glaese [9].

A reaction wheel is modeled by adding a new node collocated with the existing, structurally attached node which represents the location of the reaction wheel on the spacecraft bus. The degrees of freedom of this additional node are then constrained to

follow the bus node, except for the desired rotational degree of freedom which serves as the mechanism. Three of these are created for the three orthogonal reaction wheels. The corresponding rotational inertia values must then be added to the new grid points in order to have well defined mechanisms. The inertia values are analytically calculated from the reaction wheel masses and estimated mass distributions.

The two World View gimbals are modeled similarly. There is the additional complication that the two axes of rotation do not line up with the global coordinate system, requiring the creation of a new local coordinate system for these two pairs of nodes, as already mentioned in the previous section. The rotational inertia values for these two new nodes are also calculated analytically using the mass, center of gravity locations and physical dimensions of the gimbal elements, assuming a uniform mass distribution.

2.5 Model Reduction

A finite element model of such high fidelity as this one requires that the model be reduced so that simulations and analyses can be performed in reasonable times. A two-step approach will be used to reduce the model to a manageable size.

2.5.1 Model Reduction Method

There are many methods available in the literature which may be used to reduce the model. Balanced reduction [10] and modal cost analysis [28] are two well established. Each has advantages and disadvantages. Both methods require the system to be lightly damped and stable, meaning that any rigid body dynamics must be removed from the system before the reduction and added afterwards. This is done when the system is in modal form, since the states are uncoupled and can easily be separated.

Balanced reduction takes any given system and transforms the system such that the controllability and observability grammians are equal, or balanced. In this form the Hankel singular values represent the relative importance of each of the new states, allowing a ranking and subsequent elimination of those states whose singular values

are below a certain threshold value. Variations on this method have been made very robust and lead to high quality reduced model. Two disadvantages are that it can be very time consuming to find the transformation and that the meaning of the states is changed.

Once the physical meaning of the states is lost through the reduction procedure, transforming the remaining new state variables back to modal states is not equivalent to eliminating particular states directly in modal form. This is rarely an issue, but a World View input modification procedure discussed in Section 3.1.2 requires that the model be represented in the original modal state form.

A more convenient method of model reduction is modal cost analysis. This method has the advantage of preserving the modal form of the system and simply identifies and eliminates the unobservable/uncontrollable modes by measuring the contribution of each mode to a cost metric. Although balanced reduction may be better for choosing the appropriate states when considering stability, modal cost analysis more accurately shows which modes make a greater contribution to the cost [8]. In addition, the procedure is much faster since no transformation matrix needs to be found. The weighted contribution of each mode to the cost through the various inputs and outputs together with frequency scaling define the cost as

$$V_\alpha = \left(c_\alpha^{\mathrm{T}} W_{yy} c_\alpha + \omega^2 c_\alpha'^{\mathrm{T}} W_{yy} c_\alpha'\right) \frac{\sigma_\alpha^2}{4\zeta_\alpha \omega_\alpha^3}, \quad \alpha = 1 \ldots n \tag{2.10}$$

where

$$\sigma_\alpha^2 = B_\alpha W_{ff} B_\alpha^{\mathrm{T}}$$

$$[c_1 \ldots c_n \; c_1' \ldots c_n'] = C$$

$$\begin{bmatrix} B_1 \\ \vdots \\ B_n \end{bmatrix} = B$$

and W_{ff} and W_{yy} are input and output weighting matrices. The resulting costs V_α are plotted as a function of the number of states and all states lying below a certain cost

are discarded. A comparison of the Bode plots of the reduced-order and full-order model helps to verify that important dynamics have been retained.

2.5.2 Reduction Procedure

Preliminary NASTRAN solutions with a less detailed finite element model showed significant flexible modes up to at least 36 Hz, so it was decided to solve using a bandwidth of 0-100 Hz to capture any other possibly significant modes. A NASTRAN solution of the complete model gives 268 modes within this bandwidth. Figure 2-5 shows the frequency distribution of the all the modes. Many of these modes are nearly unobservable and/or uncontrollable by the complete set of inputs and outputs chosen, so the first model reduction is performed to eliminate them.

The modes remaining after the first reduction are saved as a database and form the basis for simulation and analysis. In most simulations, though, only a small subset of all the available outputs and inputs are actually used, providing the opportunity to even further reduce the model before simulating. After this second model reduction there are typically 25-50 states remaining, depending on the input/output combination chosen. Table 2.1 lists the dominant natural frequencies that impact the performance after reduction.

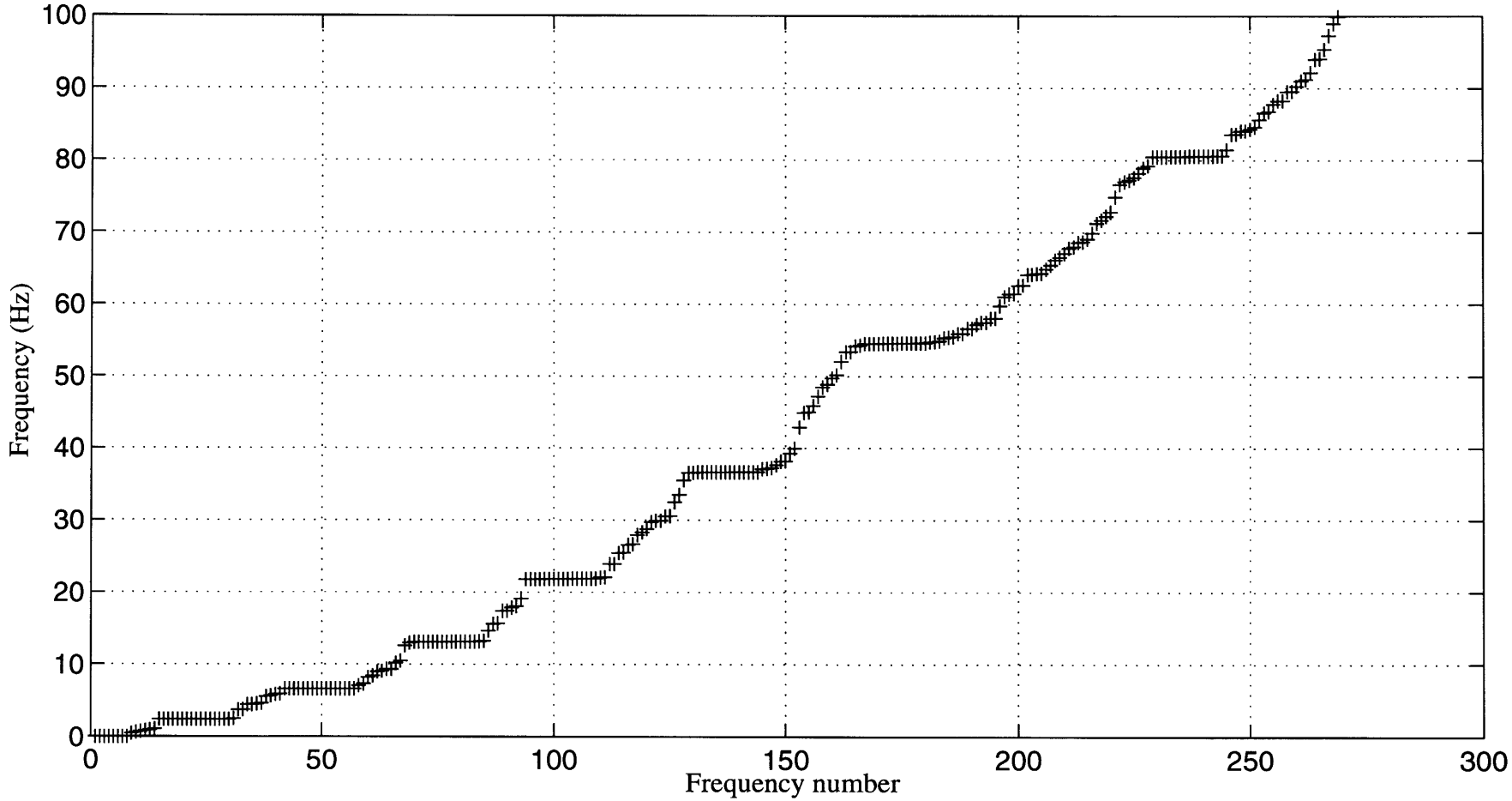

Figure 2-5: Distribution of the spacecraft's 268 structural modes obtained by solving the NASTRAN finite element model.

Table 2.1: Dominant natural frequencies of the Clark spacecraft obtained from NASTRAN.

Frequency (Hz)	Description of Mode About Global Axes
0.644	1st solar array bending about Z, anti-symmetric
0.914	1st solar array torsional about Y, symmetric
0.939	2nd solar array torsional about Y, anti-symmtric
1.176	1st solar array bending about X, symmetric
26.64	1st World View support bending about Z
38.17	1st World View support bending about Y

Chapter 3

Disturbance Effect of World View

This chapter investigates the effect of World View's slewing motions on its pointing ability. The World View commercial earth viewing instrument, a product of the World View Imaging Corporation, creates photographs of the earth from low earth orbit by piecing together many individual frames. In order to produce these single frames, two stepper motors repeatedly slew a two-degree-of-freedom mirror to point at each target area. This stepping process is one of the major sources of disturbance which excites the dynamics of the entire spacecraft and affects the pointing performance.

3.1 Modeling of the Stepper Motor

3.1.1 Microstepping vs. Full-Steps

A typical stepper motor can be moved in one of two ways. The simplest is to sequentially excite the phase windings with the constant, rated current, causing the motor to move a full step length with the excitation of each phase. Advantages of this scheme are simplicity of operation and low cost, while disadvantages are a physical limit to the position resolution and a tendency to exhibit significant mechanical resonance.

Using the method of microstepping, the phase windings are excited simultaneously with sinusoidally varying currents. The motor therefore takes a position that varies with the current. The advantage is the ability to greatly improve the position

resolution, but it comes at the cost of having to excite the winding currents at many different levels. Achieving an exact microstep size requires very accurate current levels and often the presence of disturbances and loads on the motor output shaft requires position feedback to guarantee single microstep accuracy [1]. The World View stepper motors make use of the latter method, including the use of position feedback, with a full step length of 1.8 deg, a microstep length of 0.025 deg, and an additional motor gear reduction of 10:1. Therefore, for every microstep the motor takes, the mirror takes a step of 0.0025 deg.

3.1.2 Transformation of Torque Inputs

There are two approaches to commanding a motor slew. A typical method is to create closed loop feedback using measured position and rate outputs and actuating a relative torque input. This method requires choosing a feedback controller and determining the appropriate controller parameters in order to correctly model the behavior of the motor together with its load. A less complicated method takes advantage of the fact that stepper motors, by their very nature, move in fixed, regular steps. This characteristic means that a stepper motor can be modeled as a displacement actuator rather than a torque actuator. Modeling the input as a displacement actuator requires transforming the relative *torque* input that affects the free rotational degrees of freedom in the gimbal mechanisms into a relative *displacement* input.

In order to transform the relative torque inputs into some form of relative displacements, Equation (2.3) is rewritten as

$$\ddot{\boldsymbol{\eta}} + D^*\dot{\boldsymbol{\eta}} + K^*\boldsymbol{\eta} = Q_1^*\mathbf{u_1} + Q_2^*\mathbf{u_2} \tag{3.1}$$

where $\mathbf{u_1}$ are the inputs that are to be preserved and $\mathbf{u_2}$ are the inputs to be transformed. Define a new relative displacement input, $\mathbf{d} = \phi\boldsymbol{\eta}$, where ϕ is a linear combination of two rows of Φ which correspond to the free rotational degrees of freedom of the two collocated mechanism nodes in the finite element model. Multiplying

Equation (3.1) by ϕ produces

$$\ddot{\mathbf{d}} + \phi D^* \dot{\boldsymbol{\eta}} + \phi K^* \boldsymbol{\eta} = \phi Q_1^* \mathbf{u_1} + \phi Q_2^* \mathbf{u_2} \tag{3.2}$$

Solving for $\mathbf{u_2}$, the torques to eliminate, results in

$$\mathbf{u_2} = [\phi Q_2^*]^{-1} \left[\ddot{\mathbf{d}} + \phi D^* \dot{\boldsymbol{\eta}} + \phi K^* \boldsymbol{\eta} - \phi Q_1^* \mathbf{u_1} \right] \tag{3.3}$$

Setting $N = [\phi Q_2^*]^{-1}$ and substituting Equation (3.3) into Equation (3.1), the final result becomes

$$\ddot{\boldsymbol{\eta}} + [I - Q_2^* N \phi] D^* \dot{\boldsymbol{\eta}} + [I - Q_2^* N \phi] K^* \boldsymbol{\eta} = [Q_1^* - Q_2^* N \phi Q_1^*] \mathbf{u_1} + Q_2^* N \ddot{\mathbf{d}} \tag{3.4}$$

Note that the newly defined input, $\mathbf{d}$, is now expressed as a second derivative, requiring a *relative angular acceleration input.*

Although K^* and D^* are diagonal matrices, the term $Q_2^* N \phi$ will not be strictly diagonal, causing coupling between the the modal states. The model reduction process in Section 2.5.1 included a separation of rigid body modes from flexible ones under the assumption that the states were uncoupled. Since the procedure of transforming relative torque to relative angular acceleration introduces modal coupling and thus prevents a simple separation of the rigid body modes, the transformation must be performed only *after* model reduction.

3.2 Slew Profile

The motion of a stepper motor from one position to another can be separated into three distinct sections: acceleration, maximum constant velocity, and deceleration. Acceleration and deceleration are controlled in practice by varying the stepping rate between zero and the maximum stepping rate. The maximum constant velocity is directly proportional to the maximum stepping rate which is usually a function of the software and hardware used to drive the motor.

Table 3.1: Angular displacements of the World View mirror required by World View.

Field of View	Slew About X_{WV} Axis	Slew About Z_{WV} Axis
Narrow	0.70 deg in 0.5 sec	0.35 deg in 0.5 sec
Wide	3.6 deg in 0.7 sec	1.8 deg in 0.5 sec

World View can capture image frames of two different sizes: a narrow field of view = 6 square km and a wide field of view = 30 square km. Since the spacecraft orbits at an altitude of 475 km, it easy to then calculate the required stepper motor slew sizes. They are shown in Table 3.1, together with the maximum time allowed for the slew.

3.2.1 Smooth Profile

A simple method of creating the relative angular acceleration input is to assume a square pulse profile. In this case, the resulting position profile can be determined by adjusting three parameters: the magnitude of the pulse, the duration of the pulse and the length of time between the positive and negative portions of the pulse. Such an acceleration profile results in a velocity profile which is trapezoidal and a position profile which is quadratic-linear-quadratic.

Figure 3-1 shows a typical square wave input of the relative angular acceleration and the resulting relative angular displacement profile. Given $\dot{\mathbf{d}}_{\mathbf{max}}$, the maximum relative angular velocity; t_f, the total slew time as shown in Figure 3-1; and $\mathbf{d}$, it becomes possible to iteratively solve for the appropriate t_1 and t_2. The result is a relatively simple input which represents the overall slew profile but does not attempt to model the individual discrete steps.

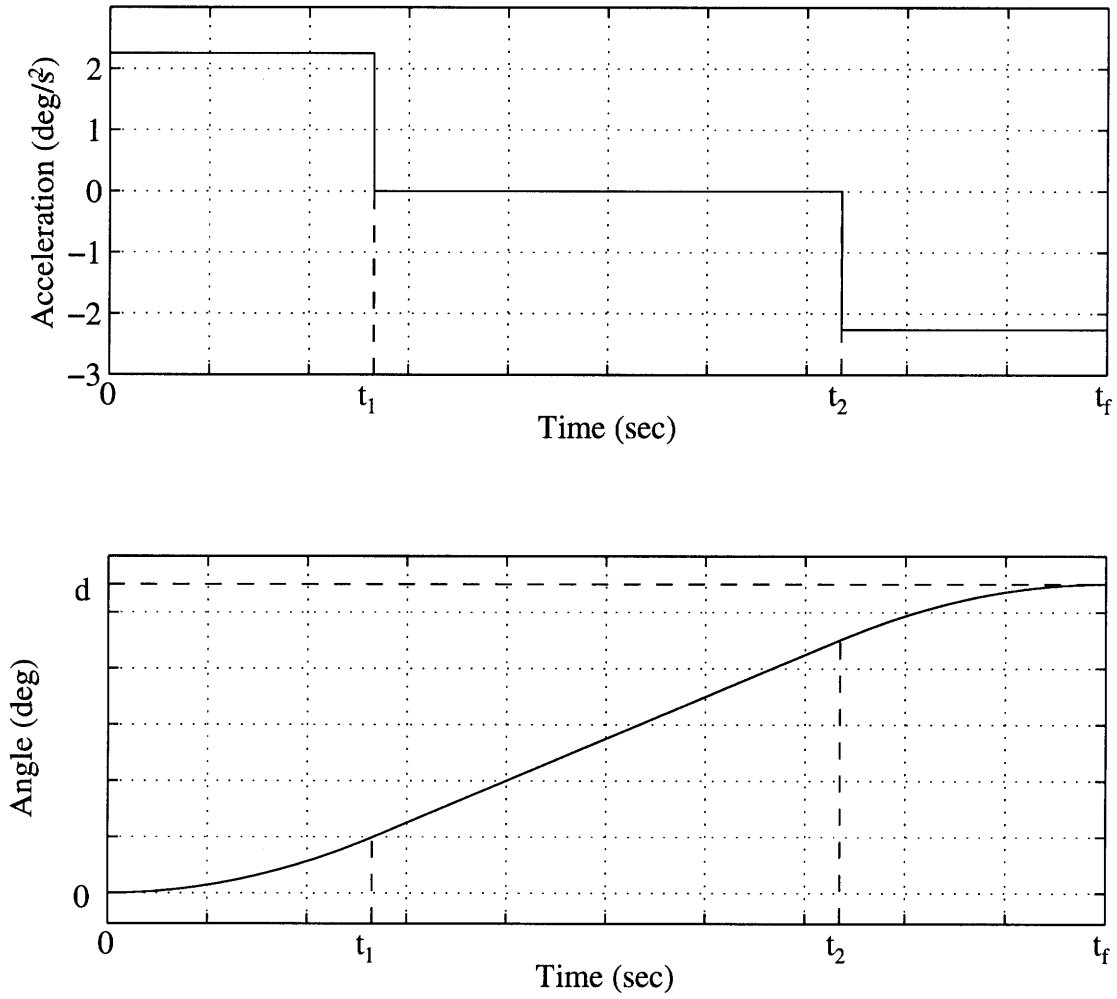

Figure 3-1: Smooth input command used for World View slewing motion and the resulting relative angular displacement.

3.2.2 Discrete Profile

A more accurate model of the stepper motor involves modeling each of the individual microsteps that make up a slew motion. Each single microstep can be represented by a pair of opposing impulses for the relative acceleration input.

The first impulse creates an instantaneous non-zero angular velocity and the second opposing one negates the first a short time later, resulting in a predetermined relative angular displacement over the short time interval. The essential numerical parameters that need to be adjusted to give the correct microstep size are the impulse area and the time between the positive and negative impulses. The relationship

between these variables can be written as

$$(\text{impulse area})(\text{time between} \pm \text{impulse}) = \text{microstep size} \tag{3.5}$$

A specific relative angular position profile can then be created by appropriately arranging a series of impulse pairs. The simple way to do this is to use the position profile in Figure 3-1 which results from the smooth acceleration and divide the position axis into discrete steps corresponding to the motor's stepsize. Then simply apply an impulse pair at each time where the smooth curve passes one of these divisions. This process will, of course, create some numerical error since the impulse times generally do not match up with the necessarily, regularly spaced time vector.

Figure 3-2 shows an example of impulse inputs of relative angular acceleration and the resulting relative angular displacement profile. Note that the commanded slew size is the same as in Figure 3-1. The fact that the position profiles in Figure 3-1 and Figure 3-2 are almost identical in shape allows for evaluation of the effects of microstepping with more confidence. Use of impulse pairs as the input carries with it some assumptions and consequences which should be pointed out. This model of stepping assumes that the motor starts from rest and comes to rest with each microstep. The assumption is a valid one as long as the stepping rate of the motor is not too high. As the stepping rate approaches the inverse of the internal response time of the motor, the inertia of the motor begins to prevent the motor from coming to a full stop at each step. It is assumed that the World View stepper motors will not approach this physical limit and therefore this model should be valid.

3.3 Response to World View Commands

The four mirror slew sizes listed in Table 3.1 are used together with MATLAB to create two sets of four different input time histories. The two sets correspond to a smooth and discrete set of inputs. These are used to drive time-domain simulations of the spacecraft's structural dynamic response. The following results are from us-

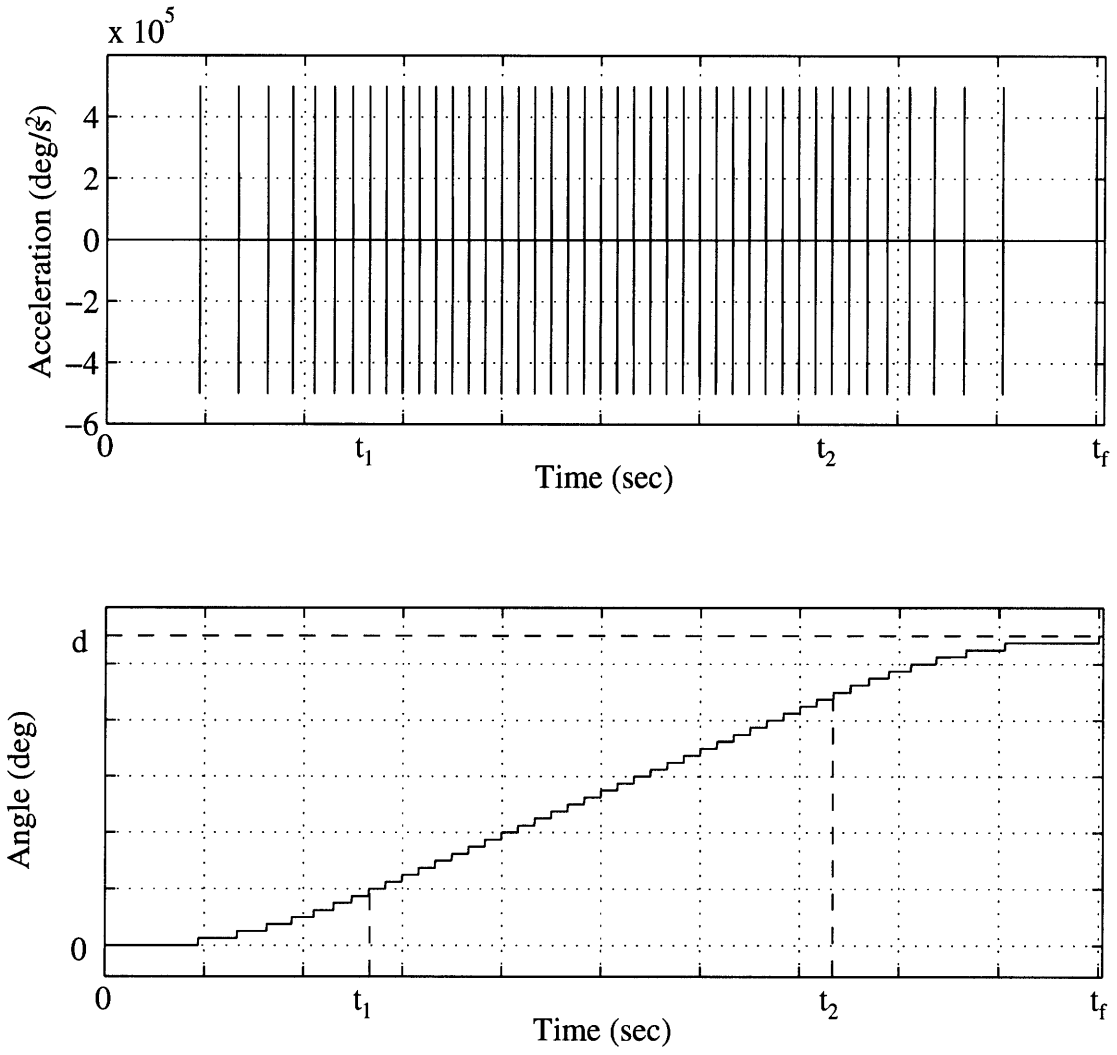

Figure 3-2: Discrete impulse commands used for World View slewing motion and the resulting relative angular displacement.

ing only one of the slew sizes shown in Table 3.1. Appendix A contains the Clark spacecraft's responses to the rest of the input sizes.

Figure 3-3 and Figure 3-4 show the raw spacecraft response to a World View command slewing the mirror 1.8 deg about Z_M in 0.5 seconds, using the smooth input model and the discrete input model, respectively. It should be no surprise that the low frequency portions of Figure 3-3 and Figure 3-4 are practically identical since the slew profile for the smooth and discrete inputs are almost identical. This indicates that the simpler, smooth input model is sufficient to model the low frequency response of the system.

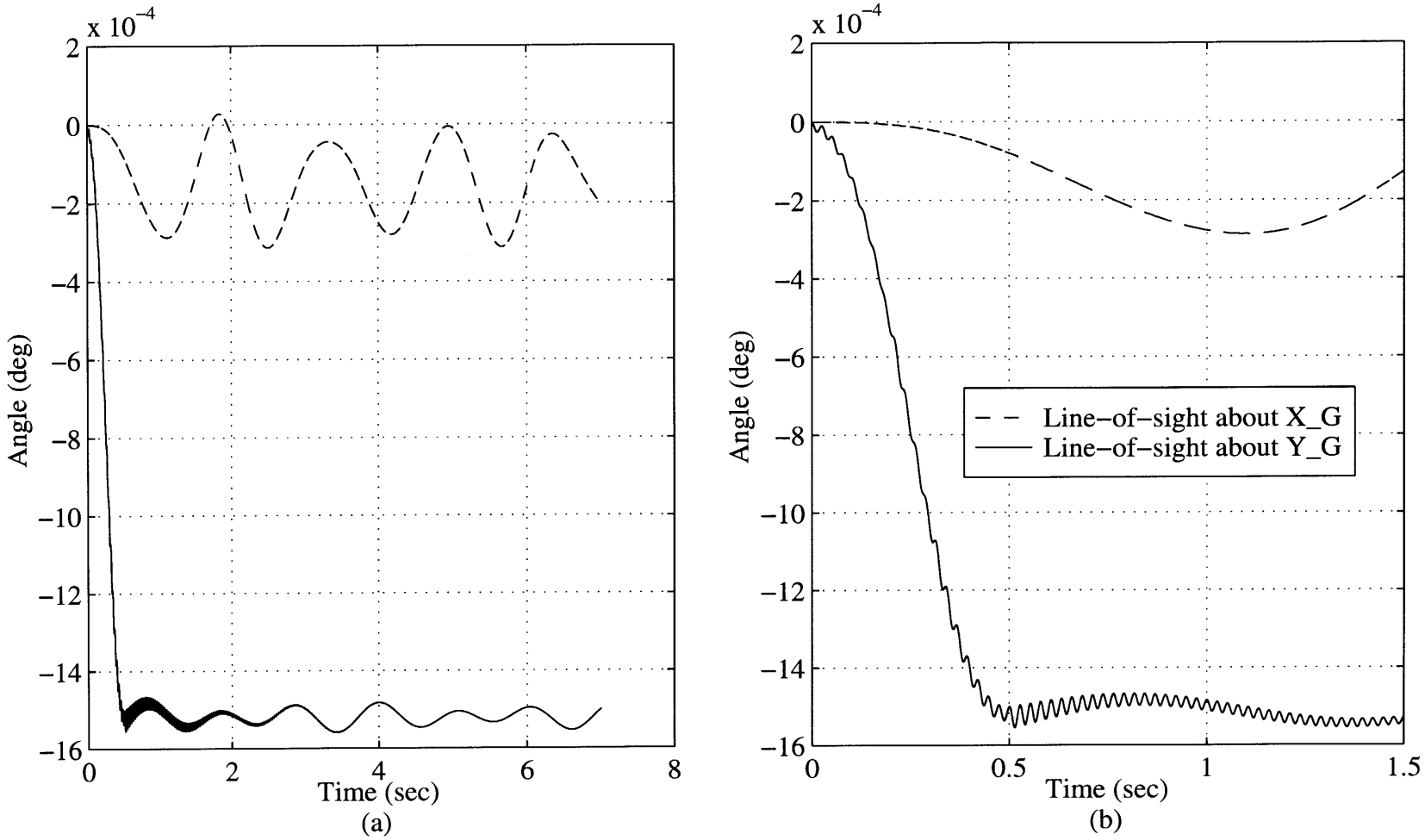

Figure 3-3: World View line-of-sight error about X_G and Y_G due to the *smooth* 1.8 deg Z_M mirror slew in 0.5 seconds. (a) Long term response showing low frequency vibration. (b) Transient response showing high frequency vibration.

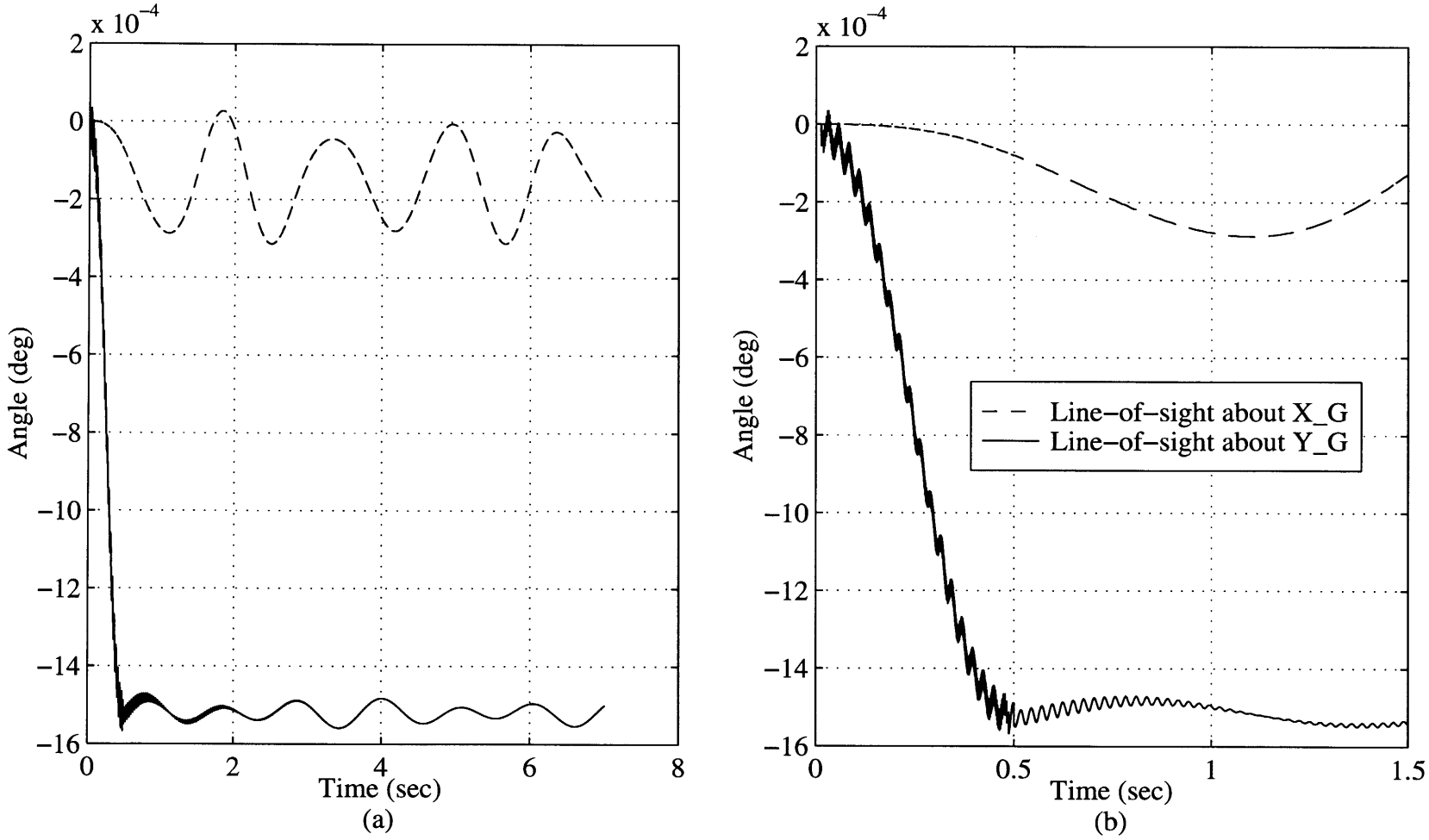

Figure 3-4: World View line-of-sight error about X_G and Y_G due to the *discrete* 1.8 deg Z_M mirror slew in 0.5 seconds. (a) Long term response showing low frequency vibration. (b) Transient response showing high frequency vibration.

The high frequency vibration is approximately the same for both the smooth and discrete inputs of this 1.8 deg slew size. Yet the rest of the inputs from Table 3.1 do not have the same result. A 0.35 deg slew modeled with the discrete input more significantly excites high frequency vibration as shown in Figure A-2 in Appendix A, indicating that detailed stepping action modeled in the discrete input model could be responsible for exciting the higher frequency flexible modes of the spacecraft.

Figure 3-5 and Figure 3-6 show the raw data in processed form to compare with the performance specifications. The accuracy requirement is met equally for both input models but the discrete input causes a violation of the 4 $\frac{\text{mdeg}}{\text{s}}$ stability requirement. The jitter requirement is also met in both cases, but the discrete input causes approximately ten times more jitter.

The majority of motion shown in Figure 3-5a and Figure 3-6a is due to rigid body rotation of the whole spacecraft, and to a lesser extent, low frequency solar array vibration. This is also evident from Figure 3-3 and Figure 3-4.

Appendix A contains the figures that show the results of simulations and comparisons to the performance specifications for the rest of the World View slews listed in Table 3.1. Though the responses differ slightly for the various slews, the conclusions concerning the violation of performance specifications are no different than those reached for the 1.8 deg slew about Z_{M}.

The potential for violating the the reporting accuracy, in general, should be mentioned at this point. Availability of an accurate position sensor is generally not sufficient to guarantee good reporting accuracy. The sensor's bandwidth and the system's sampling frequency are also important parameters. The lowest of the these two parameters sets a limit on the bandwidth of accurate sensor data. If there are observable structural modes at frequencies near or above the lowest of the two parameters, then the actual position of the spacecraft may be very different from latest sensor sample. This is does not seem to be a problem for the Clark spacecraft since the magnitude of vibration is below the 5.7 mdeg specification to start with.

A more serious stability problem exists when any feedback control loop is implemented on a spacecraft with sensor bandwidths including frequencies of significant

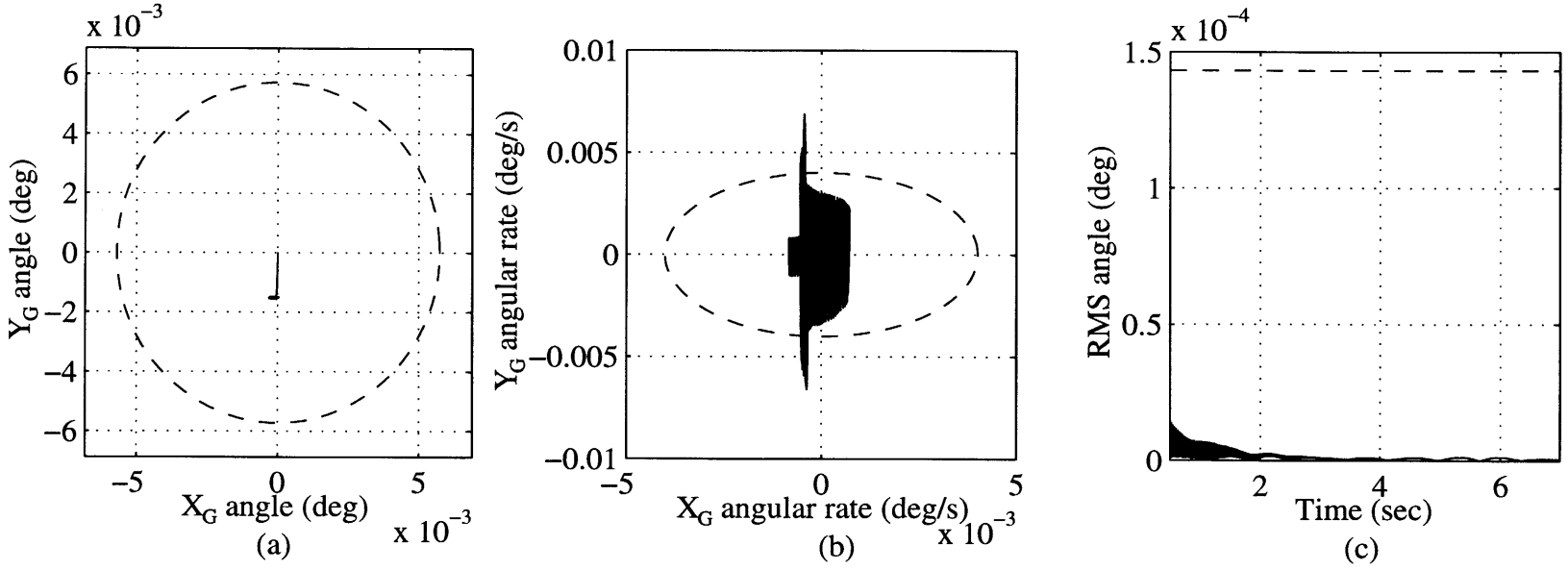

Figure 3-5: Comparison of performance response to the *smooth* 1.8 deg Z_M mirror slew with World View specifications. (a) Line-of-sight accuracy. (b) Line-of-sight stability. (c) Line-of-sight jitter.

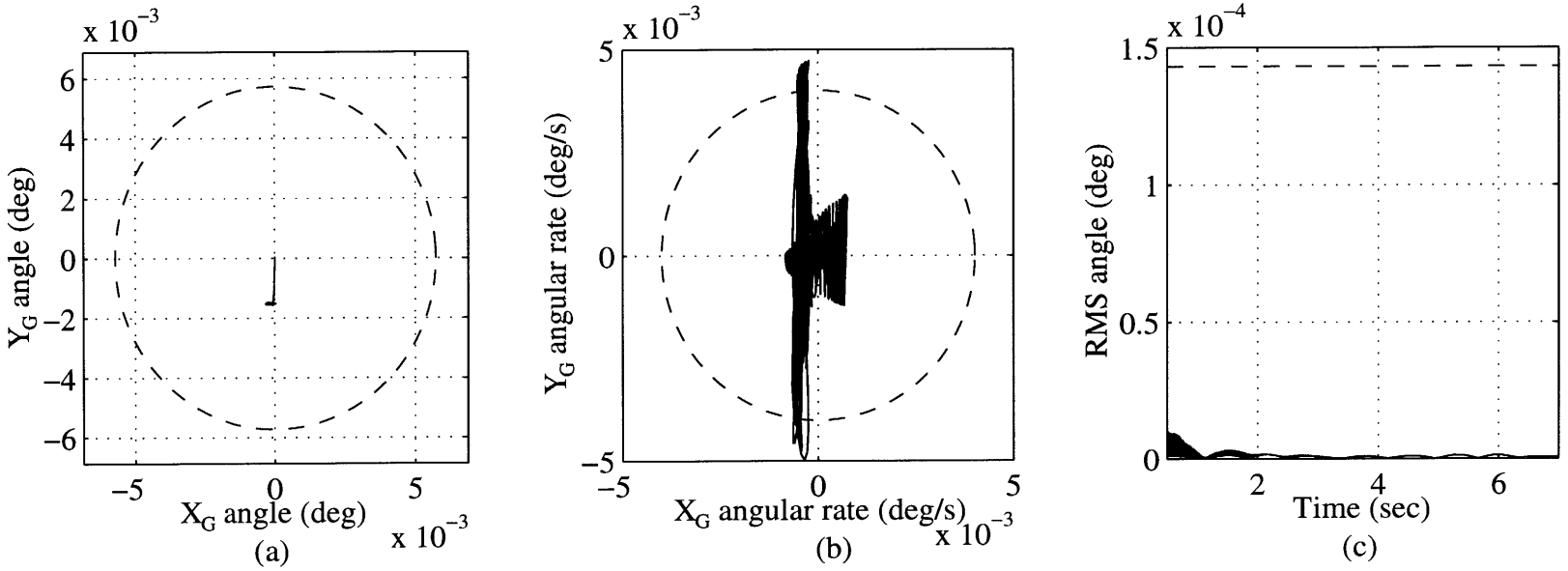

Figure 3-6: Comparison of performance response to the *discrete* 1.8 deg Z_{M} mirror slew with World View specifications. (a) Line-of-sight accuracy. (b) Line-of-sight stability. (c) Line-of-sight jitter.

structural modes. There is a good chance that the controller will drive the system to instability, even if the initial magnitude is very small. It is for this reason that, traditionally, most controller crossover frequencies are set to well below the lowest structural mode of the structure. This, indeed, is the case with the Clark satellite. Isolating the controller bandwidth from dominant structural modes avoids any control structure-interaction and guarantees stability but at the cost of limited performance. Slow system response and poor command following are two such performance limitations. This conflict of control-structure interaction and high performance requirements has led to a great deal of recent study of the problem [8, 22, 29].

Chapter 4

Effects of Thermal Snap

Increasingly stringent pointing requirements of spacecraft over the last few decades have caused thermal snap to become a considerable source of disturbance in numerous spacecraft such as the LANDSAT 4 and 5 [15], the Communications Technology Satellite [35], the Upper Atmospheric Research Satellite (UARS) [15, 20] and the Hubble Space Telescope (HST) [23]. This chapter investigates the phenomena of thermal snap, presents a modeling methodology, and applies it to the Clark spacecraft in order to predict the disturbance effect.

4.1 Background

Thermal snap, as it applies to spacecraft in earth orbit, occurs when the spacecraft moves in and out of the earth's umbra. During such transitions, the spacecraft appendages undergo relatively rapid and large thermal changes. As one side of an appendage cools or heats up relative to the other, it causes a change in the thermal gradient across it and induces thermal strain. The induced thermal strain is proportional to the material's coefficient of thermal expansion α and the change in the thermal gradient ΔT. Assuming the appendage is a uniform, one-dimensional, flexible beam, thermal deformation can be described by

$$\kappa = \frac{1}{\rho} = \frac{\alpha_{cte}\Delta T}{h} \tag{4.1}$$

where κ is the curvature of the beam, ρ is the radius of curvature and h is the beam thickness. This process of straining can happen in two different ways causing two kinds of behavior.

In the most severe case, internal structural or material stiction plays a key role. Internal stiction prevents the realization of thermal strain and causes mechanical stress and strain which cancels out the thermal strain. This stress continues to build up as the thermal gradient changes, storing thermal energy in the form of strain energy until the structure's internal stiction threshold is overcome. At that moment, the stored strain energy is suddenly converted to kinetic energy of motion, causing a large acceleration of the appendage as it now deflects toward its deformed state. The resulting behavior of the appendage is similar to applying a momentum conserving impulse to the structure where most of the structural modes of the appendage will be excited. Note that this process does not depend on how quickly the thermal gradient is changing.

The least severe case carries the assumption that there is no internal stiction present. The appendage will then continuously deform in response to the changing thermal gradient. In this case, the nature of the response depends largely on the first and second derivatives of the thermal gradient as shown by Zimbelman [35]. If the thermal gradient were to change instantaneously the response would be identical to the case where stiction is present. On the other hand, a very gradual change in the thermal gradient causes very little vibratory response of the structure. It seems that such a version of thermal snap would pose no significant disturbance, yet this is not true. The slow deformation of the appendage still applies a disturbing torque to whatever it is attached, usually a satellite bus. Although this is a gradually applied torque, it still causes a rigid body rotation of the satellite bus. Any instruments attached to the bus will experience the same rigid body rotation. If the straining structure has significant enough inertia and mass, then the motion of the bus may be significant and possibly even beyond the authority of the attitude controller.

4.2 Modeling of Thermal Snap

A change in the thermal gradient across an appendage causes a particular deflection shape which we will call a *thermal* mode shape. Substituting this mode shape for $\boldsymbol{q}$ and assuming a unit input $\boldsymbol{f}$ in Equation (2.1), it then becomes

$$K\boldsymbol{q} = Q \tag{4.2}$$

where the dynamic terms in Equation (2.1) are zero, since this $\boldsymbol{q}$ is a final equilibrium state of the structure. Equation (4.2) can then be solved for Q which describes the corresponding distribution of forces and moments.

Having solved for Q, there is one more step before simulating the effect thermal snap on the structure. An input profile of magnitude between zero and one must be created to describe how fast and in what manner the thermal snap occurs. The system response is highly dependent on this input profile. One input form which has an adjustable parameter is

$$\boldsymbol{f} = 1 - e^{-\frac{t}{\tau}} \tag{4.3}$$

A very simple profile would be to let $\tau \to 0$, which causes $\boldsymbol{f}$ to approach a unit step function, corresponding to the most severe case where all the modes will be excited. As $\tau \to \infty$, the transition of $\boldsymbol{f}$ from zero to one becomes very smooth and gradual, corresponding to the least severe case where the response will be least vibratory and approach rigid body-like motion.

In a simple model such as a two dimensional bus and beam structure the thermal mode shape can be analytically obtained and the model size is small enough to easily calculate K for use in Equation (4.2). A thermal model of the Clark satellite's solar arrays was not available and to create one would cost a significant amount of time. Therefore, in order to apply this thermal snap model to the Clark spacecraft and its structural model, some simplifying assumptions will be made.

One assumption is that all deflections will be small such that small angle approximations are valid. The next series of assumptions can best be explained with the

aid of Figure 4-1, a depiction of one of Clark's solar arrays. As Figure 4-1 shows,

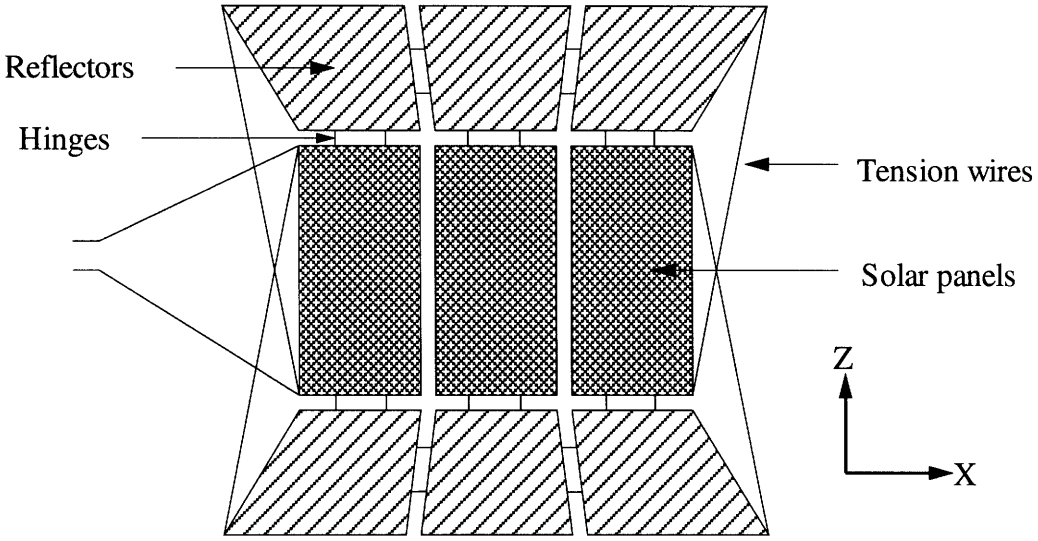

Figure 4-1: A Clark solar array.

the center portion of the structure contains solar panels and the outer panels are reflectors. We will assume that the change in thermal gradient across the reflectors is negligible compared to the gradient across the solar cells. Note that the three solar cell panels are each attached to the reflectors by four hinges, and therefore each can be treated as a plate that is pinned along two opposing edges, neglecting the effects of the tension wires. Realistically, ΔT will cause each plate to bend about both X and Z axes, but it is reasonable to assume that there will be less bending about the Z axis because of the hinges. Therefore, bending about the Z axis is initially ignored in order to further simplify modeling of thermal snap on the Clark. A further assumption is that the cross-sectional properties of each individual solar cell panel are constant. These assumptions and simplifications allow the solar cell panels to be modeled as two dimensional beams, making it possible to analytically obtain a thermal mode shape and solve for Q.

For a two dimensional beam the thermal mode shape is a curve with constant radius as described by Equation (4.1). It is known that a beam in pure bending bending has a constant curvature when the moment is constant along its length, corresponding to pin-pinned sliding boundary conditions with equal and opposite

moment couples at the ends, as shown in Figure 4-2. The specification of moment

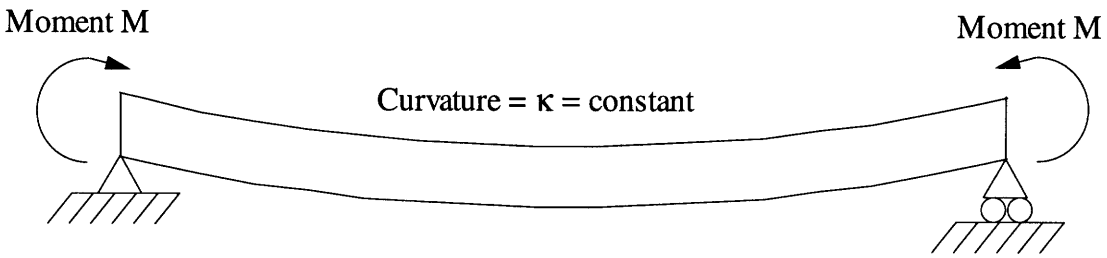

Figure 4-2: A two dimensional beam with boundary conditions and externally applied moments which cause the thermal mode shape.

couples at the ends of the solar cell panels is sufficient information to find Q up to a scaling factor. This scaling factor can be approximated assuming $\alpha = 1 \times 10^{-5}$/deg C, the coefficient of thermal expansion for aluminum, and $\Delta T = 10$ deg C, a reasonable temperature gradient in space [37]. Using these assumptions, the *predicted* thermal strain

$$\varepsilon_{predicted} = \alpha \Delta T \tag{4.4}$$

is then compared to the *modeled* thermal strain computed from simulation of the finite element model

$$\varepsilon_{modeled} = \frac{w'_A - w'_B}{L} h \tag{4.5}$$

where L is the length of the straining section and w'_A and w'_B are the rotation angles at the ends of the straining section. The magnitude of Q is then adjusted so that these two values of strain agree when using a unit input. Until now the panel has been treated as a beam, with bending about the Z axis ignored. Now, this same scaling is applied to unit moment couples about Z. In the final form, moment couples are applied about all edges of the solar panels simultaneously to model the straining of the solar panels due a changing thermal gradient. This procedure should give reliable order-of-magnitude results.

4.3 Spacecraft Response to Thermal Snap

The first response presented is from the simulation of the worst case model of thermal snap where $\boldsymbol{f}$ is a unit step input applied to one solar array, using $\tau = 1 \times 10^{-10}$ sec in Equation (4.3). Figure 4-3 shows the raw spacecraft performance response to this worst case input measured as deviation from the World View intended line-of-sight. Figure 4-4 shows processed raw data compared with the World View performance specifications.

The second response presented uses Equation (4.3) with $\tau = 5$ sec, corresponding to a much smoother input. Figure 4-5 shows the raw data and Figure 4-6 shows the processed data compared with the World View specifications.

Comparing Figure 4-3 and Figure 4-5 it is clear that a slow, gradual straining of the solar array excites the flexible modes very little compared to the sudden straining. Both approach the same final values of rigid body displacement due to thermal strain but the sudden snapping causes additional large amounts of low frequency and also some high frequency vibration. The low frequency vibration is often of greatest concern since it can continue for a long period of time.

Looking at Figure 4-4 and Figure 4-6 we see that most of the specifications are met. The line-of-sight accuracy requirement of 5.7 mdeg is met for both kinds of thermal snap. The line-of-sight stability limit of 4 $\frac{\text{mdeg}}{\text{s}}$ is exceeded in the case of the impulsive thermal snap, but is fine for the gradual thermal snap. In fact, the violation of the stability requirement by impulsive snap is so severe that the dashed line representing the specification is obscured by the data and not visible on the plot. The jitter due to the impulsive thermal snap is several orders of magnitude greater than that resulting from the gradual thermal snap, although both are below the limit of 143 μdeg. These simulations involved only one solar array snapping, but it is quite possible that both solar arrays snap. The time at which the two solar arrays snap, relative to each other, may be significant in determining if the resulting responses are worse or better compared to a single solar array snap.

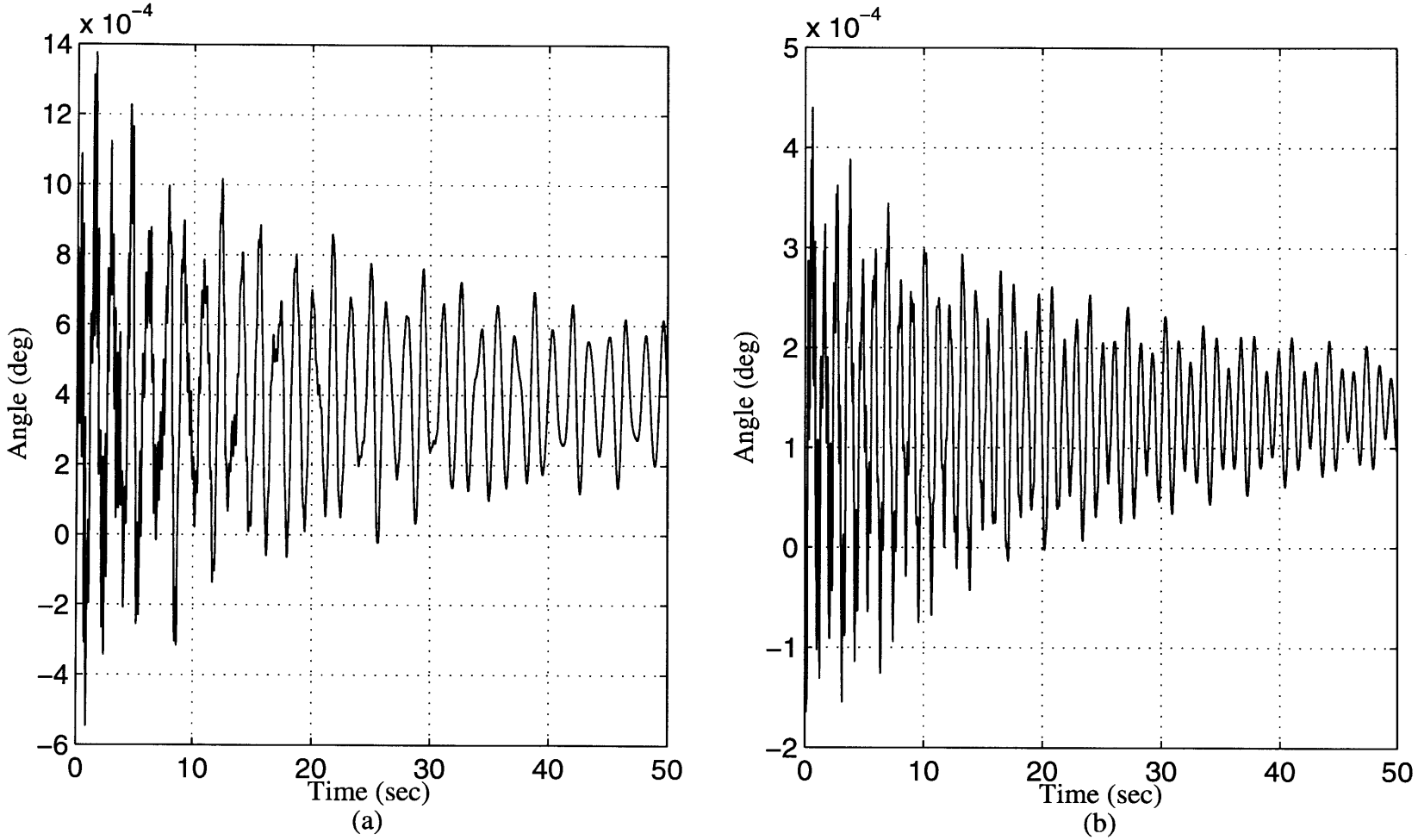

Figure 4-3: World View line-of-sight error due to the impulsive thermal snap. (a) Line-of-sight response about X_G. (b) Line-of-sight response about Y_G.

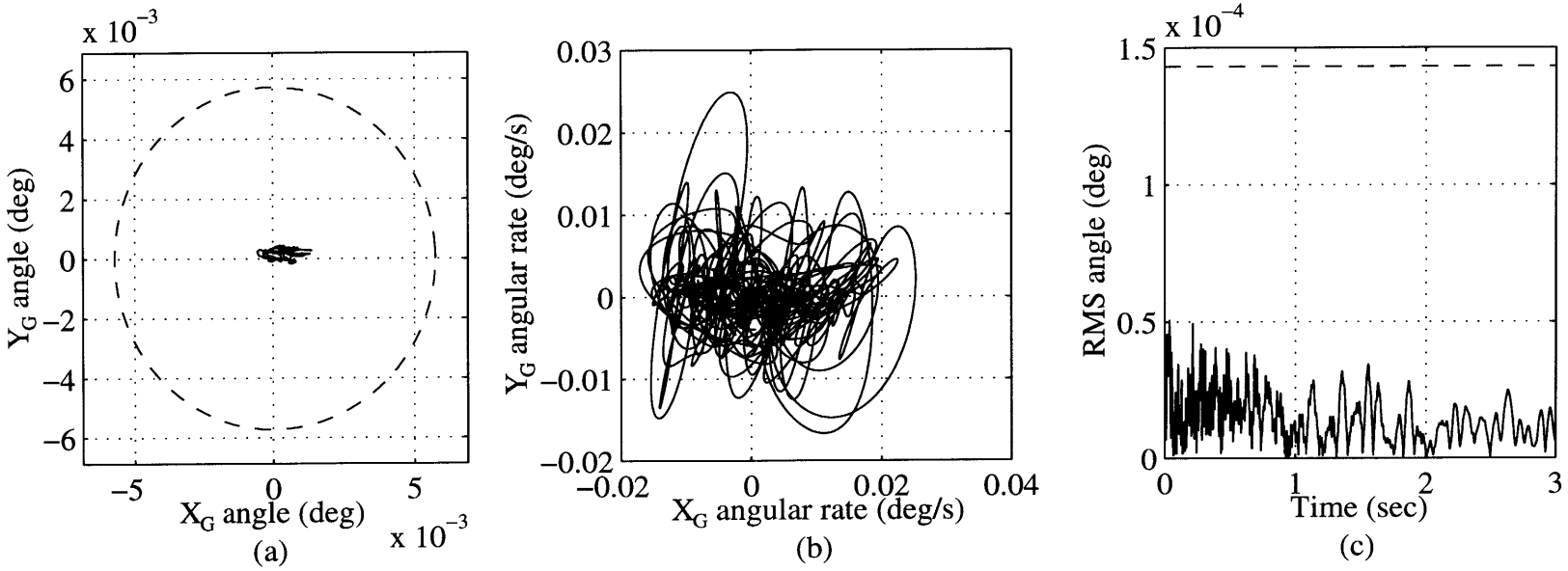

Figure 4-4: Comparison of the performance response to the impulsive thermal snap with World View specifications. (a) Line-of-sight accuracy. (b) Line-of-sight stability. (c) Line-of-sight jitter.

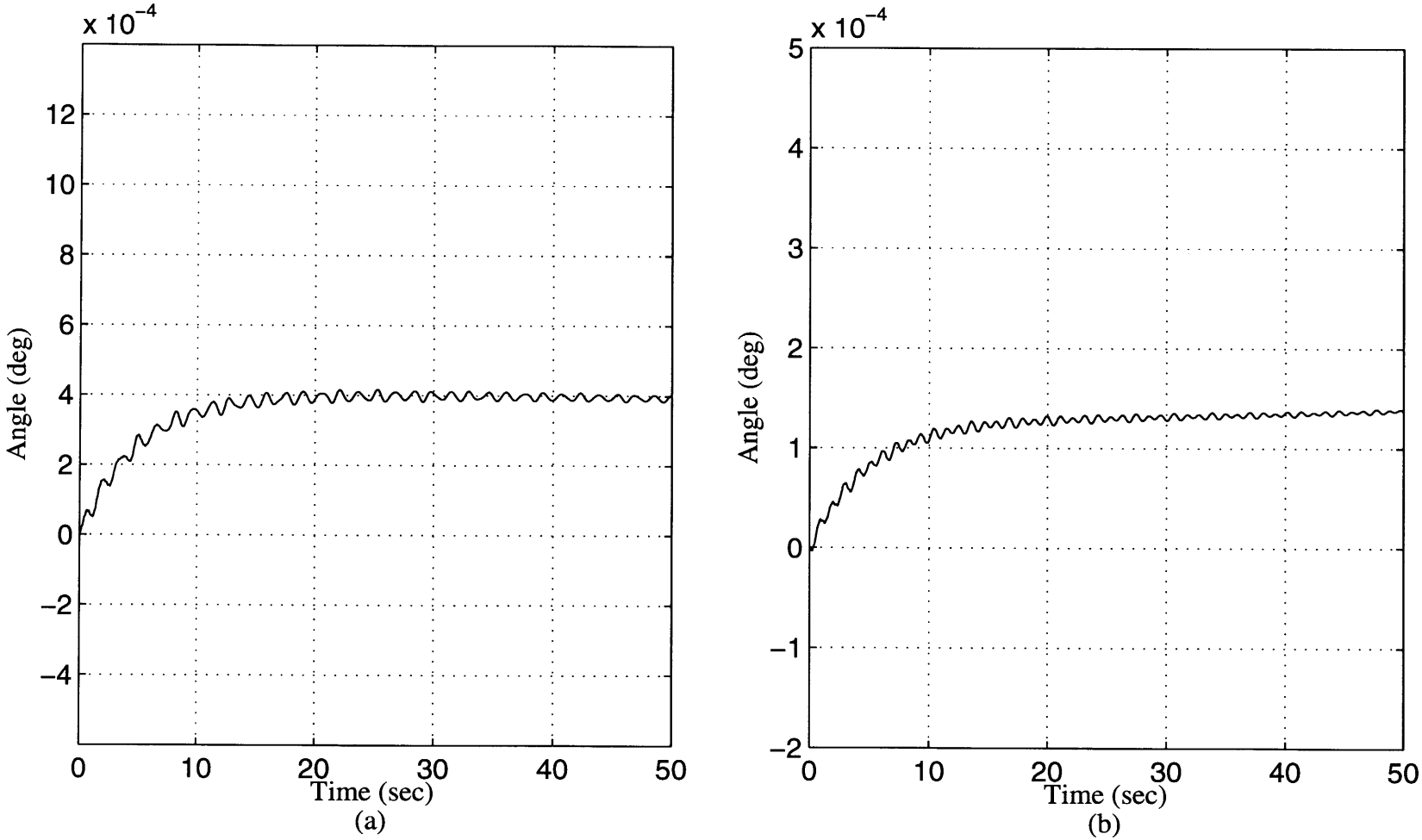

Figure 4-5: World View line-of-sight error due to the gradual thermal snap. (a) Line-of-sight response about X_G.. (b) Line-of-sight response about Y_G.

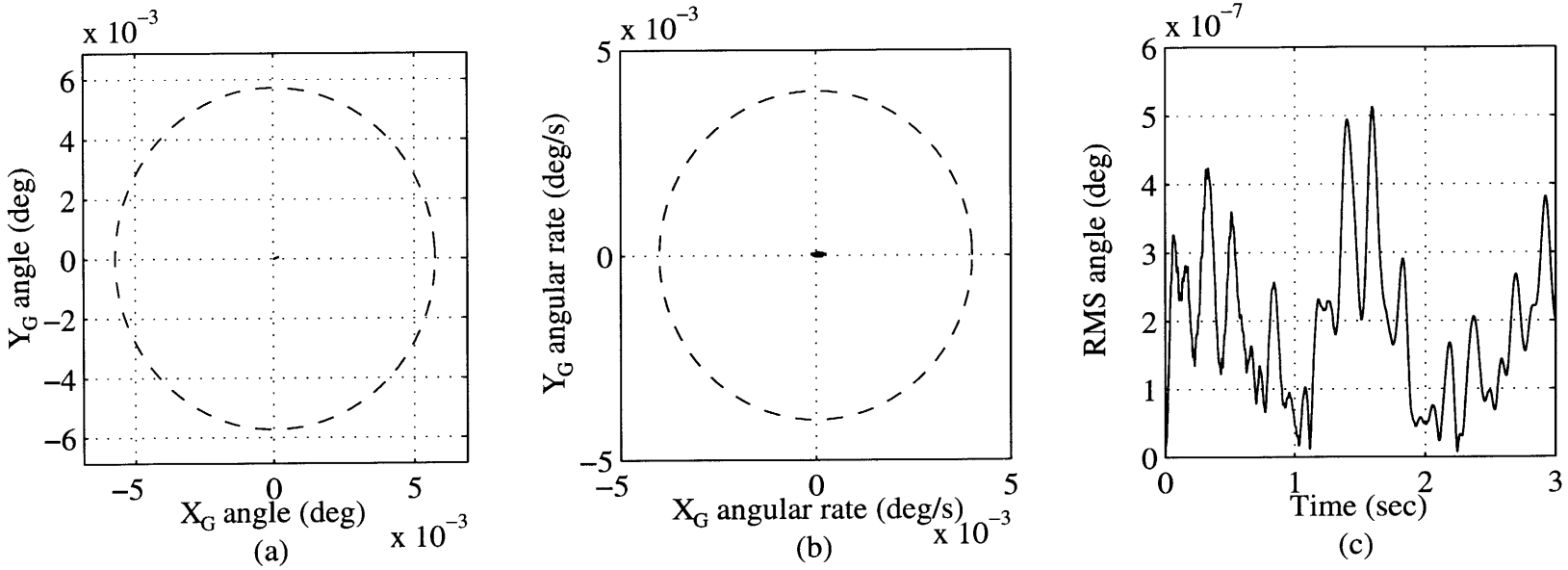

Figure 4-6: Comparison of the performance response to the gradual thermal snap with World View specifications. (a) Line-of-sight accuracy. (b) Line-of-sight stability. (c) Line-of-sight jitter.

Chapter 5

Performance Improvements

The goal in most physical systems with inputs, outputs, disturbances and performances is to obtain the best possible robust performance in the face of disturbances. Having characterized and demonstrated the disturbance effects of World View and thermal snap in previous chapters, the current chapter investigates and compares some open loop and closed loop compensation methods that further improve the pointing performance of the spacecraft.

5.1 Open Loop Compensation Methods

Open loop compensation is often the simplest compensation method to implement. In open loop compensation there is no feedback, eliminating the need for sensor hardware. The lack of a feedback loop also eliminates the possibility of closed loop instability. In flexible structures, open loop compensation is useful in preventing vibration, rather than reacting to it once it has already started. Unfortunately, its advantages simultaneously cause its disadvantages: unwanted static offsets are usually difficult or impossible to eliminate without feedback and existing system vibration cannot be eliminated since it cannot be sensed. Nevertheless, input shaping and feedforward control are useful tools in reducing vibration of flexible systems, demonstrated in the following two sections.

5.1.1 Input Shaping

The concept of input shaping is to use frequency information about a flexible system to modify prescribed inputs, so that they greatly reduce residual vibration. At the simplest level, input shaping involves modifying the prescribed input by convolving it with two impulses, spaced apart by one half of the period of vibration. Early attempts at input shaping had a number of drawbacks, mainly lack of robustness to frequency uncertainty, complexity and computational difficulties. A series of papers [12, 27, 32] describes the use of input shaping to reduce vibration at both single and multiple modes. They offer two computational methods of implementation, a frequency domain, zero pole-placement and a time domain method. Both methods have been coded in MATLAB and simply require the target frequencies of vibration to eliminate, along with the corresponding damping and degree of robustness desired for each frequency.

Of the two disturbances being considered, the World View relative acceleration input is known well in advance, but the thermal snap disturbance is quite random. Therefore, input shaping can only be used to eliminate vibration caused by World View slews. Applying this method is very simple since the NASTRAN eigenvalue solution supplies the natural frequencies of the structure. In order to form the discrete angular acceleration input as explained in Section 3.2.2, use of the continuous angular position of Figure 3-1 as the unshaped input is appropriate. This is because differentiation is a linear operator and acceleration is just the second derivative of position. Once this continuous input is shaped, the discrete angular acceleration input can then be formed as explained in Section 3.2.2.

First attempts to use input shaping will be to reduce the low frequency vibration present in both Figure 3-3 and Figure 3-4, which is largely a result of two solar array modes superimposed, one at 0.64 Hz and the other at 0.94 Hz. Figure 5-1 shows the continuous first-order robustness shaped input compared to the unshaped one together with the corresponding spacecraft responses, demonstrating the elimination of low frequency vibration. Notice, though, that the high frequency vibration is

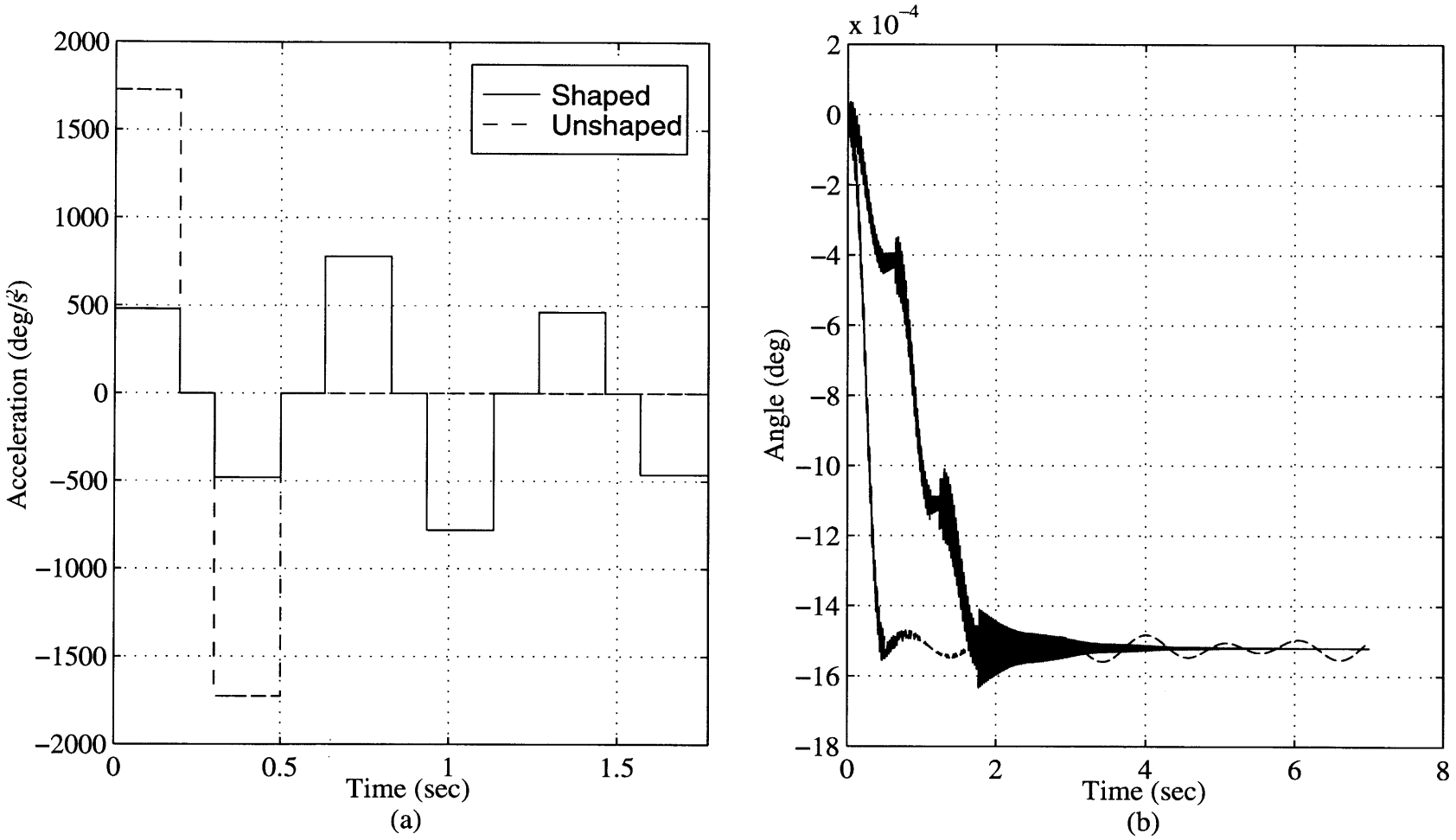

Figure 5-1: Effect of first-order robustness input shaping on low frequency World View line-of-sight vibration about Y_G due to the 1.8 deg Z_{WV} World View mirror slew in 0.5 seconds. (a) Shaped and unshaped relative acceleration inputs. (b) World View line-of-sight error.

further excited by the input shaping, which is sure to make the line-of-sight further exceed the World View stability requirement. Also note there is a substantial time delay of more than 1 second.

In order to demonstrate the robustness of this method in eliminating the low frequency vibration, the two frequencies of vibration that are used as arguments to the input shaping software are offset by 15%. This makes them 0.74 Hz and 1.08 Hz. Figure 5-2 shows the response of the spacecraft to the shaped World View inputs using these offset frequencies, with both first and second-order robustness. Note that the line-of-sight response is shown only after the command. This is so the effects of the input shaping can be more clearly discerned in the plot. Although third-order robustness is more effective than first-order in eliminating low frequency vibration, it is clear that the price paid is a longer command time, an apparent trade off that must be carefully weighed. In situations requiring only single commands, adjustments can be made for this longer command time. However, this is impossible in instances when there are a series of commands, back-to-back. In such cases, the extra time required for the shaping adds up to form a possibly unacceptable time delay. In any case, input shaping can further reduce low frequency vibration of World View's line-of-sight. Although this is not necessary, it means that better pointing accuracy could actually be achieved.

Further use of input shaping is made in attempts to eliminate the high frequency vibration, largely due to the mode at 38.1 Hz, with much smaller contributions from modes at 37.2 Hz and 33.5 Hz. These results failed, as shown in Figure 5-3, despite third-order robustness attempts to account for any error in choice of frequencies. Although there is some effect due to input shaping, the effect is to *increase* vibration, as shown in the figure. Application to various World View mirror slew angles also yielded inconsistent results. Sometimes, specifying greater robustness resulted in even worse results, as is the case in Figure 5-3. The reason given for this is the discretization process performed on the shaped input.

Input shaping works by removing specified frequency components of the signal from the unshaped command input. The absence of these frequency components

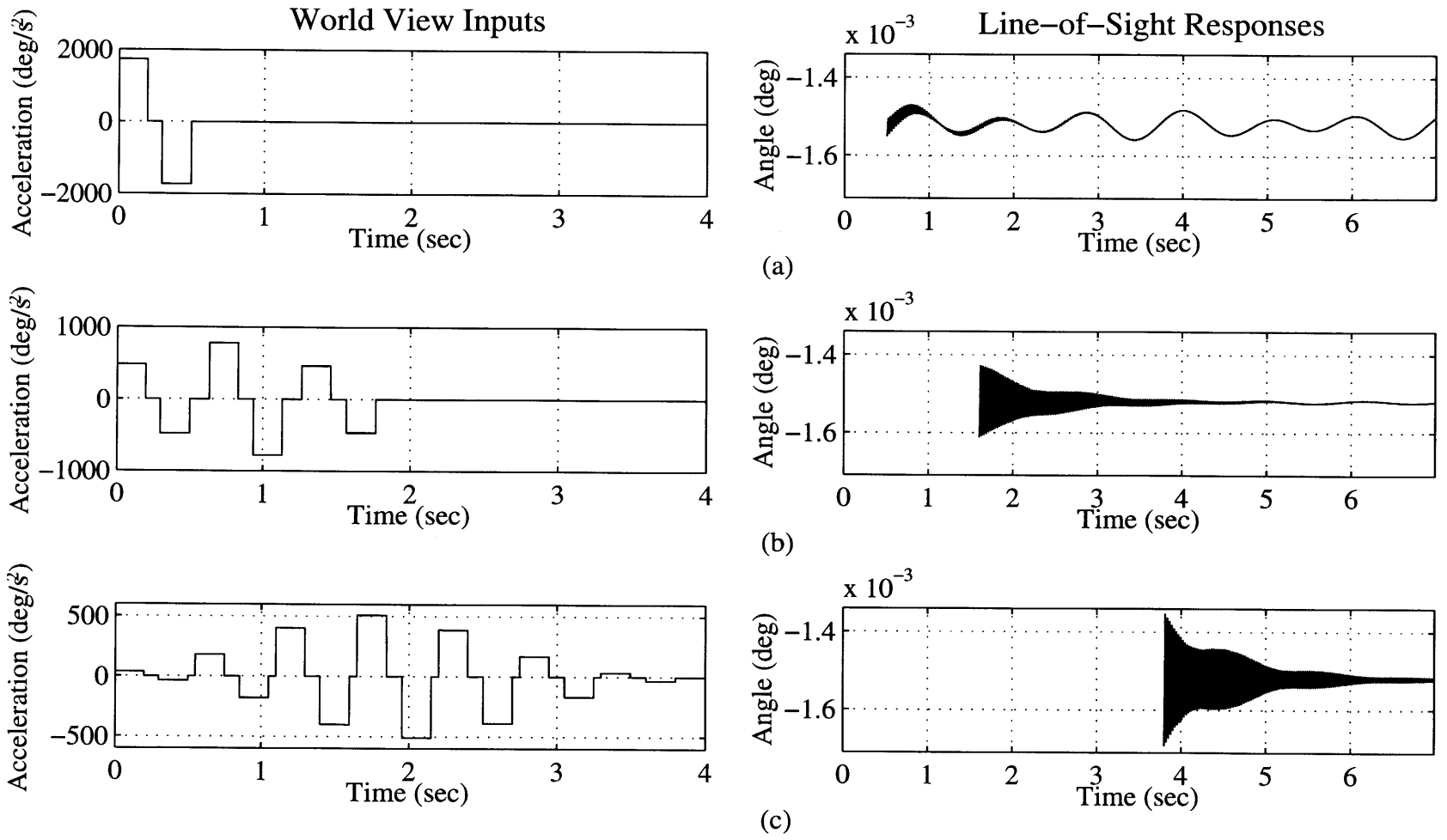

Figure 5-2: Demonstration of input shaping robustness on low frequency World View line-of-sight vibration about Y_G due to the 1.8 deg Z_M mirror slew in 0.5 seconds. (a) No input shaping. (b) First-order robustness input shaping. (c) Third-order robustness input shaping.

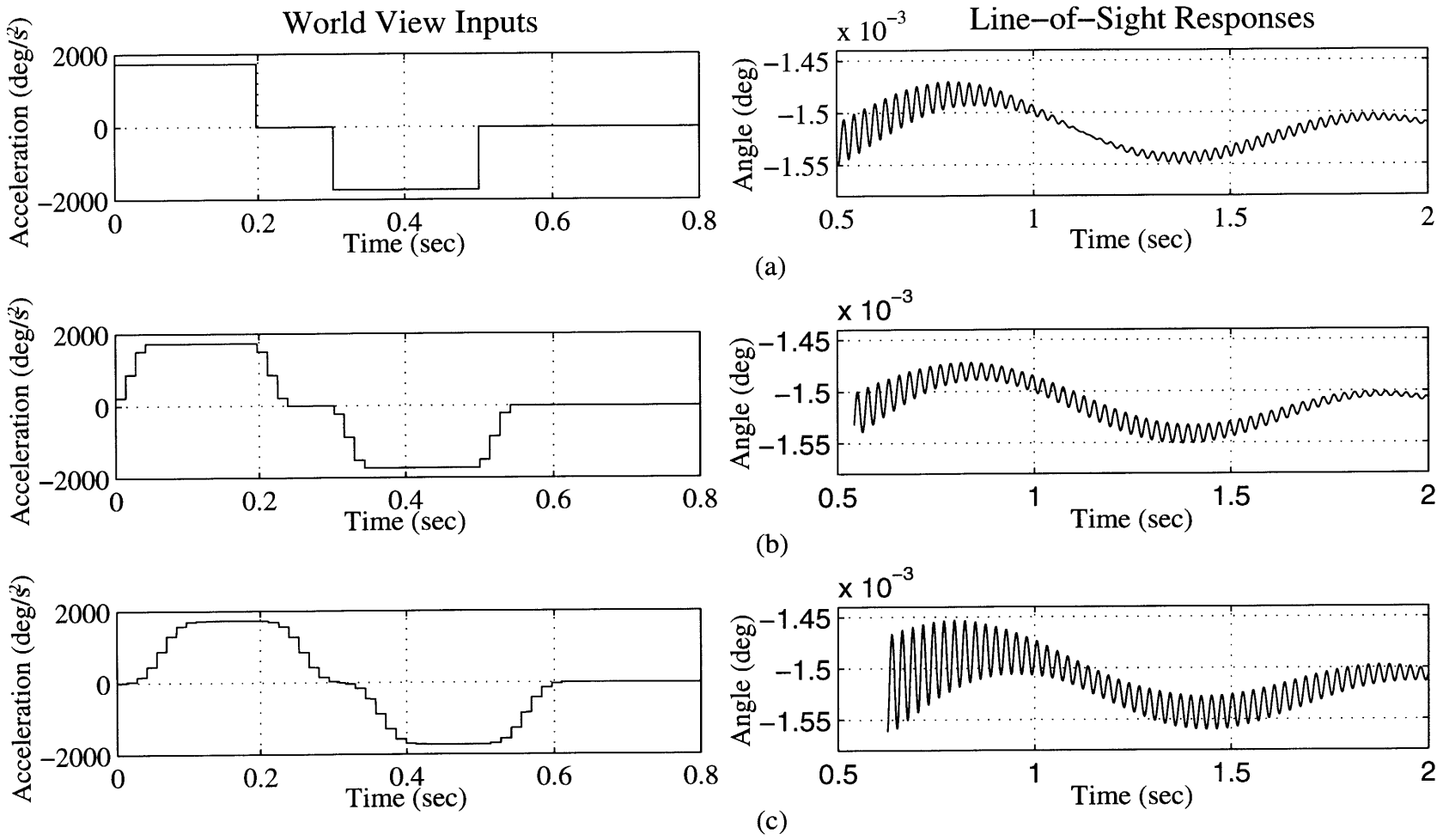

Figure 5-3: Failure of input shaping to eliminate high frequency World View line-of-sight vibration about Y_G due to the 1.8 deg Z_{WV} mirror slew in 0.5 seconds. (a) No input shaping. (b) First-order robustness input shaping. (c) Third-order robustness input shaping.

prevents excitation of the structure at or near those frequencies. However, the discretization of the the World View input introduces impulses which, by nature, excite all modes. Discretization performed *after* the input is shaped re-introduces all frequency components to the final shaped input, causing vibration.

One solution could be to shape the discretized World View input directly. Normally, unshaped, discretized input has uniform impulse magnitudes and the time spacing between impulse pairs is a constant. This results in a constant stepper motor stepsize that occurs over a fixed interval of time. However, shaping the discretized input results in varying impulse magnitudes and time spacing between impulse pairs, which corresponds to varied motor step sizes occurring over irregular times. Such a result is unacceptable because stepper motors are normally driven by only commanding the stepping rate. Driving them with varied stepsizes over irregular times would be very difficult. Thus, shaping the discretized input directly is not possible.

5.1.2 Feedforward Control

The method of feedforward control depends on explicit knowledge of both the plant itself and the disturbance that is to affect it. Since this disturbance must be known exactly, it is usually an input or derivation of one that is utilized in feedforward control. This information, together with an appropriate compensator, forms an additional input in the form of an open loop controller that cancels out unwanted effects of the disturbance on the plant before they cause vibration.

The World View instrument on the Clark satellite serves as the input that disturbs the spacecraft in an attempt to point the mirror. As the World View instrument slews the mirror, it applies a torque on the rest of the spacecraft at the tip of the World View support, causing subsequent low frequency vibration due to the solar array appendage modes. The vibration occurs because the applied torque rotates the spacecraft slightly in inertial space. The World View input can be fed forward to appropriately spin the reaction wheels on the spacecraft bus so that the World View torque is canceled by the reaction wheel torque. The net effect is that the spacecraft

bus is prevented from motion as the World View mirror is slewed, thus not exciting the solar array appendage modes.

Given $\ddot{\mathbf{d}}$, the relative angular acceleration between the World View mirror and the rest of the spacecraft and I_{WV} and $I_{S/C}$, the rotational inertias of the mirror and the rest of the spacecraft, equations governing rigid body rotation can be written as:

$$\begin{aligned} \tau_{applied} &= I_{WV}\alpha_{WV} \\ -\tau_{applied} &= I_{S/C}\alpha_{S/C} \end{aligned} \tag{5.1}$$

where the α's are inertial, $\tau_{applied}$ is the torque applied to the spacecraft, which must be canceled, and $\ddot{\mathbf{d}} = \alpha_{WV} - \alpha_{S/C}$. Subtracting the two equations from each other and solving for $\tau_{applied}$ results in

$$\tau_{applied} = \left(\frac{I_{WV}I_{S/C}}{I_{WV} + I_{S/C}}\right)\alpha = K_{ff}\ddot{\mathbf{d}} \tag{5.2}$$

where K_{ff} = the feedforward gain. Therefore, as long as the inertias of the spacecraft and the mirror are known, the reaction wheel can be commanded to supply the correct counteracting torque, $-\tau_{applied}$.

The smooth version of the World View input shown in Figure 3-1 is used as the signal to feed forward since the the goal is to eliminate the low frequency solar array modes. This is multiplied by the gain K_{ff} and used as the torque input couple to the reaction wheel and spacecraft at the reaction wheel location, simultaneously applied with the World View mirror slew input. The World View mirror is being slewed about Z_{M}, which is equivalent to Y_{O}. Therefore, the reaction wheel employed is also about Y_{O}.

Figure 5-4 shows the resulting response of the system with the application of this feedforward control technique. Also shown is the response of the system when K_{ff} is incorrect by 15%. The low frequency vibration due to the solar arrays is entirely eliminated. Thus, the line-of-sight pointing accuracy will be greatly improved, although this is not required. The improvement is not only because vibration has been prevented, but also because the spacecraft has not been slewed by the reaction

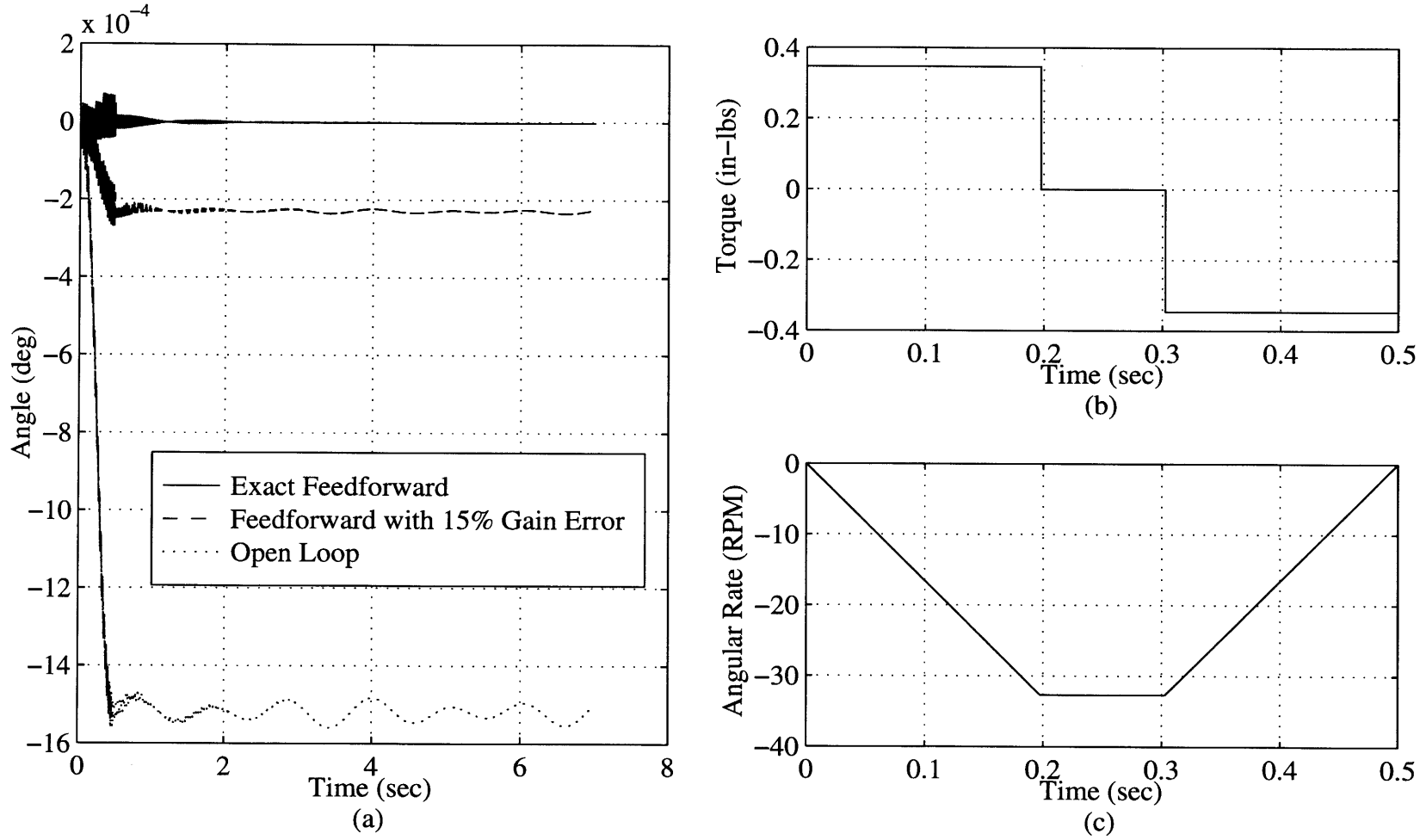

Figure 5-4: Effect of feedforward control on the Clark spacecraft's response to a 1.8 deg Z_M mirror slew in 0.5 seconds. (a) World View line-of-sight response about Y_G with and without feedforward control. (b) Reaction wheel torque required. (c) Reaction wheel velocity required.

torque from the mirror motion. Even with an error of 15% in the feedforward gain, the resulting behavior is still greatly improved, demonstrating that feedforward control can be relatively robust with respect to uncertainty in the plant.

Unfortunately, the feedforward method used here does not eliminate high frequency vibration, as shown in Figure 5-5. Inspection of the modeshapes for various

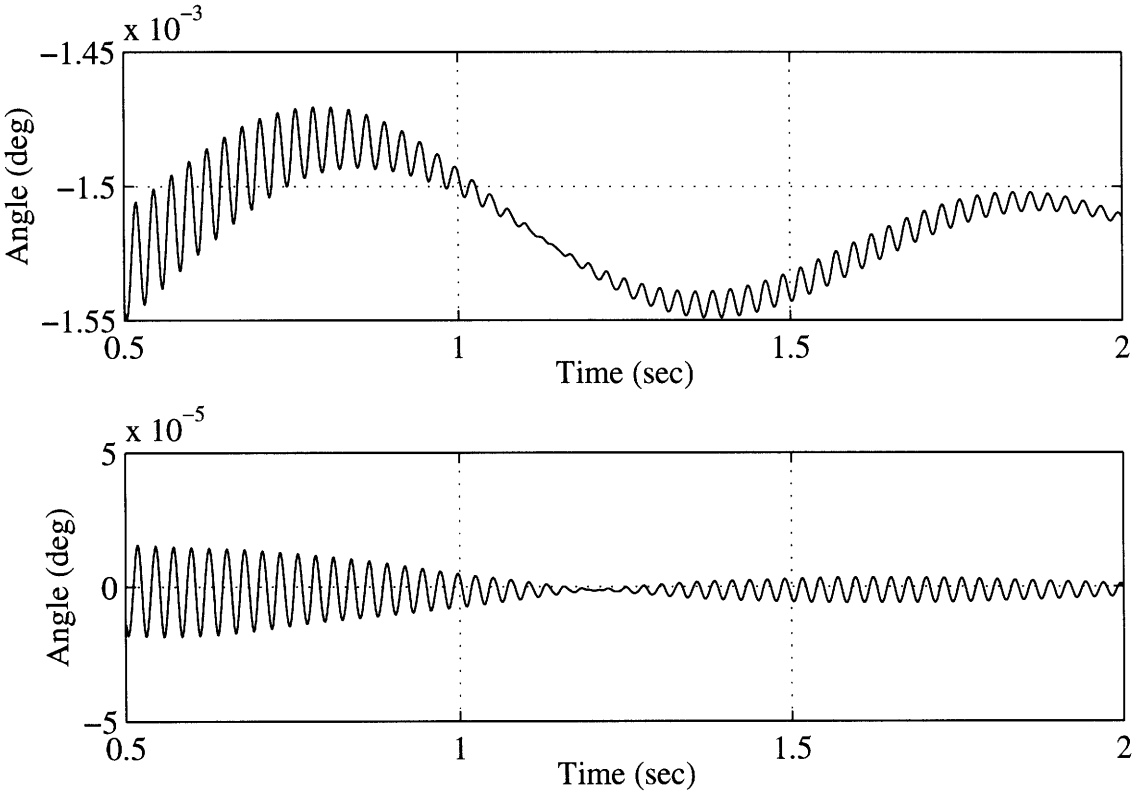

Figure 5-5: A more detailed look at Figure 5-4a: Feedforward's failure to eliminate high frequency vibration caused by the World View mirror motion. (Top) Line-of-sight Y_G response without feedforward control. (Bottom) Line-of-sight Y_G response with feedforward control.

frequencies has shown that these high frequency vibrations come from the World View support itself, which is the structure forming the load path between the World View mirror and the reaction wheels. Therefore, holding the satellite bus stationary will not prevent the support from vibrating. Without any information about the vibrating World View support, feedforward control is useless against it.

5.2 Closed Loop Compensation Methods

In areas where open loop compensation fails, closed loop compensation has the advantage of being able to use feedback. The disadvantage, though, is having to worry about stability, and therefore being faced with the control-structure interaction problem. Limitations on the achievable performance are usually imposed by the flexibility of a structure, yet some performance improvement is often possible.

A common form of closed loop control is rate feedback, which usually adds damping to flexible systems. Additional damping will reduce the length of time there is significant vibration, but increased damping does not prevent vibration from starting in the first place. The amount of damping added and the modes that become more damped depend on the allowable closed loop bandwidth of the system and the magnitude of the gain. These depend on the stability limits imposed by the control-structure-interaction problem.

5.2.1 Feedback from Rate Gyro to Reaction Wheel

Rate feedback from the rate gyro on the Clark satellite to the reaction wheels is one method of introducing damping into the system. Figure 5-6 shows a simplified topological equivalence of such a feedback loop, demonstrating that physically, this rate feedback is equivalent to a damper being attached to the spacecraft from inertial space, resisting any motion of the spacecraft.

For low frequencies, this sensor-actuator pair can be considered as structurally collocated, making rate feedback always stable. At higher frequencies, local bus modes with structural deformation between the gyro and the reaction wheel cause higher gains to drive the loop unstable. This is evident by looking at a Bode plot of the loop transfer function from reaction wheel torque input to gyro rate output, shown in Figure 5-7. This Bode plot shows that as a larger feedback gain is used, modes between 500-750 Hz will be the first to cross the 0 dB line, causing the closed loop system to go unstable since the phase is already past 180 deg. To compensate for this, a second-order lag compensator is used to attenuate the gyro output at high

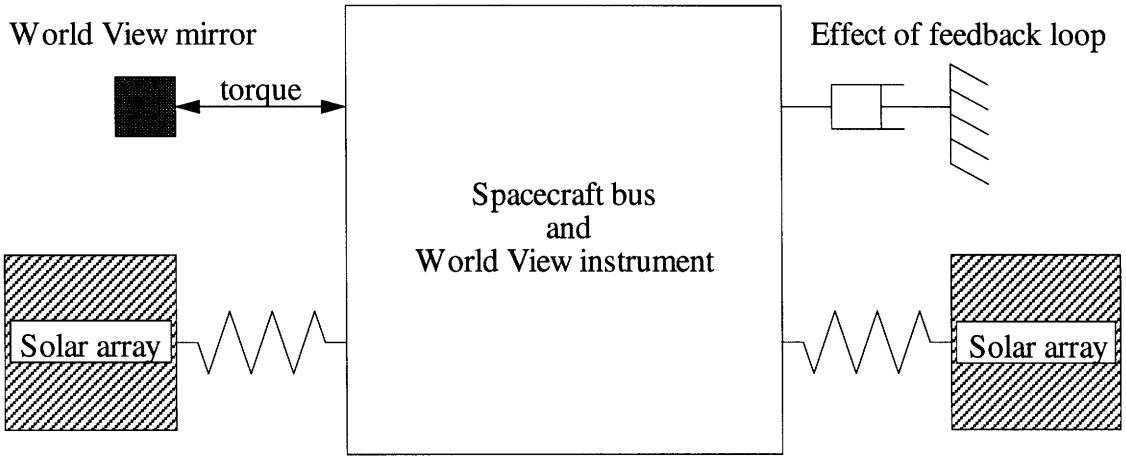

Figure 5-6: Topological equivalence of rate gyro to reaction wheel feedback.

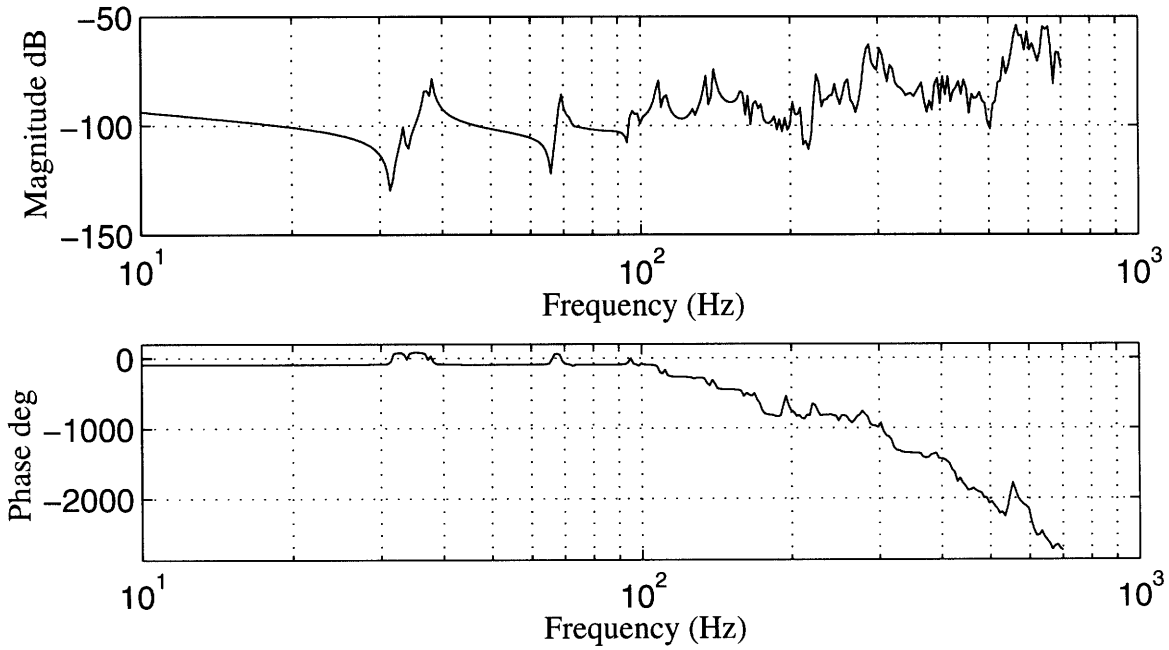

Figure 5-7: Bode plot of loop transfer function from reaction wheel torque input about Y_O to rate gyro output about Y_O.

frequencies. The compensator chosen is

$$K(s) = k\frac{(s+10000)^2}{(10s+10000)^2}, \tag{5.3}$$

and its Bode plot is shown in Figure 5-8.

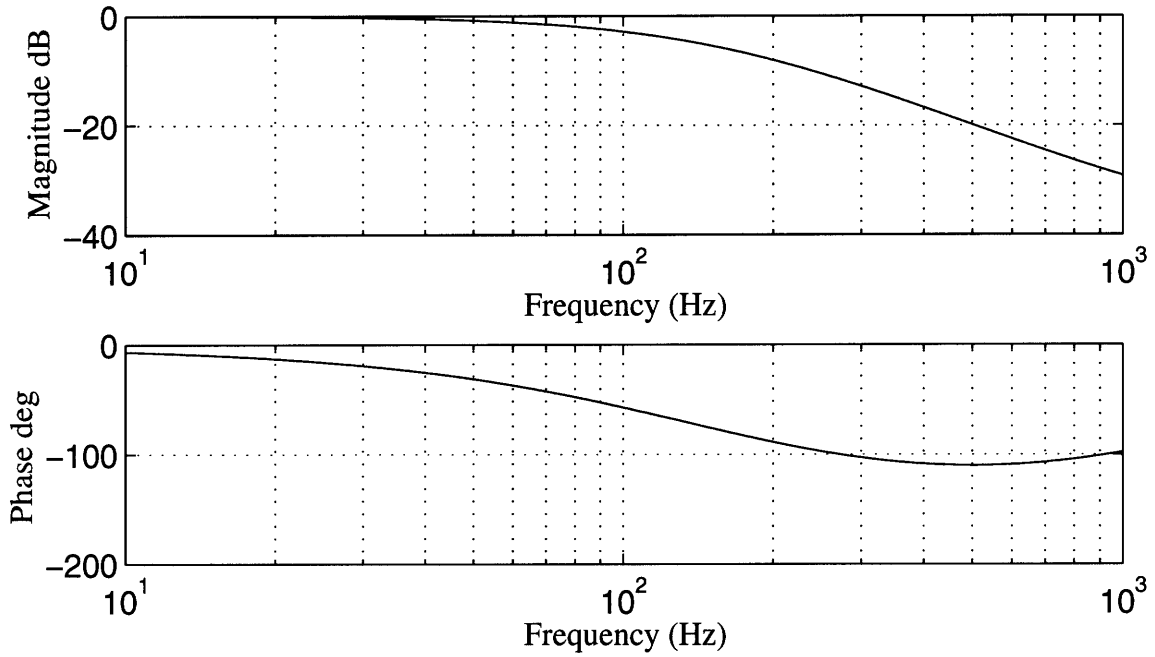

Figure 5-8: Bode plot of compensator used for rate gyro to reaction wheel feedback.

The higher the compensator gain k, the greater the improvement that might be expected in the performance. However, improvement by increasing the gain alone is limited due to stability consideration. Using the compensator in Equation (5.3) with the compensator gain, $k = 4000\frac{\text{in-lbs}}{\text{deg/s}}$ results in a revised Bode plot shown in Figure 5-9. This plot shows that the closed loop system will be gain stabilized, though only by about a 6 dB gain margin. The system response to typical World View mirror slew using this closed loop controller is shown in Figure 5-10. In simulating the response, the bandwidth of the model had been limited to 100 Hz, since it is believed that the spectral content of the *real* stepper motor disturbance has much less energy at higher frequencies. If the very high frequency modes are included, the impulse pairs

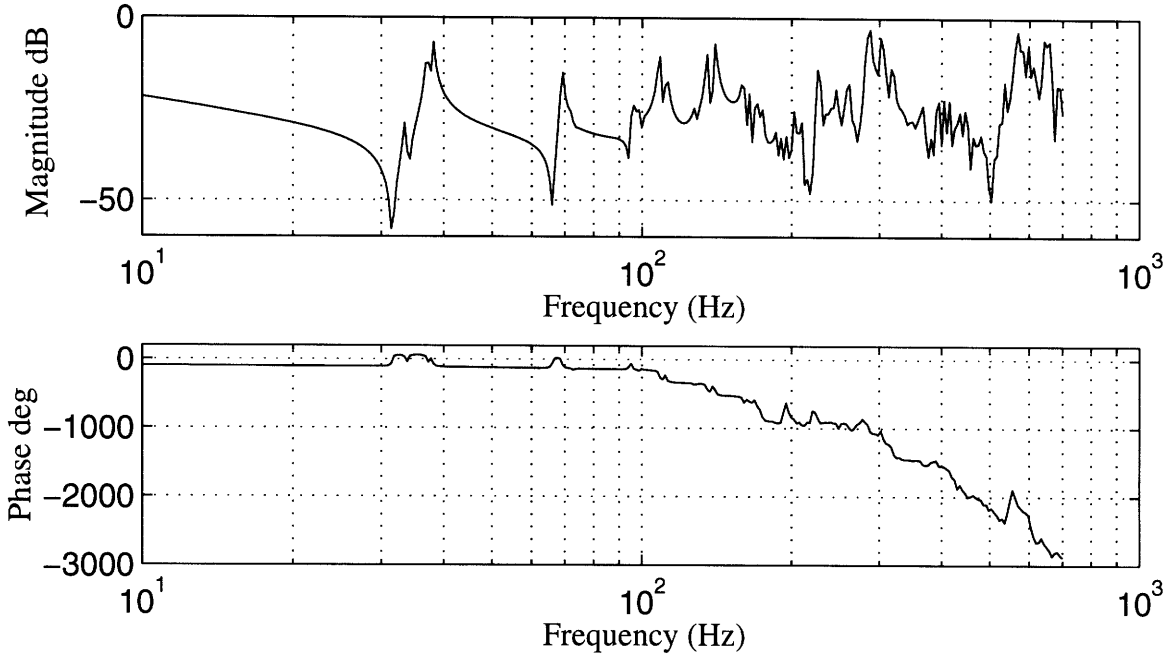

Figure 5-9: Bode plot of loop transfer function from reaction wheel torque input about Y_O to rate gyro output about Y_O, with compensator in the loop.

that model the discrete motor step will cause excessive, and probably unrealistic, excitation of many of the very high frequency modes. A surprising effect of this feedback is that it returns the spacecraft to its original attitude, although there is no position feedback.

As Figure 5-10 shows, there is slight attenuation of low frequency vibration by about a factor of two. More surprising is the fact that the closed loop response does not appear any more damped than the open loop. This can be explained with the aid of Figure 5-6. The vibration of the system involves very small rigid body motion of the satellite bus and relatively large flexible motions of the solar arrays. Therefore, the cyclic transfer of energy from potential to kinetic form occurs mostly in the solar arrays. In order to effectively damp the vibrations, this energy in the solar arrays needs to be removed. Increasing the damping gain, k, removes very little energy since the rate of motion of the massive satellite bus is small compared to the motion of the solar arrays. If $k \to \infty$, then the spacecraft bus would become

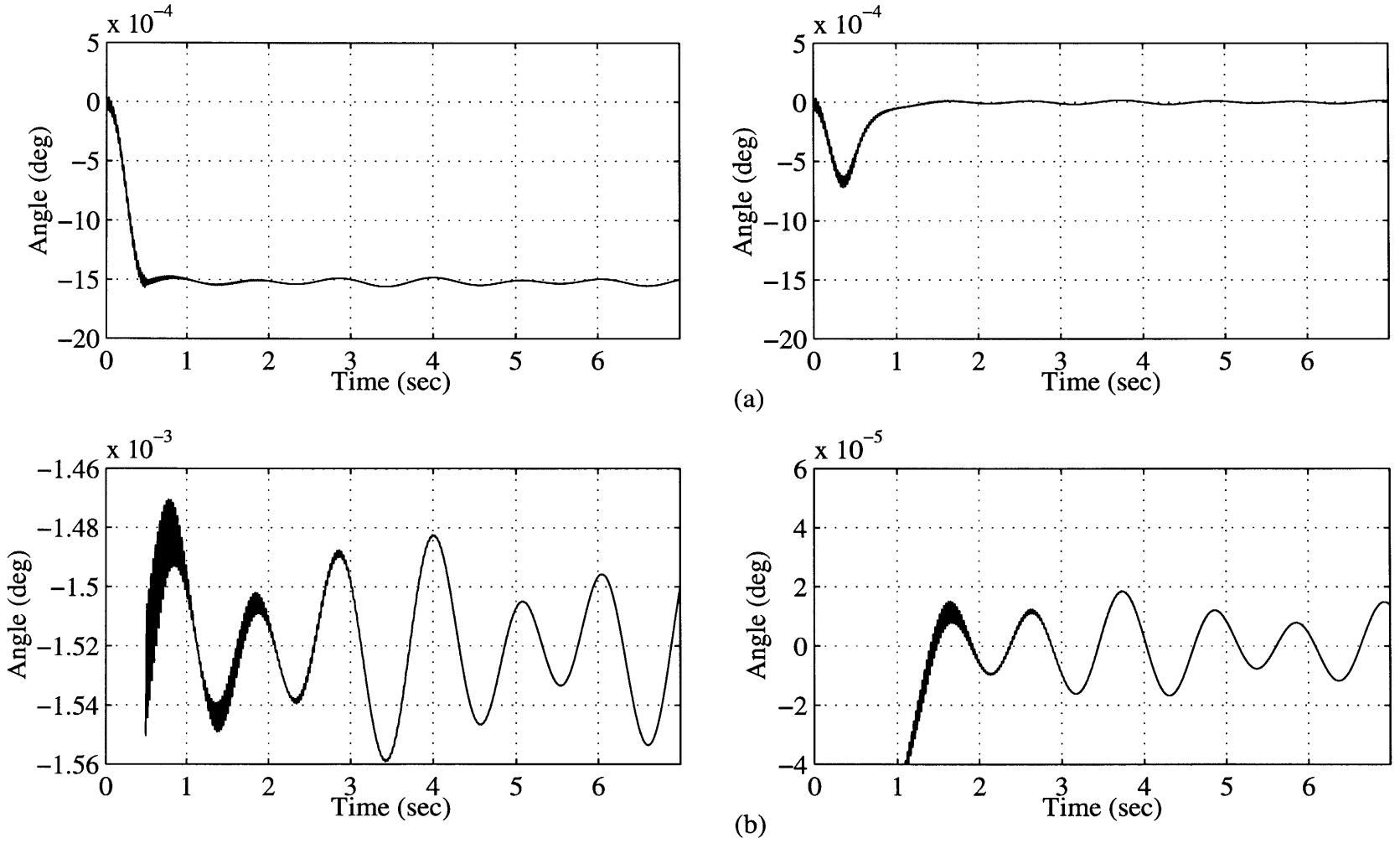

Figure 5-10: Effect of rate gyro to reaction wheel feedback on the World View line-of-sight response about Y_G when excited by a 1.8 deg Z_M World View mirror slew in 0.5 seconds. (a) Full view. (b) Close up view.

locked in space, not vibrating at all, while the solar arrays would continue to vibrate unimpeded. This controller, then, simply serves to create vibration isolation, reducing the amount of bus vibration due to solar array vibration. In order to more effectively reduce vibration, it would be better to actually reduce the vibration in the solar arrays. This method, therefore, is not very practical, especially since the closed loop approaches instability at higher gains of k.

Figure 5-11 shows the response of this closed loop system to the thermal snap disturbance derived in Chapter 4. The conclusion drawn from this figure is the same as that drawn from Figure 5-10, namely, that the little effect of rate feedback in this case is vibration isolation and not an increase in damping.

5.2.2 Actuator/Sensor Pair on World View Support Strut

Use of a piezoceramic actuator at the root of the World View support and a linear accelerometer at the tip of the support is another way to form a closed loop controller that may damp out vibrations. In practice, the accelerometer signal will be integrated to give a velocity signal appropriate for feedback. This topology works directly on reducing the high frequency vibration that is present in the World View support.

The World View support is basically a 3 ft. long, thin shelled, hollow tube with a 5 in. outer diameter, 0.13 in. shell thickness and 5.69 in^4 bending moment of inertia. With such dimensions, it is reasonable to approximate this beam as a Bernoulli-Euler beam. Knowing the cross-sectional dimensions of the tube and the bending moment of inertia, the physical dimensions of a box beam with identical stiffness can be derived. The flat surface of the box beam makes it easier, in practice, to physically apply piezoceramic actuators. The result is a square box beam section with a 4.3 in. width and 0.11 in. wall thickness.

The piezoceramic material is mounted near the root of the World View support, on the top and bottom of the support, as shown in Figure 5-12. The actuator spans the 4.3 in. width b_a of the box beam, has a length l_a of 1.0 in. and a thickness t_a of 0.01 in. The length and thickness is typical of piezoceramic actuators and the full beam-span width is chosen to achieve as much authority as possible. In practice,

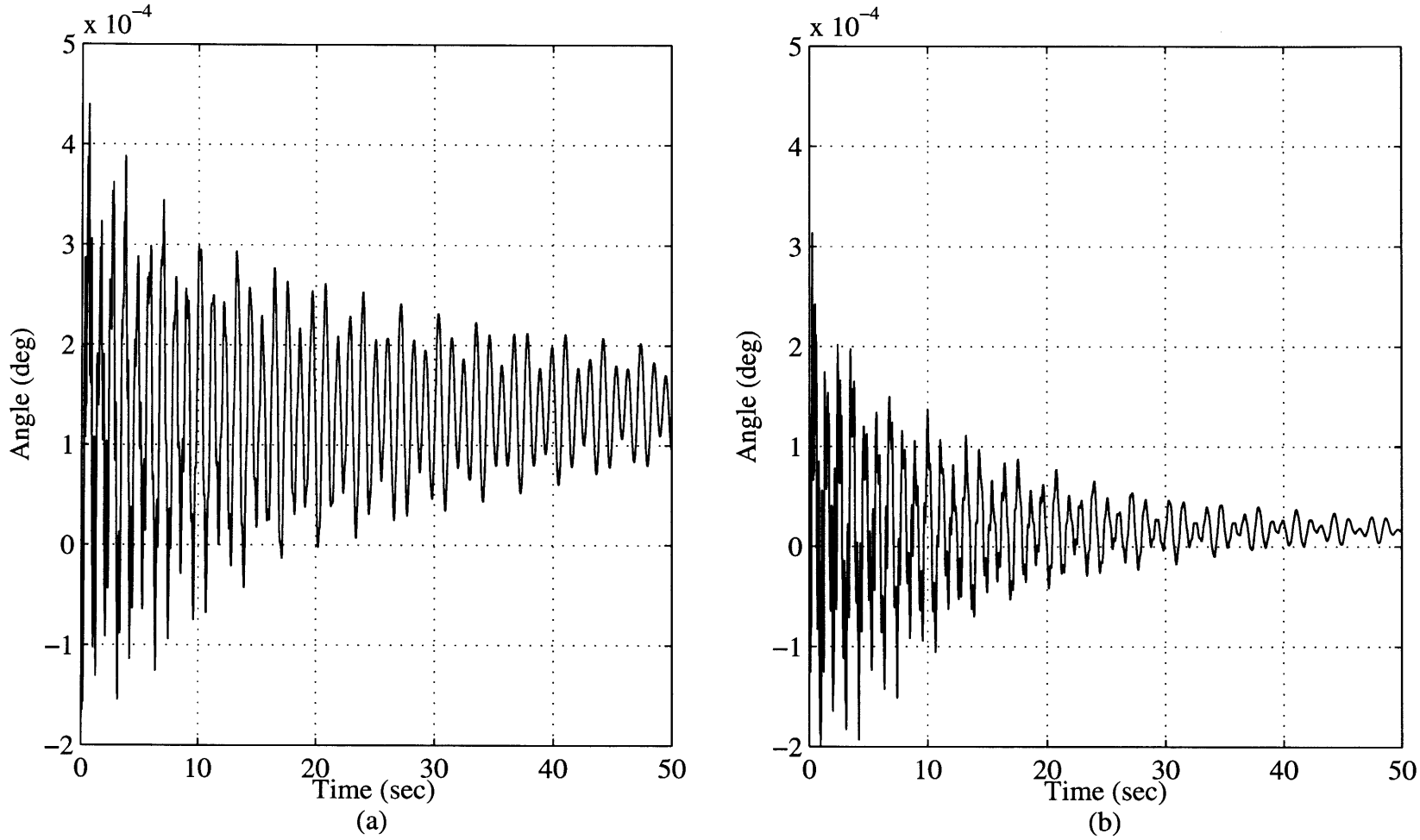

Figure 5-11: World View line-of-sight Y_G response to thermal snap using rate gyro to reaction wheel feedback loop. (a) Open loop. (b) Closed loop.

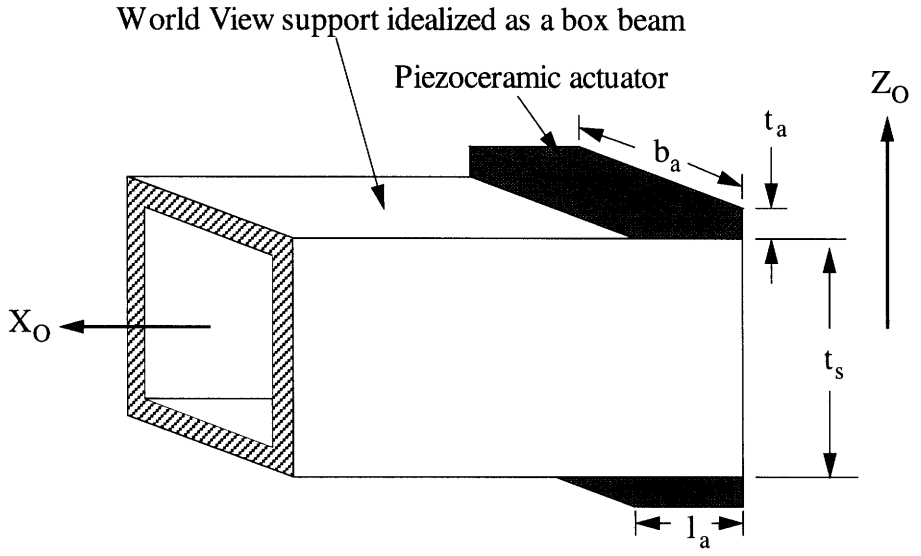

Figure 5-12: Piezoceramic actuators mounted at the root of the World View support to apply bending moment.

such a large actuator width is often achieved by placing several strips side-by-side. When actuated, one piezoceramic patch extends and the other contracts, causing a bending moment on the structure. To simulate this using the finite element model, an additional input needs to be formed to combine with the rest of the control inputs $\boldsymbol{u}$, already defined in Section 2.3. The bending moment is modeled by applying an equal and opposite moment couple at two finite element nodes that form the end points of a 1.0 in. long structural section near the root of the World View support.

According to Anderson and Crawley [2], the magnitude of the moment couple is

$$M_\Lambda = \int E(z_o)\Lambda(z_o)b(z_o)z_o dz_o, \tag{5.4}$$

where E is Young's modulus, Λ is the piezoceramic free actuation strain, b is the width and z_o is the location at which these properties are defined. Note that z_o is measured in the Z_O direction. Referring to Figure 5-12, b and E represent values of the structure over $|z_o| < \frac{t_s}{2}$ and represent values of the actuator over $\frac{t_s}{2} < |z_o| < \frac{t_s}{2} + t_a$, where t is thickness and the subscript a and s represent the actuator and structure,

respectively. The nest step is to integrate over $\frac{t_s}{2} < |z_o| < \frac{t_s}{2} + t_a$, since $\Lambda = 0$ over $|z_o| < \frac{t_s}{2}$. Noting that $\Lambda = d_{31}E_3 = d_{31}\frac{V}{t_a}$, where d_{31} relates the applied field E_3 to the free strain Λ, and the applied field E_3 is expressed as the voltage V applied across the actuator thickness, the result of the integration is

$$M_\Lambda = 2E_a A_a \left(\frac{t_s}{2} + \frac{t_a}{2}\right) d_{31} \left(\frac{V}{t_a}\right). \tag{5.5}$$

where A_a is the actuator's cross-sectional area and E_a is the actuator's Young's modulus. The values of the piezoceramic material constants, d_{31} and E_a, are those of PZT-5A [21]. Thus, this new control input in the simulation will now be in terms of voltage V.

Similarly, a new measurement must be created for the World View support tip velocity and combined with the output measurement vector $\boldsymbol{y}$. The tip velocity can, in practice, be measured by integrating the World View tip acceleration using an accelerometer. However, to model this in the simulation, the rate output of a node at the tip is directly available by virtue of the state-space form of the differential equation, Equation (2.5).

There are two fundamental issues that must be considered when attempting to create an effective closed loop system of this kind. First, the acceleration at the tip of the World View support, shown in Figure 5-13, must be large enough to be sensed by the accelerometer. The magnitudes shown are sufficient to be observable

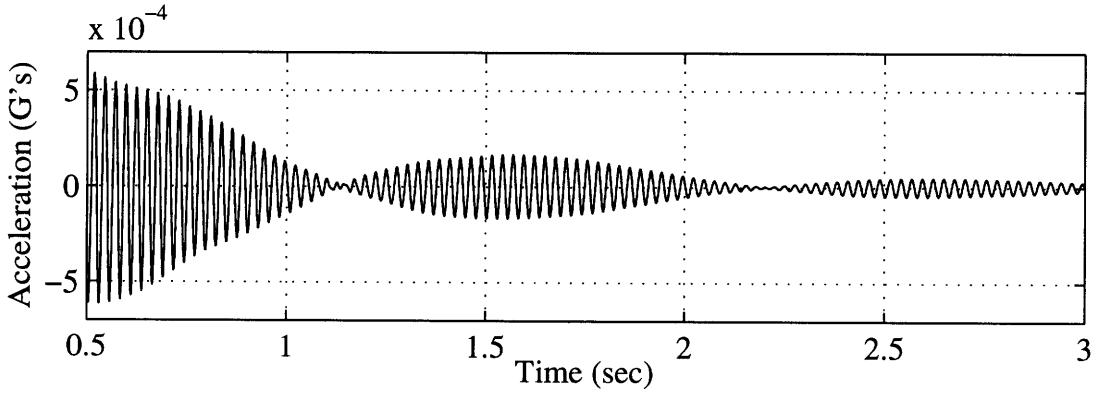

Figure 5-13: World View support tip acceleration in Z_O direction caused by 1.8 deg Z_M World View mirror slew in 0.5 seconds.

relative to noise with current state-of-the-art accelerometers. Second, piezoceramic actuators have limits to their authority defined by the *coercive field* of the particular piezoceramic material used [7]. This is the electric field at which the piezoceramic material depoles and thus no longer functions as intended. Care should be taken that the feedback gain does not cause excessively high applied voltages that near the coercive field.

Stability is another issue that is of concern, since the actuator-sensor pair are non-collocated. The Bode plot of the loop transfer function from voltage input to tip velocity output, shown in Figure 5-14, helps investigate this issue. This Bode plot indicates that the closed loop system will always be gain stabilized, and only the authority of the actuator may be of concern. This is surprising, because the actuator and sensor are non-collocated. However, the World View mirror and gimbals comprise a large mass located at the tip of a relatively lightweight support. The modal participation of this relatively large tip mass is chiefly responsible for the low fundamental frequency of this support. Above the fundamental frequency, the tip mass becomes locked in space and only the relatively light, distributed mass of the support modally participates, making subsequent natural frequencies much higher. Thus, the relatively large tip mass is responsible for the large bandwidth between the fundamental and higher frequencies. The second bending mode of the World View support does not occur until about 1000 Hz. This explains the lack of a second peak in Figure 5-14.

Closing the loop and choosing a feedback gain of $k = 1000 \frac{\text{volts}}{\text{in/sec}}$, the system then behaves as shown in Figure 5-15 when excited by a World View mirror slew. Clearly, this closed loop system does an excellent job of damping out the 38 Hz vibration very quickly. In addition, notice that the voltage applied to the actuator is well below the maximum of about 250 volts allowed for a 0.01 in. thick piezoceramic element [21].

Since this method of compensation effective reduces high frequency vibration, it should improve the stability performance of the World View line-of-sight. Figure 5-16 shows that there is some improvement. Note that the data is not presented as a scatter plot as before, but instead as a function of time. Also note that the responses

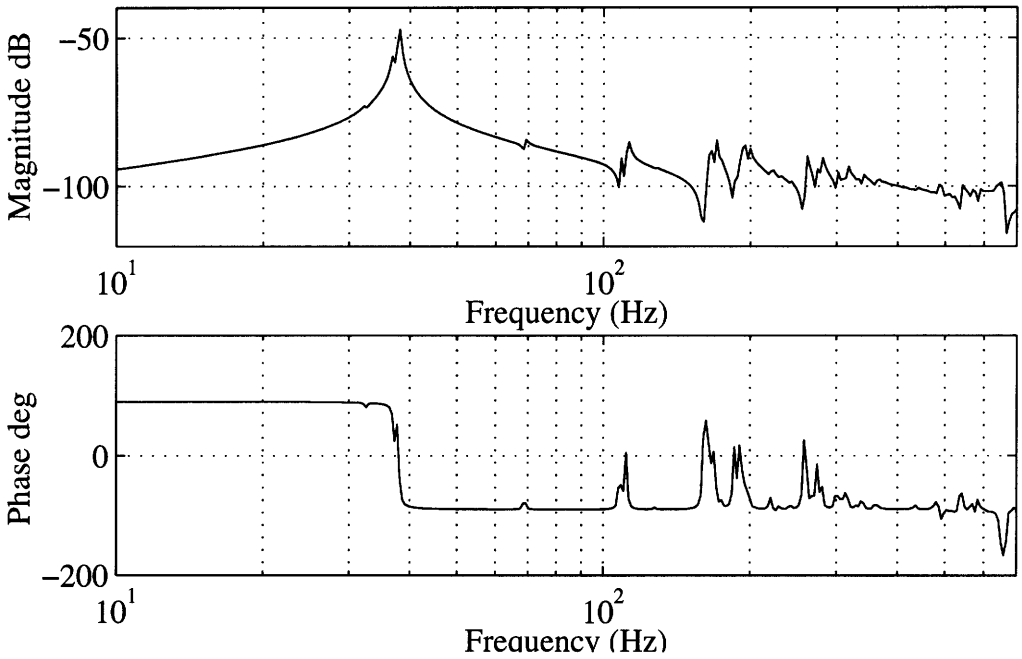

Figure 5-14: Bode plot of loop transfer function from piezo voltage input to World View support tip Z_O velocity.

are shown only after the World View commands are finished. Although the closed loop system does not bring the line-of-sight stability within the specification for all time, it certainly does reduce the duration of exceedance significantly.

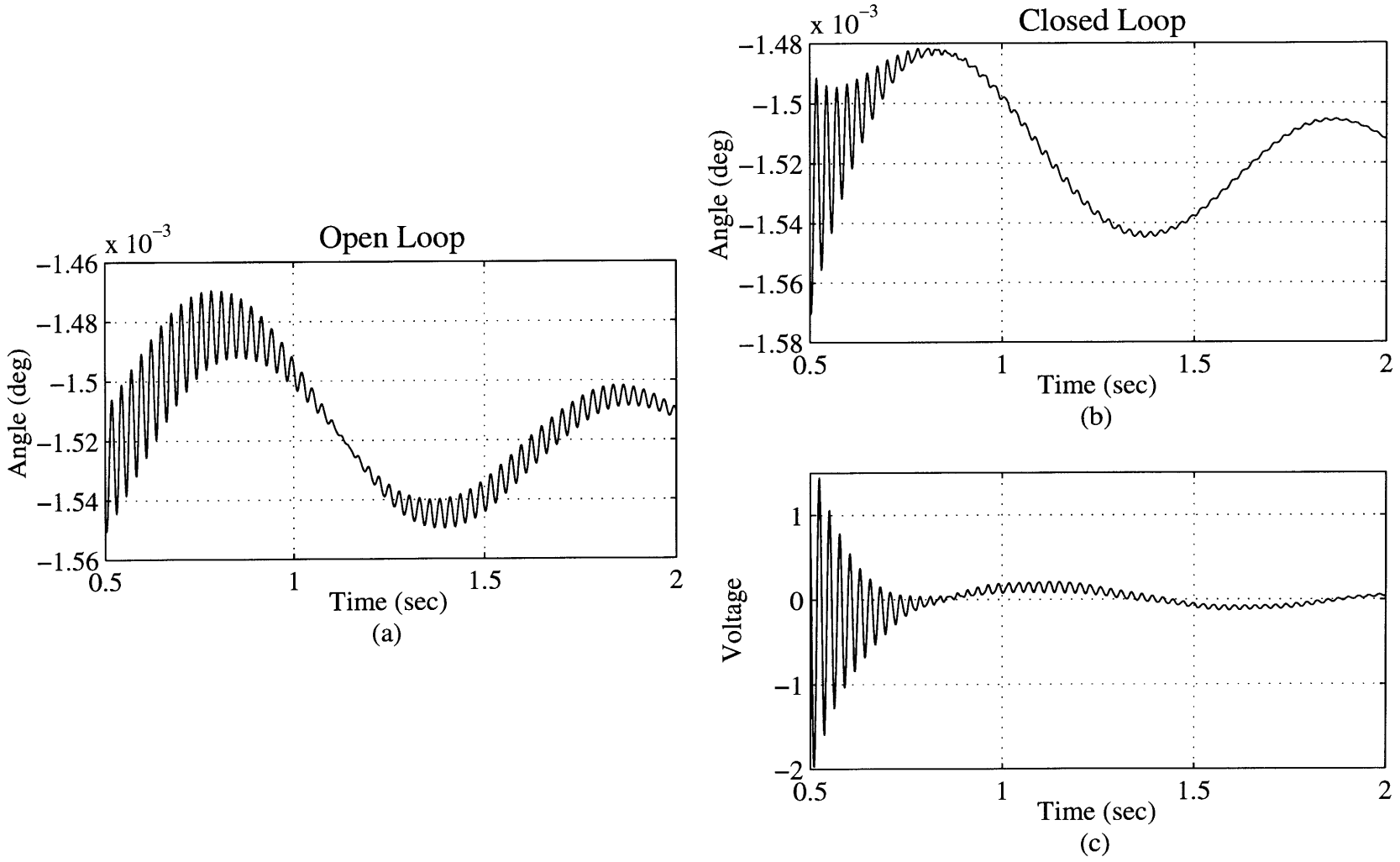

Figure 5-15: Effect of World View tip Z_O velocity to piezoceramic strain actuator feedback on the World View line-of-sight Y_G response when excited by the 0.35 deg Z_M World View mirror slew in 0.5 seconds. (a) Open loop. (b) Closed loop. (c) Voltage applied to piezoceramic actuator.

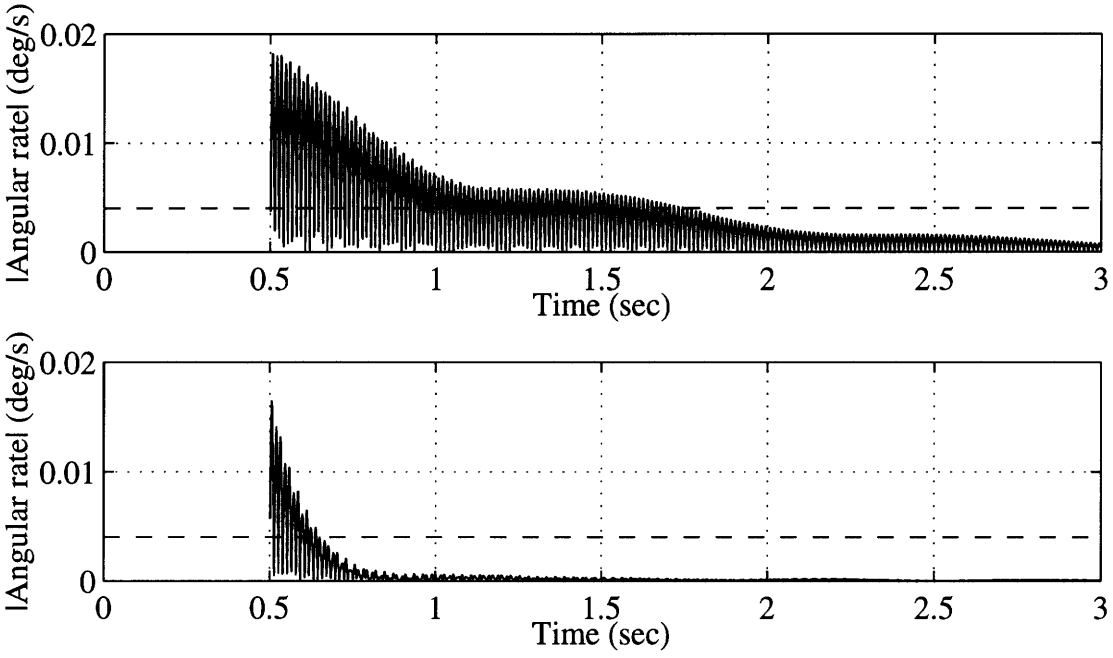

Figure 5-16: Improvement in World View line-of-sight stability using piezoceramic/accelerometer closed loop feedback. Shown are responses to a 0.35 deg Z_M mirrow slew. (a) Open Loop. (b) Closed Loop.

Chapter 6

Conclusion

6.1 Summary

This thesis has investigated the effect of disturbance sources on the pointing performance of the Clark spacecraft, and has utilized open and closed loop compensation methods to attenuate their effects. A NASTRAN finite element model of the spacecraft was modified and used to simulate the spacecraft. Both smooth and discrete models of the stepper motor motion were developed and applied to the spacecraft model, predicting that all the performance specifications will be met, with the exception of the stability specification due to high frequency vibration.

Also, a model of thermal snap was formulated. The application of this thermal snap model to the spacecraft model predicted that all of the performance specifications will be met, except for the stability specification due to high frequency vibration.

Attempts were made to further improve performance and also to possibly meet the stability specification. Two open loop and two closed loop compensation methods were applied to attenuate the World View and thermal snap disturbances. Input shaping and feedforward control were used to compensate for the World View slewing disturbance. Closed loop rate feedback from the rate gyro to the reaction wheel was used to compensate for both the World View and thermal snap disturbance sources. Closed loop rate feedback from the World View support tip to a piezoceramic actuator at the root was used to attenuate high frequency vibration support vibration.

6.2 Conclusions and Recommendations

Although the stepper motor and thermal snap disturbances are significant, simulations predict that their effects will not exceed reporting accuracy and jitter performance specifications but will exceed the stability specification some of the time. The conclusion is that there may be poor image quality from the World View instrument due to high frequency vibration induced by the World View instrument and thermal snap.

The application of input shaping to the World View stepper motor slew command was successful in preventing excitation of the low frequency solar array modes. This demonstrates the usefulness of input shaping as an open loop compensation method. The use of feedforward control to counteract the stepper motor's applied torque also prevented low frequency solar array vibration, demonstrating the usefulness of feedforward compensation. Both of these open loop methods further improve the World View line-of-sight pointing accuracy, although improvement is not required. Rate feedback from the rate gyro to the reaction wheel slightly reduced the level of low frequency solar array vibration observable on the spacecraft bus. However, this method only isolates the disturbances and does not eliminate it, and furthermore, is only marginally stable. These qualities make the method undesirable. Rate feedback from the World View support tip to the piezoceramic actuator at the root of the support successfully eliminated high frequency support vibration. This method was successful in improving the World View line-of-sight stability when the system was excited by a mirror slew, although the specification is still exceeded for a short time.

Confidence in the results presented is limited due to a number of unresolved issues. There are a number recommendations that can be made regarding these. First, the finite element model of the structure needs verification and updating. This should help to correct any mis-modeling of the spacecraft. The damping value of 0.5% assumed for all the modes is the most significant parameter likely to change with model updating. The damping values associated with World View support modes will most likely decrease, allowing vibrations to continue for a longer period of time.

In addition, the current finite element model may not have high enough resolution to model the very high frequency modes, such as those which required the double lag compensator in Section 5.2.1, making the success of the closed loop compensation methods questionable. Despite the size of this model, a higher resolution model may prove necessary.

Second, the models of the stepper motor and thermal snap also need verification. Verification of the stepper motor model should be relatively easy, since it can be tested directly on the spacecraft prior to launch. The thermal snap model can be verified by comparing its effects on a model of an orbiting spacecraft to the spacecraft's actual on-orbit thermal snap response. Changes in the disturbance models combined with a verified and updated structural model could result in significant changes in the responses.

Third, no sensor or actuator dynamics have been included in the simulation models. Sensor rolloff at high frequency may cause significant phase lags which are important to consider for stability in closed loop systems. Similarly, actuator rolloff may cause the same problem, and may also reduce the amount of authority available at higher frequencies. These effects, though, can be easily measured and accounted for in a final model.

Appendix A

Spacecraft Response to World View Slews

This appendix shows the spacecraft performance, measured as inertial angles at tip of the World View support, in response to the World View slew maneuvers listed in Table 3.1. Shown are responses to both the smooth and discrete World View inputs. Also shown are a comparison of the responses to the World View accuracy, stability and jitter specifications.

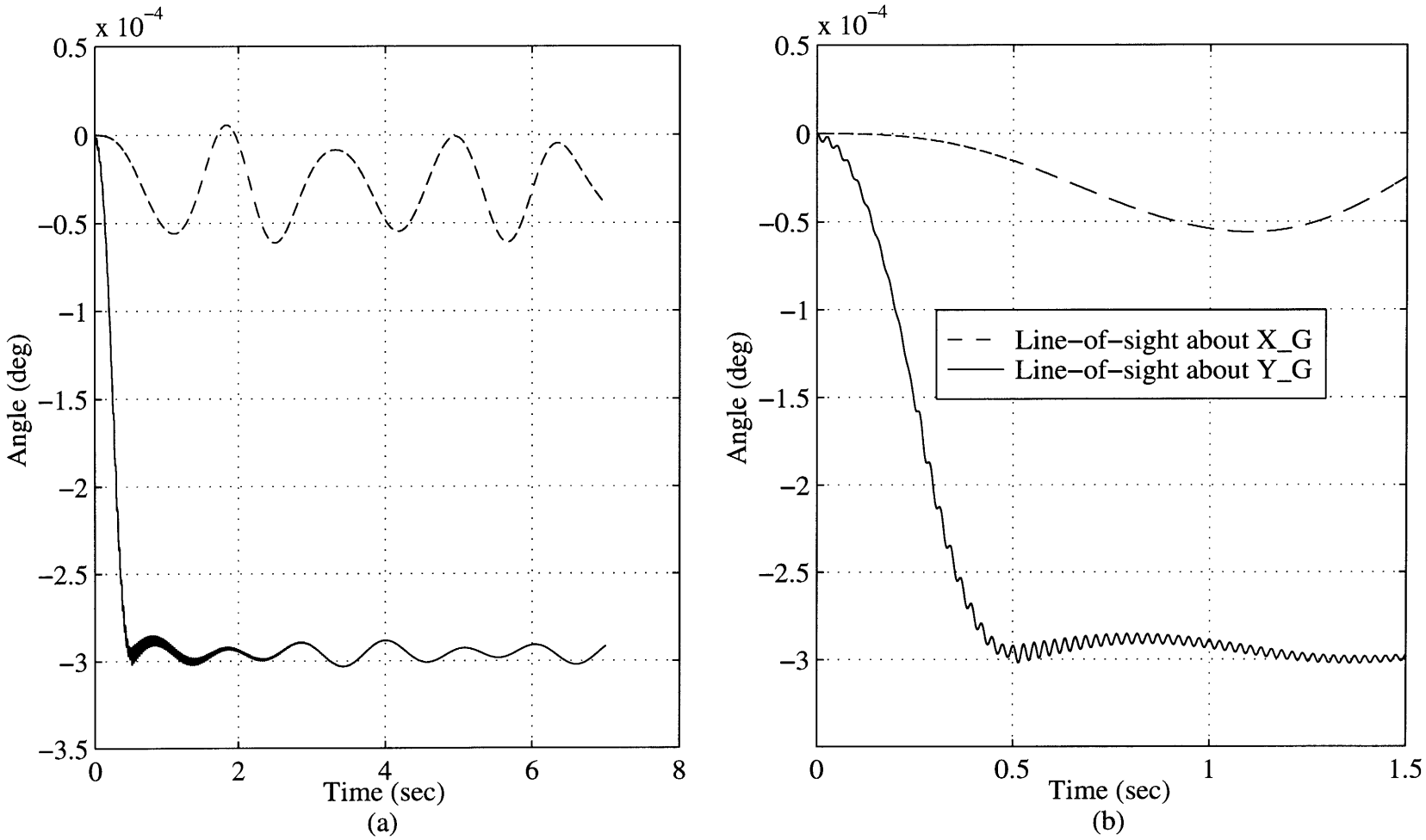

Figure A-1: World View line-of-sight error due to the *smooth* 0.35 deg Z_{M} mirror slew in 0.5 seconds. (a) Long term response showing low frequency vibration. (b) Transient response showing high frequency vibration.

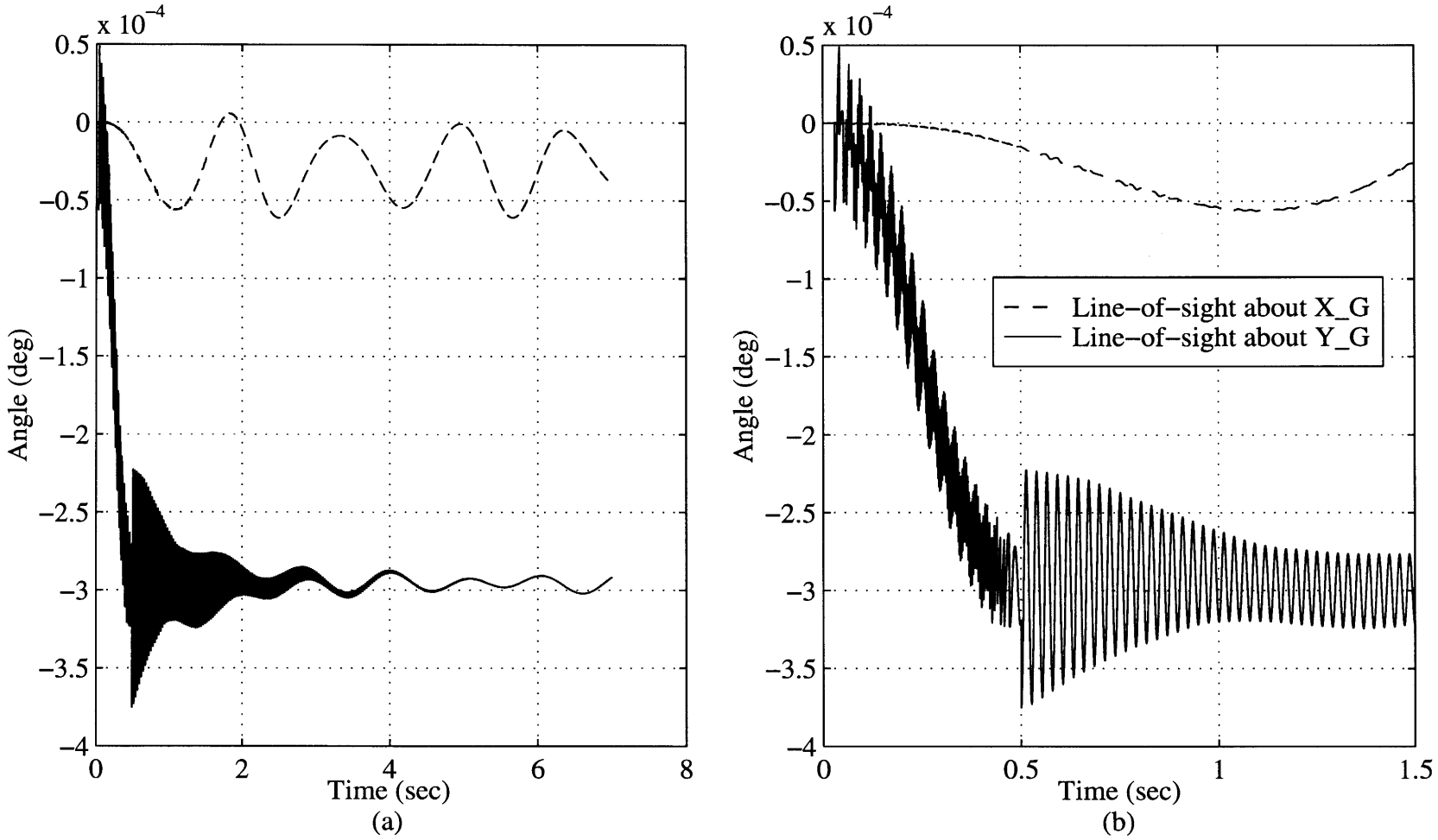

Figure A-2: World View line-of-sight error due to the *discrete* 0.35 deg Z_M mirror slew in 0.5 seconds. (a) Long term response showing low frequency vibration. (b) Transient response showing high frequency vibration.

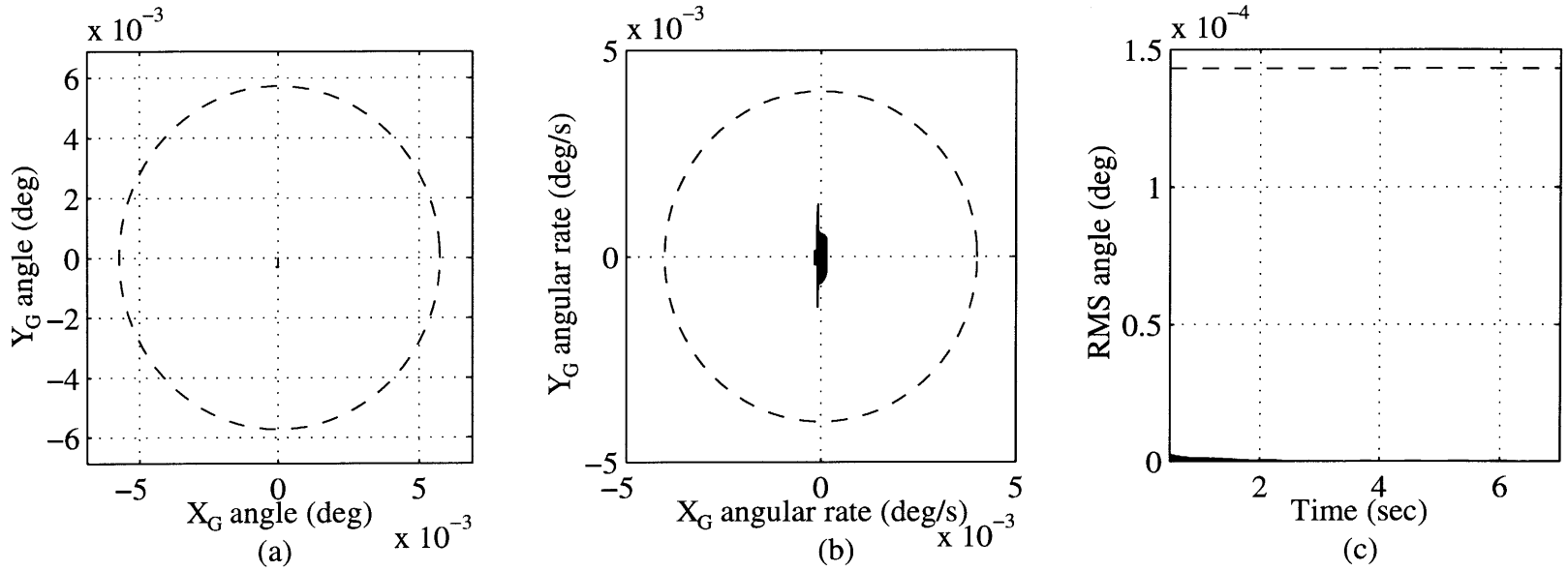

Figure A-3: Comparison of performance response to the *smooth* 0.35 deg Z_{M} mirror slew with World View specifications. (a) Line-of-sight accuracy. (b) Line-of-sight stability. (c) Line-of-sight jitter.

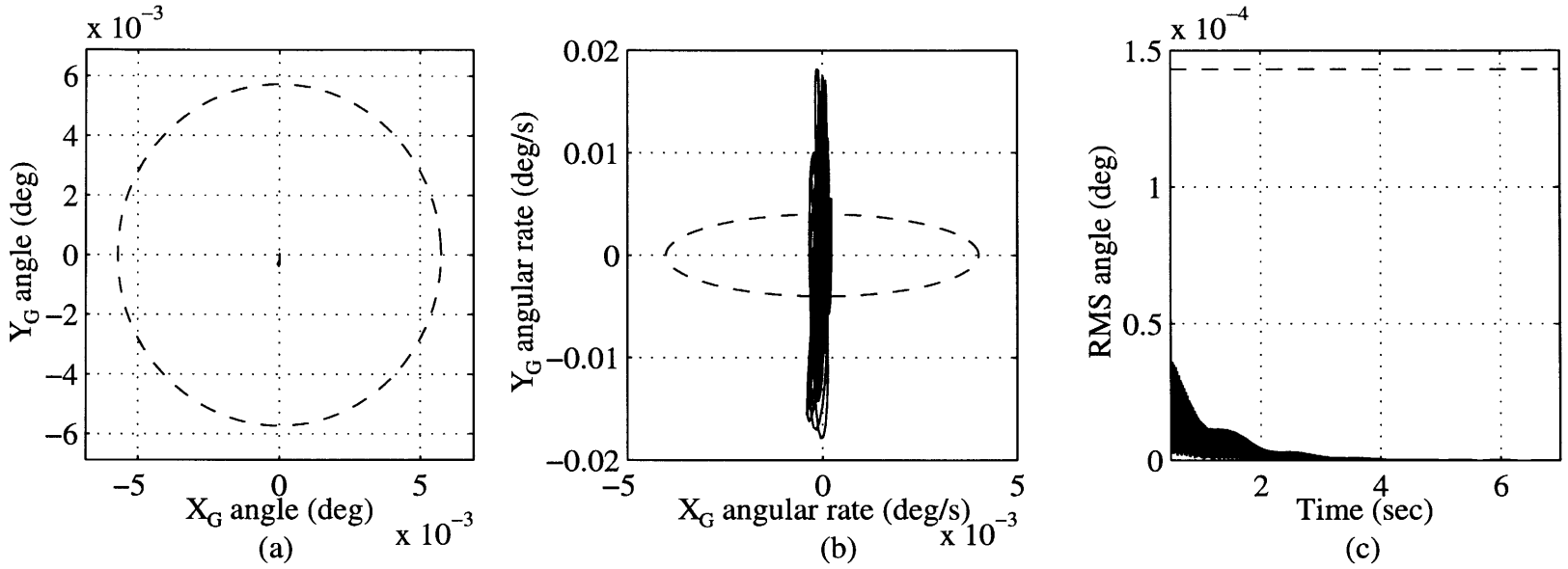

Figure A-4: Comparison of performance response to the *discrete* 0.35 deg Z_M mirror slew with World View specifications. (a) Line-of-sight accuracy. (b) Line-of-sight stability. (c) Line-of-sight jitter.

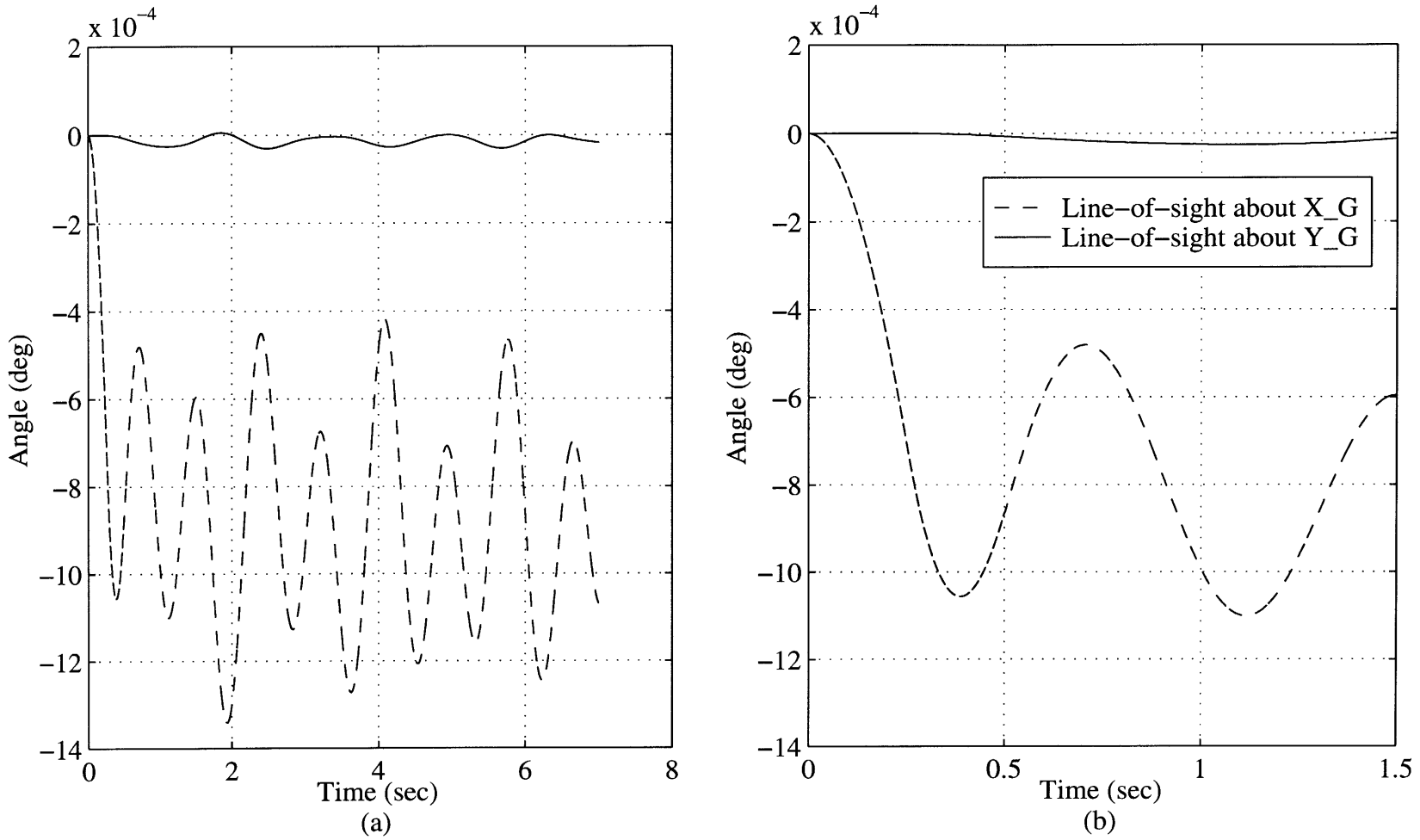

Figure A-5: World View line-of-sight error due to the *smooth* 0.7 deg X_{M} mirror slew in 0.5 seconds. (a) Long term response showing low frequency vibration. (b) Transient response showing high frequency vibration.

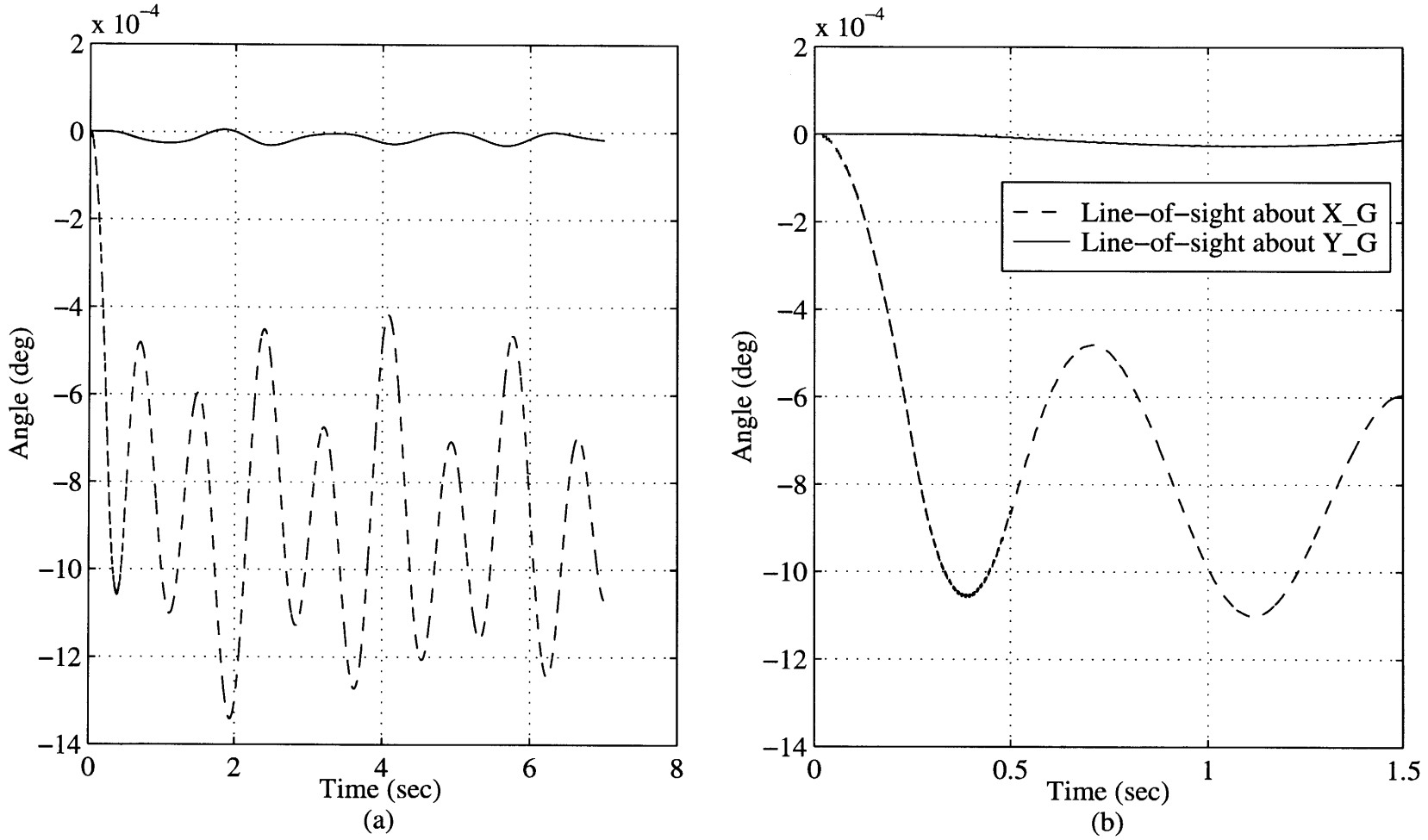

Figure A-6: World View line-of-sight error due to the *discrete* 0.7 deg X_{M} mirror slew in 0.5 seconds. (a) Long term response showing low frequency vibration. (b) Transient response showing high frequency vibration. (a) Line-of-sight error about X_{G}. (b) Line-of-sight error about Y_{G}.

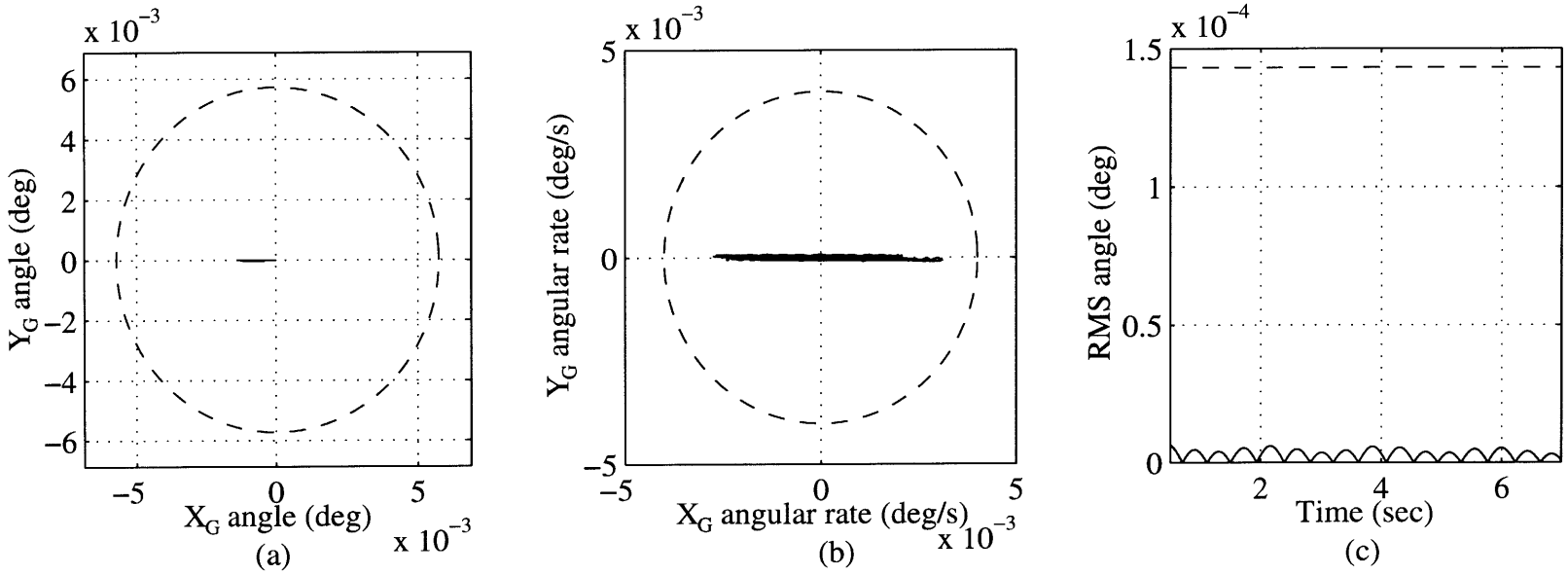

Figure A-7: Comparison of performance response to the *smooth* 0.7 deg X_{M} mirror slew with World View specifications. (a) Line-of-sight accuracy. (b) Line-of-sight stability. (c) Line-of-sight jitter.

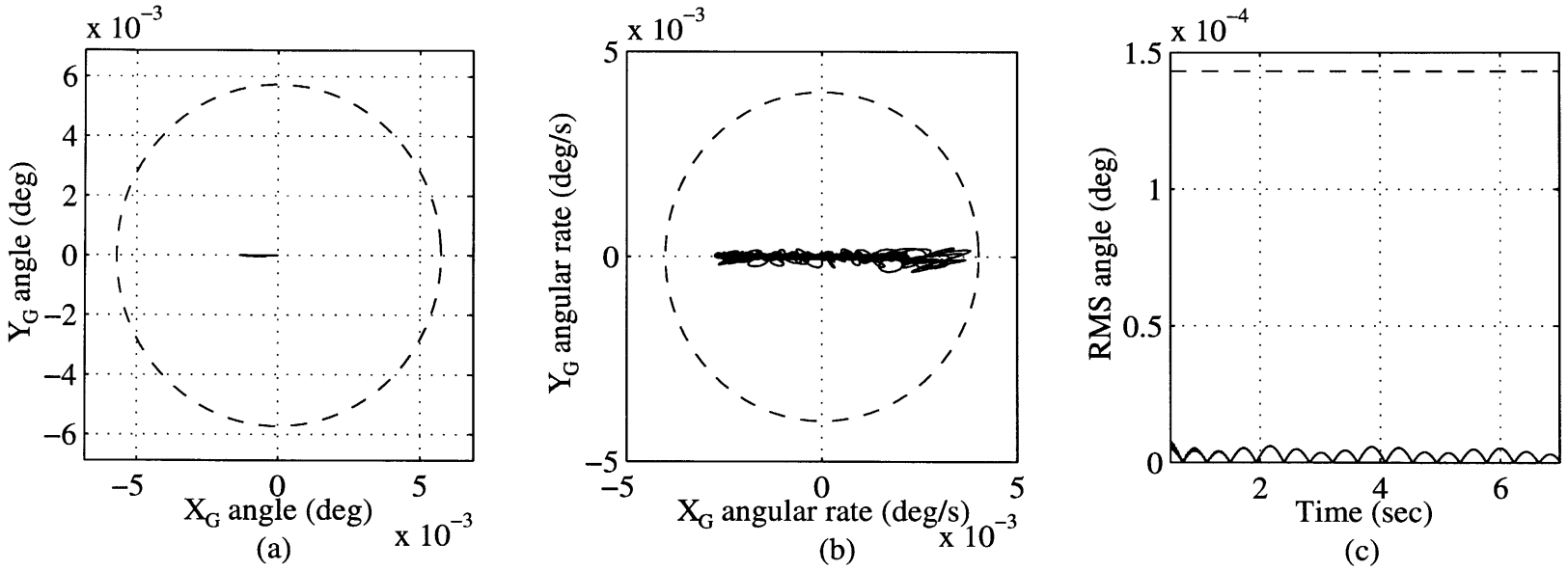

Figure A-8: Comparison of performance response to the *discrete* 0.7 deg X_{M} mirror slew with World View specifications. (a) Line-of-sight accuracy. (b) Line-of-sight stability. (c) Line-of-sight jitter.

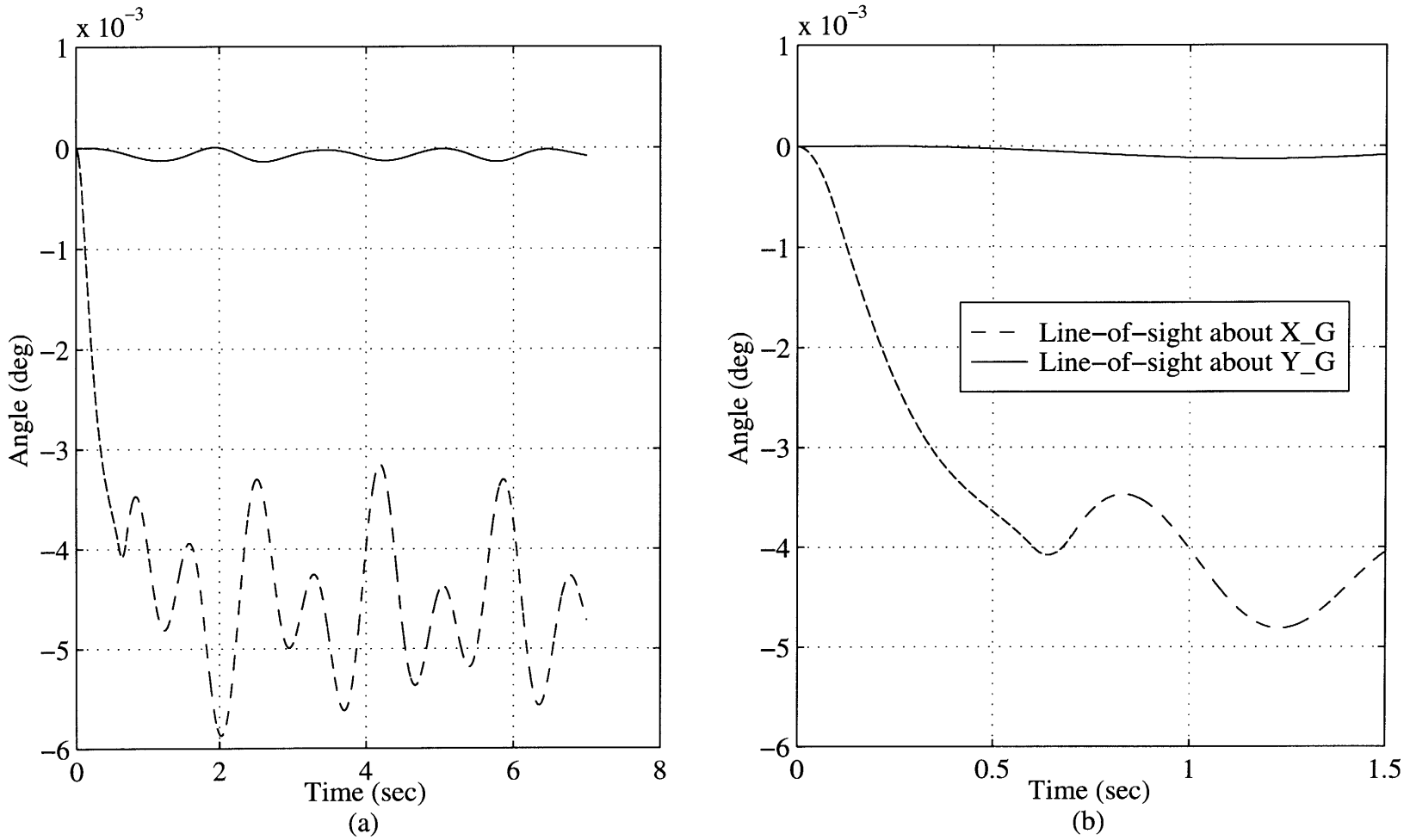

Figure A-9: World View line-of-sight error due to the *smooth* 3.6 deg X_{M} mirror slew in 0.7 seconds. (a) Long term response showing low frequency vibration. (b) Transient response showing high frequency vibration.

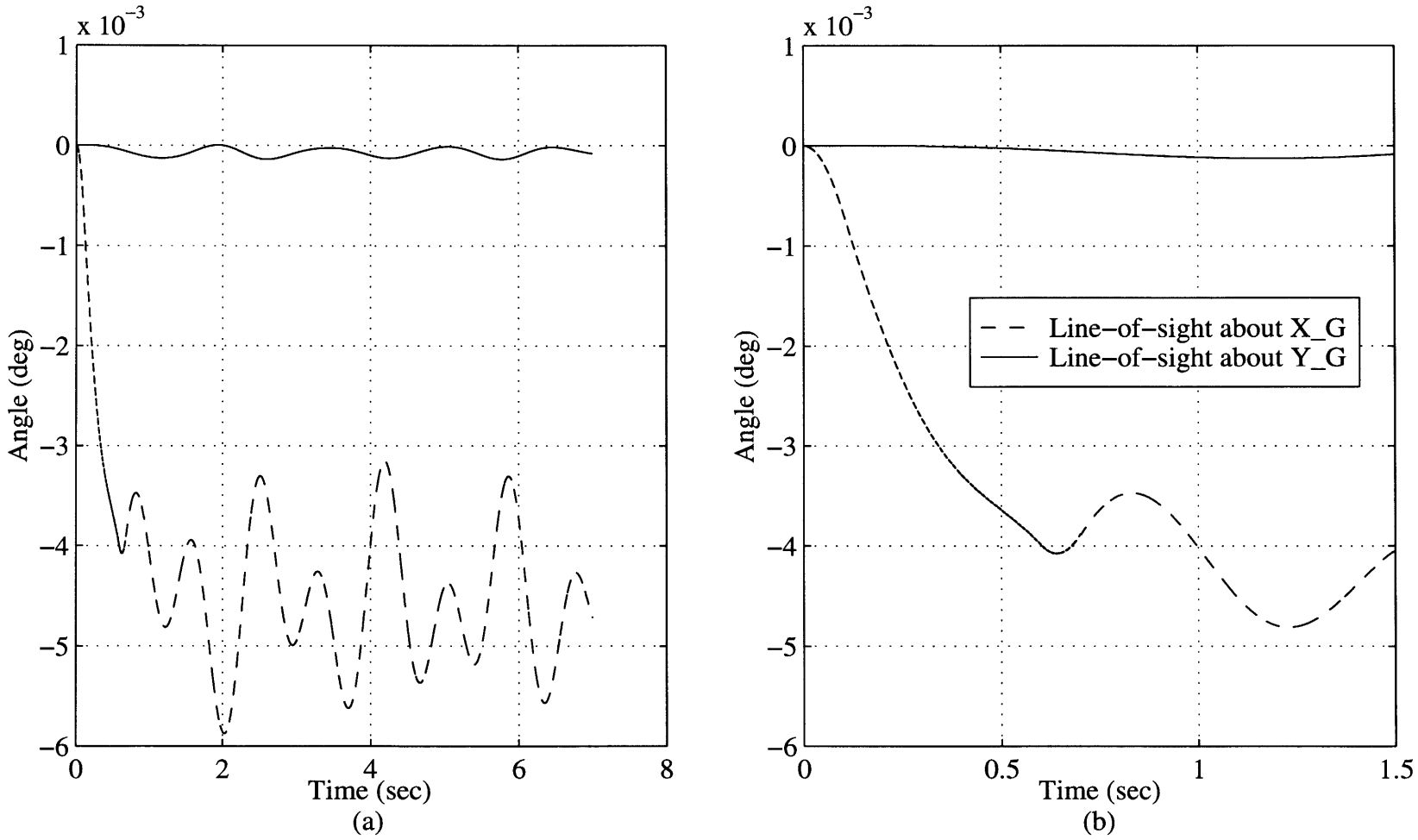

Figure A-10: World View line-of-sight error due to the *discrete* 3.6 deg X_M mirror slew in 0.7 seconds. (a) Long term response showing low frequency vibration. (b) Transient response showing high frequency vibration.

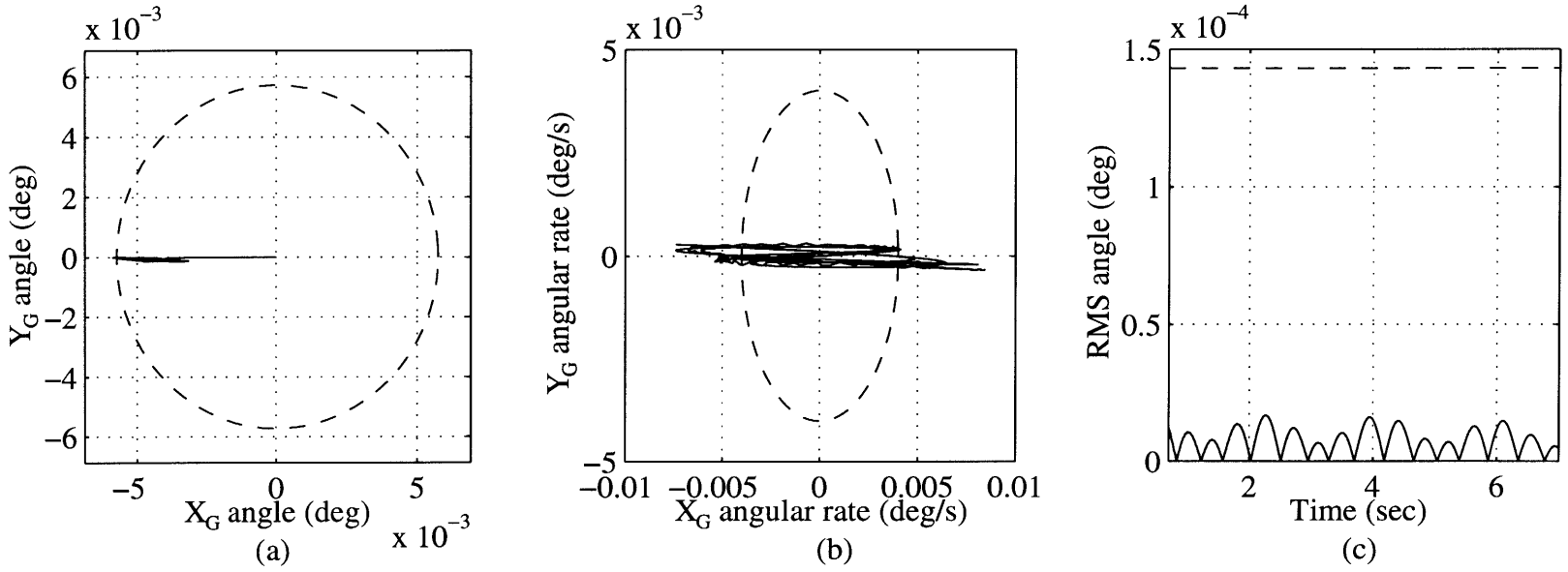

Figure A-11: Comparison of performance response to the *smooth* 3.6 deg X_{M} mirror slew with World View specifications. (a) Line-of-sight accuracy. (b) Line-of-sight stability. (c) Line-of-sight jitter.

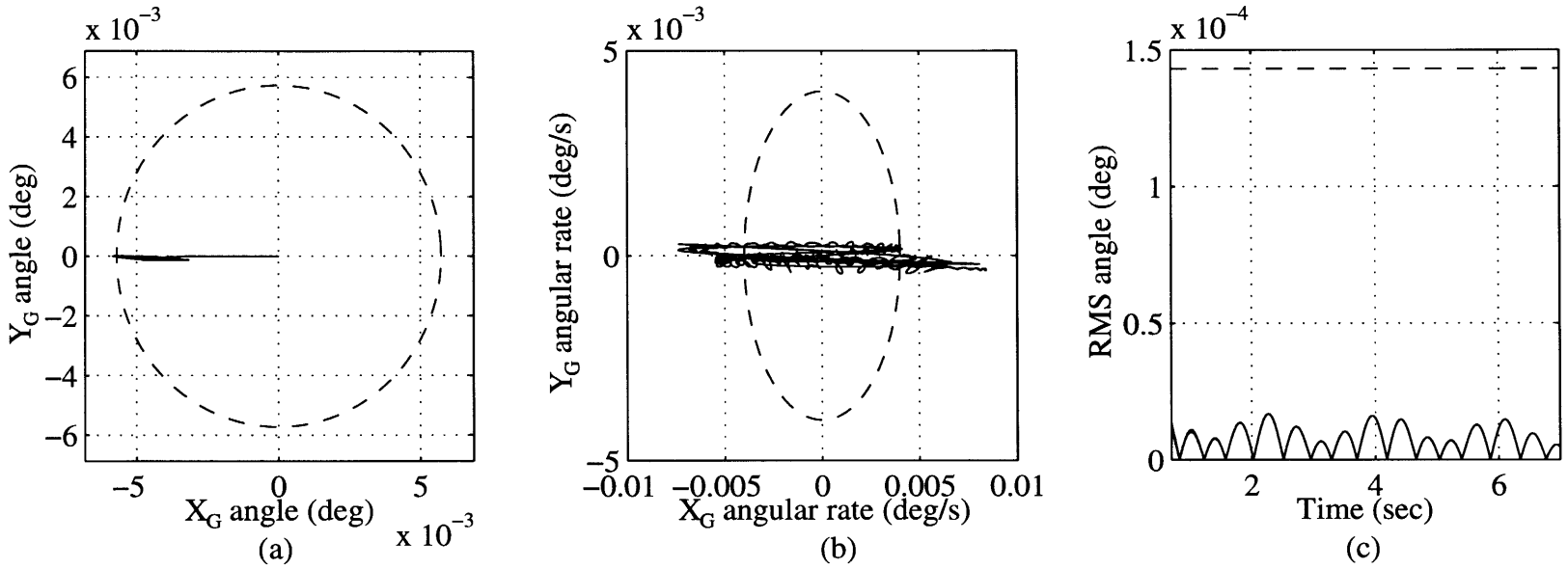

Figure A-12: Comparison of performance response to the *discrete* 3.6 deg X_{M} mirror slew with World View specifications. (a) Line-of-sight accuracy. (b) Line-of-sight stability. (c) Line-of-sight jitter.

References

[1] Acarnley, P. P., *Stepping Motors: A Guide to Modern Theory and Practice*, Second Edition, Peter Peregrinus Ltd., London, UK, 1984.

[2] Anderson, Eric A. and Crawley, Edward F., "Piezoceramic Actuation of One- and Two-Dimensional Structures," Master's thesis, Massachusetts Institute of Technology, March 1993.

[3] Anderson, Eric H., Blackwood, Gary H., and How, Jonathan P., "Passive Damping in the MIT SERC Controlled Structures Testbed," *presented at the International Symposium on Active Materials and Adaptive Structures*, Nov 1991.

[4] Bailey, T. and Hubbard Jr., J. E., "Distributed Piezoelectric-Polymer Active Vibration Control of a Cantilever Beam," *AIAA Journal of Guidance, Control, and Dynamics*, vol. 8, no. 5, pp. 605–611, Sept–Oct 1985.

[5] Blevins, R. D., *Formulas for Natural Frequency and Mode Shape*, Robert E. Kreiger Publishing Company, Malabar, FL, 1979.

[6] Crandall, Stephen H., Dahl, Norman C., and Lardner, Thomas J., *An Introduction to the Mechanics of Solids*, Second Edition, McGraw-Hill Book Company, 1978.

[7] Crawley, Edward F. and Anderson, Eric A., "Detailed Models of Piezoceramic Actuation of Beams," *Journal of Intelligent Material Systems and Structures*, vol. 1, no. 1, pp. 4–25, 1990.

[8] Crawley, Edward F. and Hall, Steven R., "The Dynamics of Controlled Structures," *1991 Notes, SERC#10-91-I*, July 1991.

[9] Glaese, Roger M. and Miller, W. David, "Development of Zero-Gravity Structural Control Models from Analysis and Ground Experimentation," Master's thesis, Massachusetts Institute of Technology, January 1994.

[10] Gregory, C. Z. Jr., "Reduction of Large Flexible Spacecraft Models Using Internal Balancing Theory," *AIAA Journal of Guidance, Control, and Dynamics*, vol. 7, no. 6, pp. 725–732, Nov–Dec 1984.

[11] Hagood, Nesbitt W. and von Flotow, Andreas, "Damping of Structural Vibration with Piezoelectric Materials and Passive Electrical Networks," *Journal of Sound and Vibration*, 1991.

[12] Hyde, James M. and Seering, Warren P., "Using Input Command Pre-Shaping to Suppress Multiple Mode Vibration," *Proceedings of IEEE International Conference on Robotics and Automation*, pp. 2604–2609, April 1991.

[13] Kaplow, C. E. and Velman, J. R., "Active Local Vibration Isolation Applied to a Flexible Space Telescope," *AIAA Journal of Guidance and Control*, vol. 3, no. 3, pp. 227–233, May–June 1980.

[14] Lambertson, M., Rohrbaugh, D., and Garrick, J., "Solar Array Thermal Snap and the Characteristics of its Effect on UARS," *NASA, Goddard Space Flight Center, Flight Mechanics/Estimation Theory Symposium*, pp. 575–588, 1992.

[15] Lambertson, M., Underwood, S., Woodruff, C., and Garber, A., "Upper Atmosphere Research Satellite Attitude Disturbances During Shadow Entry and Exit," *Advances in the Astronautical Sciences*, vol. 84, no. 2, pp. 1003–1017, 1993.

[16] Larson, W. J. and Wertz, James R., editors, *Space Mission Analysis and Design*, Microcosm, Inc., Torrence, CA, 1992.

[17] Megson, T. H. G., *Aircraft Structures*, Second Edition, Halsted Press, New York, NY, 1990.

[18] Meirovitch, Leonard, *Elements of Vibration Analysis*, Second Edition, McGraw-Hill, Inc. New York, NY, 1986.

[19] Mercadal, M., "Analysis of the First Middeck Active Control Experiment (MACE) Sample Problem," *Technical Report SERC # 7-91-R, Space Engineering Research Center Massachusetts Institute of Technology*, June 1991.

[20] Molnar, John and Garneck, Mike, "Upper Atmostphere Research Satellite (UARS) In-Flight Jitter Study for EOS Final Report," *General Electric Astro Space, Princeton, NJ*, January 1993.

[21] Morgan Matroc, Inc., Electro Ceramics Division, 232 Forbes Road, Bedford, OH 44146, *Guide to Modern Piezoelectric Ceramics*, March 1993.

[22] Noor, K. Ahmed and Venneri, Samuel L., editors, *Flight-Vehicle Materials, Structures, and Dynamics*, volume 5, American Society of Mechanical Engineers, 1993.

[23] Nurre, Gerald S., Nelson, John D., and Bradley, Arthur J., "Current NASA HST Controller Design and Performance," *Advances in the Astronautical Sciences*, vol. 81, pp. 467–492, 1993.

[24] Oda, Mitsushige, "On the Dynamics and Control of the TES-7 Satellite and its Robot Arm," *IEEE International Conference on Intelligent Robots and Systems*, vol. 3, pp. 1586–1593, 1994.

[25] Ogata, Katsuhiko, *Modern Control Engineering*, Second Edition, Prentiss-Hall, Englewood Cliffs, NJ, 1990.

[26] Poelaert, D. and Burke, W.R., "Hubble Space Telescope Solar Array: A Thermally Induced Disturbance Torque," *Proc. American Control Conference*, March 1987.

[27] Singer, N. C. and Seering, W. P., "Preshaping Command Inputs to Reduce System Vibration," *Journal of Dynamic Systems, Measurement, and Control*, vol. 112, pp. 76–82, March 1990.

[28] Skelton, R. E., Hughes, P. C., and Hablani, H. B., "Order Reduction for Models of Space Structures Using Modal Cost Analysis," *AIAA Journal of Guidance, Control and Dynamics*, vol. 5, no. 4, pp. 351–357, 1982.

[29] Spanos, John T., "Control-Structure Interaction in Precision Pointing Servo Loops," *AIAA Journal of Guidance, Control and Dynamics*, vol. 12, no. 2, pp. 256–263, March–April 1989.

[30] Sutliff, Daniel L. and Nagel, Robert T., "Active Control of Far-field Noise from a Ducted Propeller," *AIAA Journal*, vol. 33, no. 2, pp. 231–236, February 1995.

[31] Tal, Jacob, "Step vs Servo Motors - A New Look," *Proceedings of the 16th Annual Symposium on Incremental Motion Control Systems and Devices*, pp. 119–125, 1987.

[32] Tuttle, Timothy D. and Seering, Warren P., "A Zero-placement Technique for Designing Shaped Inputs to Suppress Multiple-mode Vibration," *Proceedings of the American Control Conference*, 1994.

[33] Tuttle, Timothy D. and Seering, Warren P., "Vibration Reduction in 0-g Using Input Shaping on the MIT Middeck Active Control Experiment," *To be published in the Proceedings of the American Control Conference*, 1995.

[34] Zhao, Yongdong and Jayasuriya, Suhada, "Feedforward Controllers and Tracking Accuracy in the Presence of Plant Uncertainties," *Proceedings of the American Control Conference*, vol. 1, pp. 360–364, 1994.

[35] Zimbelman, Darrel F., Dennehy, C. J., Welch, R. V., and Born, G. H., "A Technique for Optimal Temperature Estimation for Modeling Sunrise/Sunset Thermal Snap Disturbance Torque," *NASA, Goddard Space Flight Center, Flight Mechanics/Estimation Theory Symposium*, pp. 431–446, 1990.

[36] Zimbelman, Darrel F. and Zimbelman, Harold F., "Self-Induced Thermal Elastic Shock Disturbance for a Dual-Array Spinning Spacecraft," *Advances in the Astronautical Sciences*, vol. 75, no. 1, pp. 641–656, February 1991.

[37] Zimbelman, Darrell F., "Thermal Elastic Shock and its Effect on Spacecraft Attitude Control," PhD thesis, University of Colorado, 1990.